NUCLEIC ACID-BASED COLORIMETRIC BIOSENSORS FOR ENVIRONMENTAL MONITORING AND LIQUID BIOPSY

Erica Cavaliere

Dottorato in Biotecnologie –PNNR XXXVIII ciclo

Università di Napoli Federico II


Finanziato
dall'Unione europea
NextGenerationEU
Italiadomani
PIANO NAZIONALE
DI RIPRESA E RESILIENZA
agritech

Università di Napoli Federico II

NUCLEIC ACID-BASED COLORIMETRIC BIOSENSORS FOR ENVIRONMENTAL MONITORING AND LIQUID BIOPSY

Erica Cavaliere

Dottorando: Erica Cavaliere

Relatori: Prof. Raffaele Velotta

Prof. Rosanna Capparelli

Coordinatore: Prof. Marco Moracci

Settore Scientifico Disciplinare: FIS/07

This study was carried out within the Agritech National Research Center and received funding from the European Union Next-GenerationEU (PIANO NAZIONALE DI RIPRESA E RESILIENZA (PNRR) – MISSIONE 4 COMPONENTE 2, INVESTIMENTO 1.4 – D.D. 1032 17/06/2022, CN00000022). This manuscript reflects only the authors' views and opinions, neither the European Union nor the European Commission can be considered responsible for them.

Index

Riassunto 1

Summary 4

Introduction 6

Chapter 1 — Optical biosensors based on localized surface plasmon resonance (LSPR) 11

1.1 Introduction to biosensors: definition, components, and operating principles 11

1.2 Key performance metrics and characteristics of biosensors 11

1.3 Optical biosensors: principles, advantages, and major techniques 12

1.4 Localized surface plasmon resonance (LSPR): physical principles and tuning parameters 13

1.4.1 LSPR dependence on nanoparticle size: Quasi-static approximation and size effect 15

1.4.2 LSPR dependence on refractive index of the medium: role of the Drude Model 17

1.4.3 Plasmon coupling and LSPR dependence on interparticle distance 18

1.5 Colorimetric biosensors based on LSPR: principles and detection strategies 20

1.6 AuNPs: the ideal platform for LSPR-based colorimetric biosensing 20

Chapter 2 — Gold nanoparticles (AuNPs) as a versatile platform for nucleic acid-based colorimetric biosensing 22

2.1 Gold nanoparticles as platform 22

2.2.1 Synthesis of AuNPs 23

2.2.2 AuNPs Characterization 23

2.3 Surface biofunctionalization 24

2.3.1 Methods to obtain Au-S bound 26

2.4 Biorecognition elements: aptamers and ssDNA probes 28

2.4.1 RNA aptamers for exosome detection 29

2.4.2 ssDNA probes for environmental DNA (eDNA) detection 30

2.5 Nucleic acid functionalization for the two biosensing platforms 31

2.6 Functionalization with RNA aptamer for BC derived exosome detection 31

2.6.1 SH-RNA aptamer activation, AuNPs functionalization, and surface coverage characterization 31

2.7 Functionalization with ssDNA for eDNA detection 33

2.7.1 Probe's thiol group activation and functionalization 33

2.7.2 Conjugation protocol and sequence-dependent optimization of ssDNA:AuNP ratios 34

2.7.3 Post-functionalization purification and colloidal stability validation 34

2.7.4 Quantification of ssDNA surface coverage and interstrand spacing 38

2.8 Transition to experimental work 39

Chapter 3 — A colorimetric aptasensor for exosome detection in breast cancer liquid biopsy 41

3.1 The clinical need for non-invasive and early-stage breast cancer detection 41

3.2 Anti-aggregation-based detection 42

3.3 Interaction between GREM1 and aptamer functionalized AuNPs 44

3.4 Interaction between GREM1 and purified exosomes 46

3.5 Assay performance in real samples 48

3.5.1 Signal processing in complex matrices 48

3.5.2 Diagnostic discrimination between tumoral and non-tumoral samples 48

3.5.3 Morphological Validation by Transmission Electron Microscopy 48

3.6 Assay specificity 50

3.6.1 Specificity against non-target cancers 50

3.6.2 Benchmarking against conventional detection methods 51

3.6 Discussion and key findings 52

Chapter 4 — Development of a Colorimetric ssDNA Biosensor for the Detection of *Fusarium oxysporum* Environmental DNA 54

4.1 The agricultural need for field-deployable detection of *Fusarium oxysporum* in soil 54

4.2 Complementary-Probe anti aggregation assay 55

4.3. Dose–response curve and Limit of Detection (LOD) Determination 58

4.3.1 Dose-response curve in ultra-pure water 58

4.4 Specificity assessment 61

4.4.1 Specificity against non-target sequence in complex mixture 61

4.4.2 Supporting evidence from preliminary studies 62

4.5 Real sample test 66

4.5.1 Sample preparation and DNA extraction 66

4.5.2 DNA Fragment size control and quality verification 66

4.5.4 Recovery in real matrices 68

4.6 Final considerations 72

5. — Conclusions 73

References 75

Appendix 95

Finanziato dall'Unione europea NextGenerationEU
Italiadomani PIANO NAZIONALE DI RIPRESA E RESILIENZA
agritech

Riassunto

La diagnosi precoce del cancro e il monitoraggio ambientale dei patogeni agricoli rappresentano due sfide critiche del nostro tempo, con impatti profondi sulla salute umana e sulla sicurezza alimentare globale. Nel contesto oncologico, il cancro al seno rimane la neoplasia più diffusa tra le donne, e la sua prognosi dipende fortemente dalla capacità di rilevarlo in fase iniziale, idealmente attraverso metodi non invasivi. Parallelamente, in ambito agricolo, funghi fitopatogeni come *Fusarium oxysporum* causano perdite economiche devastanti in colture di alto valore, spesso senza sintomi visibili fino a danni irreversibili. In entrambi i casi, i metodi diagnostici tradizionali risultano lenti, costosi e richiedono infrastrutture specializzate, limitandone l'uso in contesti point-of-care o sul campo.

Per superare queste limitazioni, in questa tesi di dottorato sono stati sviluppati due biosensori colorimetrici innovativi, basati su nanoparticelle d'oro (AuNPs) e acidi nucleici (NAs) come elementi di riconoscimento, capaci di fornire un segnale visivo diretto senza strumentazione complessa. Entrambi i sistemi sfruttano la risonanza plasmonica localizzata (LSPR), ma adottano differenti NAs e strategie di rilevamento, dimostrando la versatilità della piattaforma.

Il primo biosensore è stato progettato per la rilevazione di esosomi derivati da cellule di carcinoma mammario in fluidi biologici. Prevede l'utilizzo di un aptamero RNA (Ex.50.T), specifico per la proteina GREM1 espressa sulla superficie degli esosomi tumorali. Lo schema di rilevazione sfrutta AuNPs funzionalizzate con l'aptamero in cui viene indotta l'aggregazione mediante aggiunta controllata di sale, risultando in una soluzione di colore blu. In presenza di esosomi target, il legame specifico aptamero–esosoma induce la disaggregazione dei cluster di nanoparticelle, producendo un viraggio visibile dal blu al rosso. Questo approccio, basato su un meccanismo di disaggregazione indotta dal target, consente la rilevazione diretta in sieri diluiti, senza amplificazione, aprendo la strada a test rapidi per la biopsia liquida.

Il secondo biosensore è stato sviluppato per la rilevazione del DNA ambientale (e-DNA) e in particolare del DNA genomico di *F. oxysporum* in campioni ambientali. La rilevazione con questo biosensore si basa sull' utilizzo di sonde di DNA a singolo filamento (ssDNA) e su un meccanismo di anti-aggregazione che sfrutta due lotti distinti di AuNPs: uno funzionalizzato con una sonda (Probe) complementare al DNA

bersaglio, l'altro con la sequenza complementare (C_Probe). In assenza del target, le sonde Probe e C_Probe si ibridizzano, causando aggregazione delle AuNPs e un viraggio dal rosso al blu. In presenza del DNA di *F. oxysporum*, il target si lega alla sonda Probe durante un primo step di ibridazione, impedendo l'interazione con C_Probe e mantenendo il colore rosso. Entrambi gli step di ibridazione sono accelerati dal congelamento, consentendo una rilevazione in soli 5 minuti. Questo approccio permette una rilevazione rapida e strumentalmente semplice del target dopo un'opportuna preparazione del campione.

Insieme, questi due biosensori incarnano un paradigma emergente: "una piattaforma, molteplici missioni". La chiave di questa adattabilità risiede nella straordinaria versatilità degli acidi nucleici come elementi di riconoscimento: gli aptameri, selezionati per legare target proteici con alta affinità, e le sonde di ssDNA, progettate per riconoscere sequenze genetiche attraverso l'ibridazione, sono entrambi molecole sintetiche, stabili, facilmente modificabili e completamente programmabili a livello di sequenza. Questa duplice natura, riconoscimento di proteine o di acidi nucleici, consente di estendere la stessa piattaforma plasmonica a contesti biologici profondamente diversi, semplicemente cambiando la sonda immobilizzata sulla superficie delle AuNPs. Pur condividendo la stessa piattaforma plasmonica basata su AuNPs e LSPR essi rispondono a problematiche radicalmente diverse, una in ambito clinico, l'altra in quello ambientale, dimostrando come la programmabilità degli acidi nucleici possa essere sfruttata per progettare strategie ottiche adattive e altamente specifiche.

Questo lavoro di dottorato dimostra come una singola piattaforma plasmonica, opportunamente funzionalizzata con acidi nucleici diversi, possa affrontare sfide diagnostiche in ambiti apparentemente distanti, dalla biopsia liquida per il cancro al seno al monitoraggio di patogeni fitosanitari, offrendo soluzioni rapide, a basso costo e prive di strumentazione complessa. Il biosensore per la rilevazione di esosomi è stato già validato su matrici cliniche reali, dimostrando la sua applicabilità in contesti biomedici, mentre il sistema per *F. oxysporum* rappresenta una base solida per lo sviluppo di strumenti diagnostici sul campo, la cui implementazione beneficerà di ulteriori test sul campo. Prospettive future includono l'integrazione con lettori smartphone per la quantificazione del segnale colorimetrico e l'estensione della piattaforma ad altri target di rilevanza clinica o ambientale,

consolidando il paradigma di una diagnostica versatile, decentralizzata e accessibile.

Summary

Early cancer diagnosis and environmental monitoring of agricultural pathogens represent two critical challenges of our time, with profound implications for human health and global food security. In oncology, breast cancer remains the most prevalent malignancy among women, and its prognosis is heavily dependent on the ability to detect it at an early stage, ideally through non-invasive methods. Concurrently, in agriculture, phytopathogenic fungi such as *Fusarium oxysporum* cause devastating economic losses in high-value crops, often without visible symptoms until irreversible damage has occurred. In both domains, conventional diagnostic methods are slow, expensive, and require specialized infrastructure, which limits their use in point-of-care or field settings.

To overcome these limitations, this doctoral thesis shows the development of two innovative colorimetric biosensors based on gold nanoparticles (AuNPs) and nucleic acids (NAs) as biorecognition elements, capable of delivering a direct visual signal without complex instrumentation. Both systems exploit localized surface plasmon resonance (LSPR) but employ different types of NAs and detection strategies, thereby demonstrating the platform's versatility.

The first biosensor was designed for the detection of breast cancer-derived exosomes in biological fluids. It utilizes an RNA aptamer, Ex.50.T, which specifically targets GREM1, a protein expressed on the surface of tumor-derived exosomes. The detection scheme employs aptamer-functionalized gold nanoparticles that are induced to aggregate through controlled salt addition, yielding a blue-colored solution. Upon binding to target exosomes, the specific aptamer–exosome interaction triggers nanoparticle disaggregation, resulting in a visible color shift from blue to red. This target-induced disaggregation mechanism enables direct detection in diluted serum samples without signal amplification, paving the way for rapid liquid biopsy tests.

The second biosensor was developed for the detection of environmental DNA (eDNA), specifically genomic DNA from *F. oxysporum* in environmental samples. This sensor relies on single-stranded DNA (ssDNA) probes and an anti-aggregation mechanism that uses two distinct batches of gold nanoparticles: one functionalized with a target-complementary probe, referred to as Probe, and the other with its complementary sequence, referred to as C_Probe. In the absence of the target, Probe and C_Probe hybridize, leading to AuNPs

and a red-to-blue color change. When *F. oxysporum* DNA is present, it binds to the Probe during an initial hybridization step, preventing interaction with C_Probe and preserving the red color. Both hybridization steps are accelerated by freezing, enabling detection in just five minutes. This approach allows for rapid and instrument-free target identification following appropriate sample preparation.

Together, these two biosensors embody an emerging paradigm: one platform, multiple missions. The key to this adaptability lies in the remarkable versatility of nucleic acids as biorecognition elements. Aptamers, selected to bind protein targets with high affinity, and ssDNA probes, engineered to recognize specific genetic sequences through hybridization, are both synthetic, stable, easily modifiable, and fully sequence-programmable molecules. This dual capability, targeting either proteins or nucleic acids, enables the same plasmonic platform to address vastly different biological contexts simply by changing the nucleic acid probe immobilized on the AuNPs surface. Although both biosensors share the same gold nanoparticle–localized surface plasmon resonance transduction core, they tackle fundamentally distinct challenges, one clinical and the other environmental, demonstrating how the programmability of nucleic acids can be harnessed to design highly specific and adaptive optical detection strategies.

This doctoral work demonstrates that a single plasmonic platform, when appropriately functionalized with different nucleic acids, can address diagnostic challenges across seemingly disparate fields, from liquid biopsy for breast cancer to phytosanitary pathogen monitoring, offering rapid, low-cost, and instrument-free solutions. The exosome biosensor has already been validated in real clinical matrices, confirming its applicability in biomedical contexts, whereas the *F. oxysporum* system provides a solid foundation for future field-deployable diagnostic tools, with implementation further enhanced by validation in real agricultural soil samples. Future perspectives include integration with smartphone-based readers for colorimetric signal quantification and extension of the platform to additional clinically or environmentally relevant targets, thereby reinforcing the vision of versatile, decentralized, and accessible diagnostics.

Introduction

In recent years, optical biosensors have emerged as powerful tools for molecular detection, bridging the gap between high analytical performance and practical usability. Among them, colorimetric biosensors based on localized surface plasmon resonance (LSPR) of noble metal nanoparticles, particularly gold nanoparticles (AuNPs), have attracted widespread interest due to their simplicity, low cost, and instrument-free readout [1]. The intense absorption in the visible range, coupled with a strong dependence of the LSPR peak on the local dielectric environment, interparticle distance, and nanoparticle morphology, enables the transduction of molecular recognition events into naked-eye color changes [2], typically from red to blue upon aggregation [3]. This makes LSPR-based platforms uniquely suited for point-of-care diagnostics, field-deployable sensing, and other resource-limited settings, applications that span healthcare [4], environmental monitoring [5], pharmaceutical development, biosecurity, and defence [6], without requiring specialized laboratory infrastructure. Compared to traditional analytical methods, optical biosensors significantly reduce the cost, complexity, and turnaround time of testing, making them particularly valuable in low-resource contexts [7].

A key factor determining the success of any biosensor is the biorecognition element [8]. An ideal biorecognition element exhibits selective and high-affinity binding toward the target analyte, thereby conferring specificity to the biosensor [8]. In recent years, nucleic acids (NAs) have been integrated into a wide range of biosensors and bioanalytical assays owing to their diverse physical, chemical, and biological properties. While NAs are traditionally known for their role in storing and transmitting genetic information [9], a feature exploited for the identification of species, genetically modified organisms, pathogens, and toxins, they have also acquired a second, distinct function over the past 25 years: serving as engineered recognition elements in biotechnology and materials science [10].

Accordingly, nucleic acid–based bioreceptors can be broadly classified into two categories: hybridization-based probes and aptamers.

Hybridization-based probes bind complementary nucleic acid targets through Watson–Crick base pairing. Their design relies on the known sequence of nucleic acid biomarkers, such as circulating tumor DNA, microRNAs (miRNAs), or pathogenic genomes, to ensure sequence-specific recognition [11]. The high fidelity of nucleic acid hybridization

forms the core principle of genosensors, enabling the selective detection of target sequences with excellent specificity [12].

Aptamers, often described as “chemical antibodies,” are short, single-stranded synthetic oligonucleotides (DNA or RNA) that bind non-nucleic acid targets, including proteins, peptides, small molecules, and even whole cells or vesicles, with high affinity, selectivity, and specificity through intermolecular forces [11], stems from *in vitro* selection techniques such as “Systematic Evolution of Ligands by EXponential enrichment” (SELEX), which isolates high-affinity ssDNA or ssRNA sequences from random libraries [13]. RNA aptamers frequently exhibit higher binding affinity than their DNA counterparts for the same target [14,15] Upon target binding, aptamers undergo conformational changes in their secondary and tertiary structures; this structural switch serves as the biorecognition event that triggers a detectable signal in aptamer-based biosensors. Additional advantages include excellent batch-to-batch reproducibility, low production cost, stability under harsh conditions, and long-term storage without special requirements [16].

Aptamers can bind selectively to a wide variety of target ligands, ranging from small ions and single molecules to proteins and even whole cells. In recent years, they have attracted significant interest as recognition elements in biosensor design as well as in analytical and diagnostic applications. Thanks to their high specificity, ease of synthesis, and programmability, aptamers are increasingly viewed as promising alternatives to traditional antibodies in bioassay-related fields. As a result, they have been successfully employed in biomolecule detection, cell capture and analysis, imaging applications, and even in various emerging clinical treatments [17].
This versatility arises from the use of different nucleic acids as recognition elements, each relying on a specific molecular interaction mechanism, and represents a shift from “one sensor, one target” to “one platform, multiple missions.” Such an approach is particularly valuable for addressing multidisciplinary challenges spanning clinical diagnostics and environmental monitoring, where the same plasmonic transducer (AuNPs) can be tailored to vastly different biological and analytical contexts.

Cancer is one of the most devastating diseases of the twenty-first century, and its risk of developing is increasing [18]. Breast cancer (BC)

is the second most common cancer diagnosed in women and the leading cause of death from cancer in women worldwide. Early diagnosis of breast cancer greatly increases the chance of cure and survival from the disease. To quickly and accurately screen BC, many diagnostic methods based on imaging and molecular biotechnology have been developed [19]. It has been shown that various imaging techniques such as mammography, magnetic resonance imaging (MRI), positron-emission tomography (PET), Computed tomography (CT), and single-photon emission computed tomography (SPECT) could be used for diagnosis and monitoring patients with breast cancer in various stages [20]. Apart from screening techniques, breast biopsies are generally performed to distinguish between cancerous and benign tissues [21] but this is an expensive method that requires trained people [22]. Biomarker-based methods such as radioimmunoassay, immunohistochemistry, enzyme-linked immunosorbent assay (ELISA) and fluoro-immunoassay also address to the diagnostic requirements for breast cancer. Biomarker-based techniques are sensitive and selective; however, they have some limitations such as being expensive, time consuming, needing trained people and complex labelling process are also required [23].

Unlike conventional soluble biomarkers, such as circulating proteins detected by ELISA or tissue antigens analysed by immunohistochemistry, exosomes are membrane-enclosed vesicles that carry a complex molecular signature reflecting their cell of origin, including surface proteins, nucleic acids, and lipids [24]. In breast cancer, tumor-derived exosomes display disease-specific markers (e.g., HER2, EpCAM, or GREM1) directly on their membrane, offering a more comprehensive and stable source of diagnostic information than isolated soluble factors [25,26]. In this scenario exosomes emerged as potential biomarker for early detection of breast cancer. Exosomes are endosome-derived nanometer-sized (30–150 nm) vesicles that are secreted from various types of cells [27] that are present in many and perhaps all biological fluids [28]. Accumulating evidence has manifested that exosomes enjoy potential value as circulating biomarkers for various types of tumors because of their ubiquitous presence in physiological fluids, extraordinary stability in the circulation, and similarity to original cells contents [29].

Just as tumor-derived exosomes carry molecular fingerprints of cancer, environmental DNA (e-DNA) preserves the genetic signature of its

source organism, enabling species-specific detection without the need for direct observation or culturing.

While the analysis of tumor-derived exosomes addresses a critical challenge in human health, the non-invasive detection of disease-specific signals in complex biological fluids, a conceptually similar need arises in environmental science. Here, the early and reliable identification of pathogenic organisms in soil, water, or air is essential for ecosystem protection, food security, and sustainable agriculture [30]. In this context eDNA, defined as fragments of genomic material released by organisms into their surroundings [31], has emerged as a powerful proxy for species presence, offering a sensitive and non-invasive alternative to direct observation or culturing. However, current eDNA detection methods, such as quantitative PCR (qPCR) or next-generation sequencing, typically require DNA extraction, thermal cycling, and specialized laboratory infrastructure, limiting their applicability in field settings or resource-limited scenarios [32]. This limitation is particularly relevant for phytopathogens like *Fusarium oxysporum*, a soil-borne fungus responsible for devastating vascular wilts [33] in economically important crops, including major food and cash crops such as wheat, barley, maize, bananas, and cotton, often with devastating socio-economic impact [34]. *F. oxysporum* can persist in soil for years as resilient spores, and disease symptoms often appear only after irreversible crop damage has occurred [35]. Conventional detection relies on microbial culturing and morphology identification molecular assays that, despite their specificity, remain confined to centralized laboratories [36]. These constraints underscore the need for rapid, instrument-free, and field-deployable strategies capable of directly interrogating crude environmental samples for pathogen-specific DNA signatures, mirroring the same design principles that motivate point-of-care exosome sensing in oncology.

In response to these parallel diagnostic challenges, this doctoral work focused on the development of two colorimetric biosensing platforms based on AuNPs functionalized with NAs probes: one employing an RNA aptamer for the detection of breast cancer-derived exosomes, and the other utilizing a ssDNA probe for the identification of *Fusarium oxysporum* genomic DNA in environmental samples. Both systems employ localized surface plasmon resonance (LSPR) to generate a visible signal without the need for complex instrumentation, aiming to

bridge the gap between laboratory performance and real-world usability.

Chapter 1 — Optical biosensors based on localized surface plasmon resonance (LSPR)

1.1 Introduction to biosensors: definition, components, and operating principles

The term biosensor was first introduced by Cammann in 1977 [37] and it can be defined as analytical device which converts a biological response into a measurable signal. A biosensor consists of three main elements: a bioreceptor, a transducer, and a signal processing system [38].

The bioreceptor, the sensitive biological element (cell, enzyme, antibody, aptamer, DNA etc) capable of selectively recognizing and reacting with the target analyte. The transducer is a key element in a biosensor. It converts the biorecognition event into a measurable signal that connects with the quantity or in the presence of a chemical or biological target. This process of energy conversion is known as signalling [39]. Transducers generate either optical or electrical signals proportional to the number of analytes–bioreceptor interactions. The signal processing system, which involves amplification and display of the output in an appropriate format [40].

1.2 Key performance metrics and characteristics of biosensors

The performance of a biosensor is experimentally evaluated based on the following parameters:

(i) Selectivity: the ability of a bioreceptor to detect a specific analyte in a sample containing other admixtures and contaminants. Hence selectivity is the most important feature of the biosensor [40].

(ii) Sensitivity: the correlation between variations in the analyte concentration and the corresponding signal intensity produced by the transducer. An optimal biosensor can detect minor fluctuations in the target analyte's concentration, thereby generating a measurable signal [38].

(iii) Stability: a crucial attribute in biosensor applications, particularly when continuous monitoring is essential. It refers to the biosensor's resilience against environmental disturbances, both internal and external. Two primary factors influence this stability: the affinity of the bioreceptor, indicating how effectively the analyte binds to it, and the bioreceptor's degradation over time. High-affinity interactions

ensure consistent analyte detection, while minimizing bioreceptor degradation prolongs the sensor's operational lifespan. Together, these factors determine the reliability and durability of biosensors in long-term monitoring scenarios [41].

(iv) Limit of detection (LOD): defined as the lowest concentration of the target that is able eliciting a measurable signal or response.

(v) Linearity Range: determines the accuracy of the signal obtained, in response to a set of measurements with differing concentrations. This attribute gives insight into the resolution of the biosensor, defined as the minimal change in the target analyte concentration that will elicit a response from the biosensor.

(vi) Reproducibility: the ability of the biosensor to reproduce the same results for duplicated experiments is an immense matter of concern [42]. Along with reproducibility, the results obtained should be of high accuracy and precision and altogether these properties of the biosensor make it the more dependable one.

1.3 Optical biosensors: principles, advantages, and major techniques

Biosensors can be classified according to either the type of signal transducer they employ, such as optical, electrochemical, thermometric (calorimetric), piezoelectric, or magnetic, or the nature of the bioreceptor used for target recognition (Figure 1.1). Among these, optical biosensors offer significant advantages over conventional analytical methods: they enable direct, real-time, and label-free detection of a wide range of biological and chemical analytes by exploiting the interaction between light and a biorecognition element [43]. Within optical biosensing, techniques based on quantifiable optical signals, such as luminescence, fluorescence, or visible color changes, have gained widespread adoption. Surface Plasmon Resonance (SPR) and Localized Surface Plasmon Resonance (LSPR) biosensors have become prominent tools in food safety and quality control, owing to their high sensitivity, rapid response, compatibility with miniaturization into handheld devices, and ability to perform real-time, multiplexed, label-free detection [44].

In this work, we developed two LSPR-based optical biosensors that share the same transduction mechanism but differ in their biorecognition elements: one employs an RNA aptamer, while the other utilizes single-stranded DNA (ssDNA).

1.4 Localized surface plasmon resonance (LSPR): physical principles and tuning parameters

Localized surface plasmon resonance (LSPR) is a nanoscale optical phenomenon exhibited by plasmonic nanomaterials such as gold nanoparticles (AuNPs), which have been extensively studied and continue to attract significant scientific interest due to its versatile applications [45]. When light with a wavelength larger than the nanoparticle diameter interacts with AuNPs, it can drive a resonant collective oscillation of the conduction electrons—induced by the external electric field of the incident radiation—causing the electron cloud to oscillate coherently at the same frequency as the incoming light [46] (Figure 1.2). Although purely electromagnetic in origin, this motion resembles a mechanical vibration of the “electron gas” and is the defining feature of plasmonic behaviour.

The interaction of light with AuNPs results in two optical processes: absorption, where photon energy is dissipated as heat through lattice vibrations (phonons), and scattering, where light is re-emitted elastically in all directions. Together, these contribute to optical extinction, defined as the sum of absorption and scattering [47]. When the frequency of the incident light matches the intrinsic resonant frequency of the nanoparticle’s electron cloud, a strong resonance, known as localized surface plasmon resonance (LSPR), is established.

LSPR is characterized by a distinct peak in the extinction spectrum and a dramatic enhancement of the electric field near the nanoparticle surface. In noble metals such as gold and silver, this resonance typically lies in the visible range. Importantly, the LSPR wavelength is highly sensitive to the nanoparticle’s physical and chemical environment, shifting in response to changes in size, shape, material, inter-particle spacing, and, most significantly, the refractive index of the surrounding medium [48]. This sensitivity forms the basis of LSPR-based sensing: even small changes caused by molecular binding [49] or nanoparticle aggregation [50] produce measurable shifts in the resonance peak, enabling label-free detection of biological and chemical analytes.

LSPR is one of three main types of plasmonic oscillations. Volume plasmons occur in the bulk of a metal and require high-energy excitation (e.g., via electron beams). Surface plasmons propagate along extended metal–dielectric interfaces and are excited with moderate energy (e.g., using prisms or gratings). In contrast, localized surface plasmons are confined to nanoscale particles like AuNPs and can be excited directly by visible light—making them especially practical for optical applications [51].

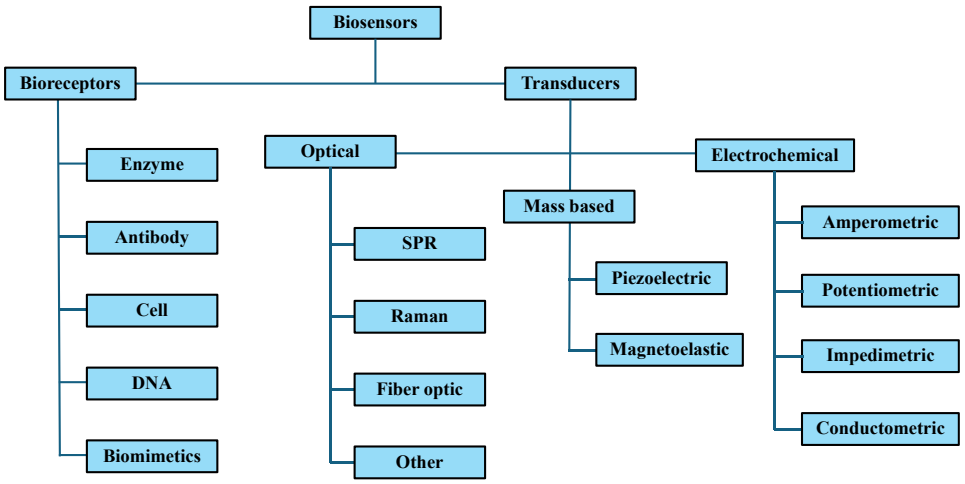

Figure 1.1 Classification of bioreceptors and transducers.

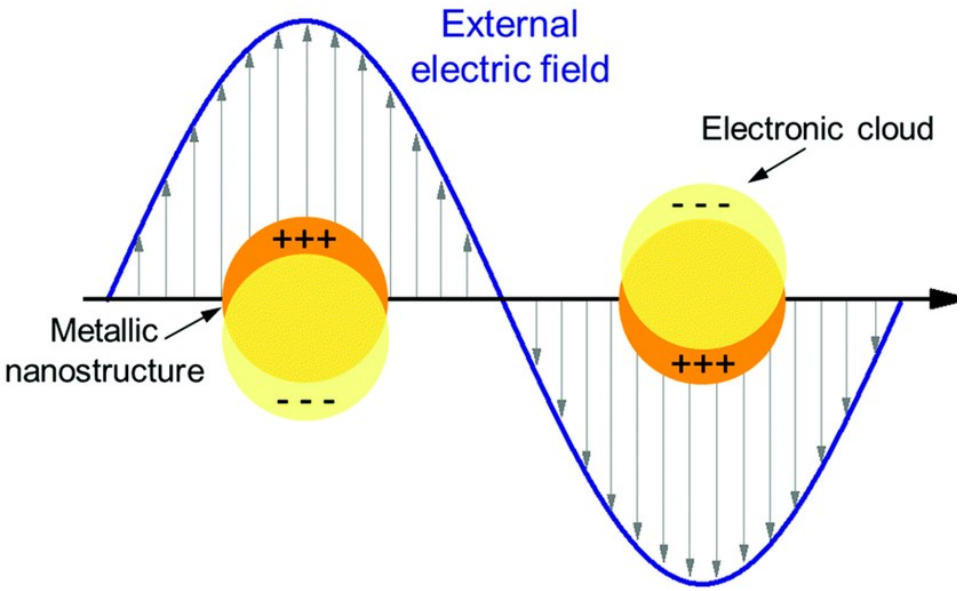

Figure 1.2 Illustrations of localized surface plasmon resonance (LSPR), resulting from the collective oscillations of delocalized electrons in response to an external electric field [52].

1.4.1 LSPR dependence on nanoparticle size: Quasi-static approximation and size effect

The phenomenon of LSPR has been described theoretically by the German physicist Gustav Mie in 1908 [53]. He was the first to rationalize the nature of the plasmon resonance and developed his theory to explain the changes in color exhibited by colloidal solution of AuNPs of different sizes.

If consider the interaction of light with a spherical particle that is much smaller than the wavelength of light, under these circumstances, the electric field of the light can be taken to be constant, and the interaction is governed by electrostatics rather than electrodynamics. This is often called the quasi-static approximation [54].

In quasi-static approximation for particles smaller than 100 nm [51] the contribution from scattering is much smaller than from absorption. Thus, the extinction cross section is approximately equivalent to the absorption cross section, and the total cross section is described by following equation:

where *V* is the volume of the particle, ω is the angular frequency of the incident radiation, c is the speed of light, ε_m is the dielectric constant of the medium, and $\varepsilon'(\omega)$ and $\varepsilon''(\omega)$ are the real and imaginary parts of the dielectric constant of the metal of the nanoparticles. The real part of the dielectric constant of the metal determines the SPR position and the imaginary part determines the bandwidth [55]. The resonance condition occurs when, $\varepsilon'(\omega) = -2\varepsilon_m$, a situation in which σ_{ext} takes the highest possible value [51].

However, for larger nanoparticles, the approximation is no longer valid; the plasmon resonance depends explicitly on the particle size. The larger the particles become, the more important are the higher-order modes as the light can no longer polarize the nanoparticles homogeneously. These higher-order modes peak at lower energies and therefore the plasmon band red shifts with increasing particle size. At the same time, the plasmon bandwidth increases with increasing particle size [56]. (Figure 1.3)

$$\sigma_{\text{ext}} = \frac{9V\,\varepsilon_m^{3/2}}{c} \cdot \frac{\omega\,\varepsilon''(\omega)}{(\varepsilon'(\omega) + 2\varepsilon_m)^2 + \left(\varepsilon''(\omega)\right)^2} \qquad (1)$$

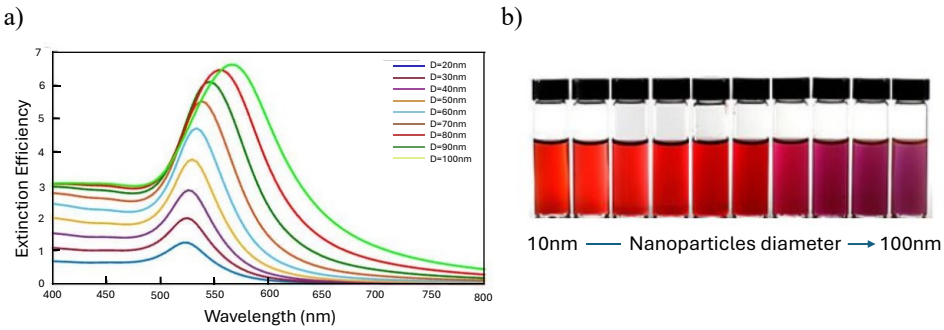

Figure 1.3 a) Extinction efficiency of spherical AuNPs in water [57] b) Colloidal solutions of spheroidal AuNPs with diameters in the range 10-100 nm, at increments of 10 nm.

1.4.2 LSPR dependence on refractive index of the medium: role of the Drude Model

To find out how the refractive index (RI) of the medium affects the LSPR peak wavelength, the Drude model gives an analytical form through that formula:

$$\lambda_{LSPR} = \lambda_p \sqrt{1 + 2n^2} \qquad (2)$$

Where λ_{LSPR} is the wavelenght at which we have resonance, λ_p is the plasma wavelength associated to the metal nanoparticle, and *n* is the RI of the medium surrounding the particle. The key insight from this relationship is that as the RI increases, for example, when biomolecules bind to the nanoparticle's surface, the resonance wavelength λ_{LSPR} becomes longer, shifting toward the red part of the spectrum (red–shifts) [58,59]. This predictable color change forms the physical basis for many label-free biosensors: the presence or concentration of a target molecule can be detected simply by tracking how much the nanoparticle's color shifts. In biosensing, this effect is not only exploited for detection but also for functionalization, as nanoparticle surfaces can be modified with specific receptors (e.g., antibodies or nucleic acids) (Figure 1.4).

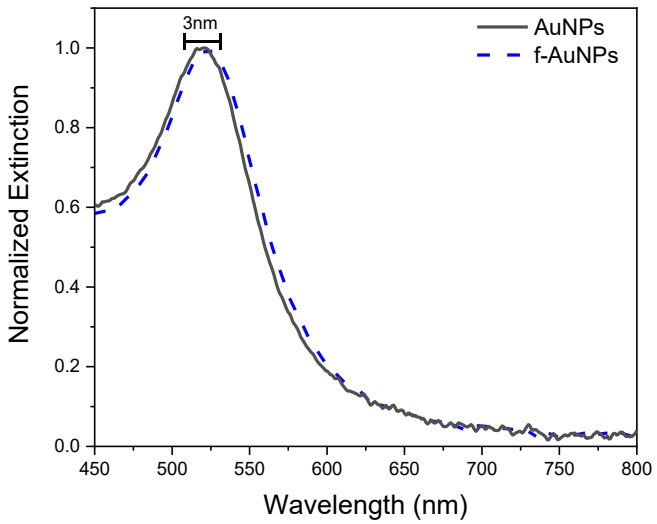

Figure 1.4 UV–Vis spectrum of 20 nm gold nanoparticles before (black) and after (red) oligonucleotide conjugation. A red shift of around 3 nm is observed due to the attachment of antibody on the AuNP surface, which induces a change in the local refractive index (RI).

1.4.3 Plasmon coupling and LSPR dependence on interparticle distance

LSPR frequency shift to longer wavelengths can be achieved not only by synthesizing larger and/or asymmetric structures but also through plasmonic coupling that couples their electromagnetic fields [60]. This phenomenon occurs when two gold nanoparticles are brought into proximity; their localized surface plasmon resonances interact through near-field electromagnetic coupling. This interaction gives rise to hybridized plasmon modes, the most prominent of which is the bonding dipole mode, where electron oscillations align across the gap between particles [61]. This mode resonates at a lower energy than the plasmon of an isolated nanoparticle, resulting in a pronounced red-shift of the absorption peak, often visible to the naked eye as a color change from red to blue [62]. The magnitude of the assembly-induced plasmon shift depends on the strength of the interparticle coupling, which, in turn, depends on the proximity of the individual nanoparticles. The plasmon shift thus gives a measure of the distance between the particles. The

closer the particles in the assembly, the larger is the red-shift of the plasmon resonance (Figure 1.5).

The magnitude of this shift is described by:

$$\Delta\lambda \propto \frac{1}{d^3} \qquad (3)$$

where $\Delta\lambda$ is the peak wavelength shift and d is the edge-to-edge gap between nanoparticles [61,63]. This extreme distance sensitivity means that even sub-10 nm changes, such as those induced by biomolecular binding, produce easily measurable optical responses.

In biosensing, this effect can be used when the analytes interacting with the bioreceptors on the AuNPs either pull them closer together inducing aggregates [64]. Or inducing controlled aggregates to use their disaggregation to detect something [65].

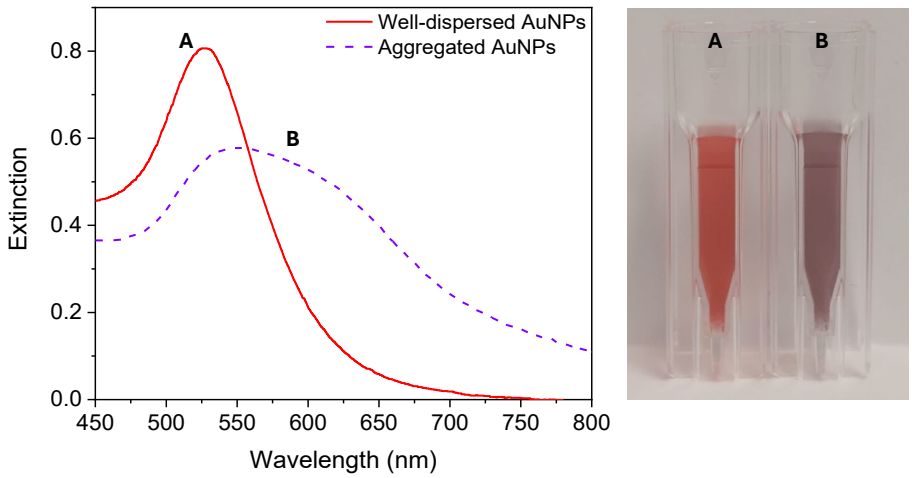

Figure 1.5 a) Absorption bands and corresponding colors of the solution for free AuNPs and b) aggregated AuNPs.

1.5 Colorimetric biosensors based on LSPR: principles and detection strategies

Depending on the origin of the LSPR shift, three main sensing modalities can be distinguished: aggregation-based, refractive-index-based (RI) and disaggregation-based sensors.

The first group exploits the drastic colorimetric response induced by nanoparticle aggregation, driven by near-field electromagnetic coupling. As the inter-particle distance decreases below the particle diameter, a significant redshift of the LSPR peak occurs [66]. This phenomenon enables highly sensitive, label-free detection: when two populations of metal nanoparticles are functionalized with complementary biomolecules, their specific biochemical interaction will induce aggregation and a color change [67].

In contrast, RI sensors rely on the subtle, but quantifiable LSPR peak shift induced by changes in the local dielectric environment surrounding the nanostructure. Binding events, such as protein adsorption or ligand-receptor recognition, alter the effective refractive index at the nanoparticle surface, resulting in a measurable spectral shift [68]. While often requiring instrumentation for precise quantification, RI sensors offer excellent specificity and are well-suited for real-time, label-free monitoring [69].

Recently, disaggregation-based sensors have been developed as a powerful complementary strategy. In these systems, nanoparticles are first assembled into aggregates, which produce a red-shifted LSPR and a characteristic color (typically purple or blue for AuNPs). When the target analyte is introduced, it either cleaves a linker, competes for binding, or enzymatically degrades a crosslinker. As a result, the aggregates dissociate, the LSPR peak shifts back toward that of the dispersed nanoparticles, and the solution color reverts to its original state [70,71].

1.6 AuNPs: the ideal platform for LSPR-based colorimetric biosensing

Typical materials for plasmonic applications are noble metals, among them AuNPs has emerged as the most used platform for LSPR biosensing. Even though silver displays sharper and more intense LSPR bands than gold, the higher chemical stability of gold nanostructures has favored its preferential use in biosensing [72].

AuNPs combine exceptional stability, high conductivity, and a large surface-to-volume ratio, making them excellent platforms for coupling biorecognition elements with signal transduction in biosensing. They are chemically inert, biocompatible, and generally considered among the least toxic metal nanoparticles, which underpins their widespread use in biomedical applications. Their surface can be readily functionalized with proteins, nucleic acids, drugs, dyes, antibodies, or enzymes, conferring specific recognition capabilities. Size, shape, and surface modifications strongly influence their sensitivity and selectivity [73].

In the following chapter, we will discuss the synthesis, functionalization, and optical characterization of gold nanoparticles, exploring how their structural and chemical design can be tailored to optimize sensitivity and selectivity in colorimetric biosensing applications.

Chapter 2 — Gold nanoparticles (AuNPs) as a versatile platform for nucleic acid-based colorimetric biosensing

2.1 Gold nanoparticles as platform

Gold nanoparticles (AuNPs), also known as colloidal gold, consist of gold particles with diameters ranging from 1 to 100 nm, typically stabilized by capping agents such as sodium citrate. Due to their unique optical and electronic properties [74], as well as their high biocompatibility [75], AuNPs have attracted significant attention in fields such as biosensing [73], diagnostics [76], and nanotechnology [77]. Their history dates to 1857 when Michael Faraday first synthesized colloidal gold by reducing a chloroauric acid solution with phosphorus in a two-phase system of water and carbon disulfide [78].

In the first chapter, we introduced the LSPR phenomenon and explained why AuNPs are the most used metallic nanoparticles due to their unique proprieties including strong optical response, high stability and biocompatibility. In this work, AuNPs were selected as the platform for the development of two different colorimetric biosensors, both employing nucleic acids as the recognition element. The first step in constructing these biosensors was the synthesis of AuNPs. Nanoparticles fabrication generally follows two primary approaches: top-down and bottom-up methods [79]. In bottom-up synthesis, nanoparticles are assembled from atomic or molecular precursors. In contrast, top-down methods involve breaking down bulk gold into nanoparticles. Techniques such as sonolysis [80], chemical vapor deposition [81], and radiolys [82] are less frequently used due to their complexity and cost, though they have the advantage of producing AuNPs with fewer impurities. Among bottom-up approaches, the Turkevich's method [83] is one of the most widely used for gold nanoparticle synthesis. It is relatively simple and reproducible for obtaining spherical particles in the 10–30 nm range. The principle of this method is based on the reduction of gold ions (Au^{3+}) to produce gold atoms (Au^{0}) using reducing agents such as trisodium citrate, ascorbic acid, amino acid, and polymers [84]. However, the particles become less spherical, the size distribution becomes wider, and the results are less reproducible for the synthesis of AuNPs above 30 nm in size [85]. Further, this method was modified in 1973, by Frens, to obtain AuNPs within a range of 15 to 150 nm. This was achieved by using different concentration ratios of reducing agents [84]. In this

study, we employed a modified version of the Turkevich's method to synthesize the AuNPs used in our biosensors. The details of the synthesis procedure, along with the characterization of the synthesized AuNPs, are presented in the following sections.

2.2.1 Synthesis of AuNPs

A volume of 1 mL of $HAuCl_4 \cdot 3H_2O$ (25.4 mM) was spiked in 80 mL of ultrapure water under vigorous stirring and the solution was warmed at 150 °C. During the boiling, 3 mL of sodium citrate (80 mM) was added into the solution by holding the same temperature and vigorous stirring for 20 min. Meanwhile, the colour of the solution changed from yellowish to dark and then bright red. Thus, the beaker was moved on a cold plate, by holding the stirring for 2 h. Eventually, the colloidal solution exhibits an OD of ~0.6 at 450 nm corresponding to a concentration of 6×10^{10} AuNPs/mL for 20 nm diameter AuNPs [86,87]. Aiming at removing the sodium citrate surrounding the AuNPs thereby allowing them to be functionalized, a volume of 1 mL of citrate-stabilized AuNPs was centrifuged for 30 min at 6500 g. After the centrifugation, the pellet was re-suspended in 1 mL ultrapure water. Afterward, the AuNP colloidal solution was stored in dark conditions at 4°C.

2.2.2 AuNPs Characterization

The AuNPs were then extensively characterized to confirm their optical, dimensional, and surface properties. UV-Vis spectroscopy was employed to monitor the LSPR peak (Figure 2.1a), confirming the expected spectral profile of well-dispersed AuNPs. Dynamic Light Scattering (DLS) analysis provided quantitative measurements of the hydrodynamic diameter (30 nm), supporting the uniformity of particle size distribution (Figure 2.1b). Additionally, ζ-potential analysis confirmed the colloidal stability of the nanoparticles, showing a surface charge of −35 mV. (Figure 2.1c). To further validate their morphology, Transmission Electron Microscopy (TEM) images were acquired by depositing the AuNPs on a depositing the AuNPs on a gold sheet with very low roughness, so that a high-contrast image could be achieved. Figure 2.1d confirms that the AuNP size distribution is quite narrow with an average value for the diameter of ≈ 25 nm. The TEM micrograph images clearly confirmed both the spherical shape and consistent size of the synthesized particles.

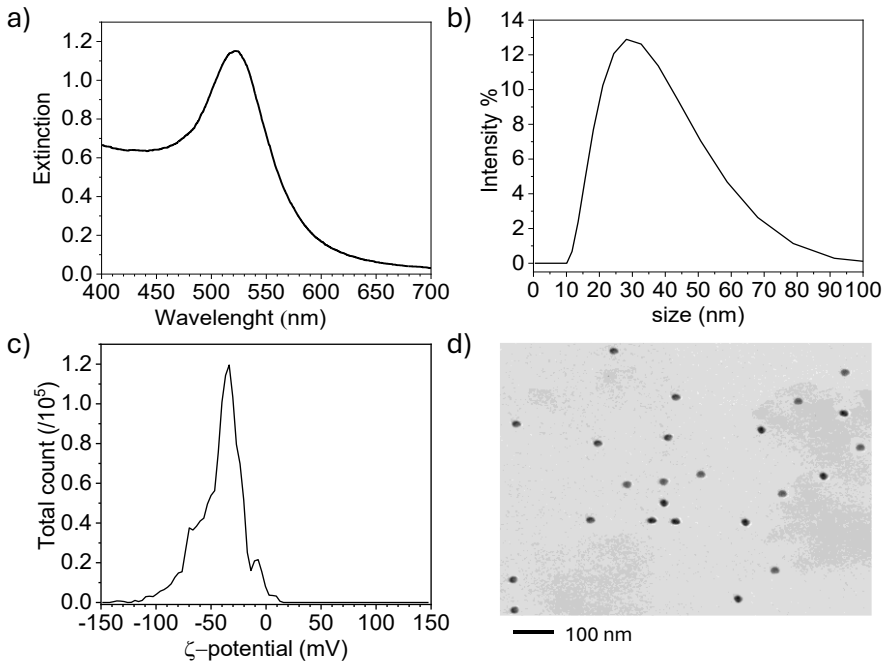

Figure 2.1. a) Extinction spectrum of the synthesized AuNPs, showing a well-defined plasmon resonance peak centered at 522 nm, indicative of mono dispersity and colloidal stability. b) Dynamic Light Scattering (DLS) analysis confirms a narrow size distribution with an average hydrodynamic diameter of approximately 25 nm. c) ζ-potential measurements reveal a surface charge of –35 mV, indicating strong electrostatic repulsion and high colloidal stability. d) Transmission Electron Microscopy (TEM) micrographs further confirm the spherical morphology and uniform size distribution of the gold nanoparticles.

2.3 Surface biofunctionalization

A key challenge in the application of metal nanoparticles in biosensing lies in the biofunctionalization of the active surface, as this process deeply affects both the sensitivity and specificity [72]. The surface properties of nanoparticles directly govern the loading efficiency of functionalizing molecules, which in turn has a profound impact on their performance in biological contexts. Due to their high surface affinity, biomolecules such as proteins readily adsorb onto nanoparticle

surfaces, a phenomenon that must be carefully controlled or exploited depending on the intended application [88].

Following synthesis, functionalization of AuNPs is essential to enhance their utility across different applications. Proper functionalization improves colloidal stability and ensures compatibility with aqueous and physiological environments [89]. AuNPs can be modified with a wide variety of chemicals ligands and biomolecules (proteins, peptides, antibodies, carbohydrates, and nucleic acids) each conferring specific functionalities for targeted sensing or therapeutic purposes.

For nucleic acids (NAs), functionalization strategies fall into two broad categories: covalent and non-covalent approaches [90]. The choice between them depends on factors such as NA type, required conjugate stability, and application conditions.

Non-covalent conjugation relies on intrinsic molecular interactions such as electrostatic attraction, hydrogen bonding, π-π stacking, and hydrophobic forces [91]. These methods are cost-effective and preserve the native structure and function of NAs without chemical modifications. However, they typically yield less stable conjugates, prone to dissociation under varying pH or ionic strength [92]. In contrast, covalent attachment ensures a robust linkage between NAs and nanoparticle surfaces, thereby preserving the integrity and functionality of both components even under biologically relevant conditions. Common covalent strategies include, amide bond formation, thioether linkages, disulfide bridges and Au–S bonds. Au–S bond is by far the most widely used strategy for functionalizing AuNPs with NAs [93]. It exploits the strong affinity of thiols for gold, enabling highly stable conjugates through semi-covalent Au–S bonding (bond energy ≈ 45 kcal/mol [94]). Thiolated NAs, typically modified at the 5′ or 3′ terminus, anchor reliably to AuNPs, offering high stability and reproducibility for applications involving aptamers or ssDNA.

To achieve efficient and reproducible conjugation via Au–S bonds several methods have been developed and optimized. These include direct adsorption, the salt-aging method, the low-pH method, freeze-thaw, and the dehydrated “solid solution” method. Each offers distinct kinetic and thermodynamic advantages depending on the desired conjugate density, particle size, and downstream application.

2.3.1 Methods to obtain Au-S bound

As previously discussed, multiple strategies have been developed to link the NAs to the AuNPs surfaces through Au-S bound. Although thiolated NAs can, in principle, bind directly to AuNPs through this strong semi-covalent interaction, simple mixing in aqueous solution typically yields suboptimal surface coverage. This limitation stems from electrostatic repulsion between the negatively charged phosphate backbones of adjacent NA strands, which hinders dense packing on the nanoparticle surface [95].

To overcome this, several advanced functionalization protocols have been developed as shown in Figure 2.2. The first and most widely adopted method, introduced by the Mirkin group [96], is the salt-aging technique. Here, electrostatic repulsion between NA strands and citrate-capped AuNPs is gradually screened by the stepwise addition of salt (typically NaCl). The final concentration of salt that must be reached is 1 M. Critically; salt must be added slowly; abrupt introduction of high concentrations can cause irreversible AuNP aggregation due to charge neutralization and loss of colloidal stability[95]. While highly effective for forming dense, well-ordered DNA monolayers, salt aging is time-consuming, often requiring 24–48 hours.

To enable faster functionalization, alternative methods have emerged. One is the low-pH method. At acidic pH (~3.0), the phosphate backbone becomes partially protonated, reducing its net negative charge. Nucleobases such as adenine and cytosine may also acquire partial positive charges, enhancing interaction with the negatively charged citrate-stabilized AuNP surface. Simultaneously, citrate capping agents protonate, weakening their repulsive barrier and allowing thiolated NAs to bind rapidly, often within minutes. However, efficiency can be sequence-dependent, as protonation and charge distribution vary with nucleobase composition [97].
Another rapid and highly efficient technique is the freeze–thaw method [98]. During freezing, pure water forms ice crystals, excluding solutes like salts, DNA, and AuNPs. into interstitial regions. This creates a eutectic phase with near-saturated salt concentration [99]. Locally increasing ionic strength and molecular crowding. These conditions effectively screen electrostatic repulsions and accelerate thiol–gold binding. Remarkably, complete functionalization can occur in as little as two minutes, without adding external reagents or buffers [100].

Recently, a new ultrafast method called INDEBT (Instant Dehydration in Butanol) was reported for achieving ultra-dense AuNP functionalization with NAs [101]. It rapidly functionalizes AuNPs by dehydrating a mixture of AuNPs and thiol-NAs in butanol, which concentrates and compresses the molecules, suppresses charge repulsion, and accelerates the Au–S bond formation. Upon water reintroduction, the molecules redistribute, yielding stable, high-density DNA-functionalized AuNPs in seconds—making the process simple, fast, and suitable for high-throughput applications [102].

In this work, two distinct functionalization strategies were selected based on the specific requirements of each biosensing platform. For one biosensor, we used simple adsorption, a straightforward approach suitable for applications where moderate surface density and rapid preparation are prioritized. For the other biosensor, we implemented the freeze–thaw method to achieve rapid, and controlled functionalization density without introducing additional chemical components.

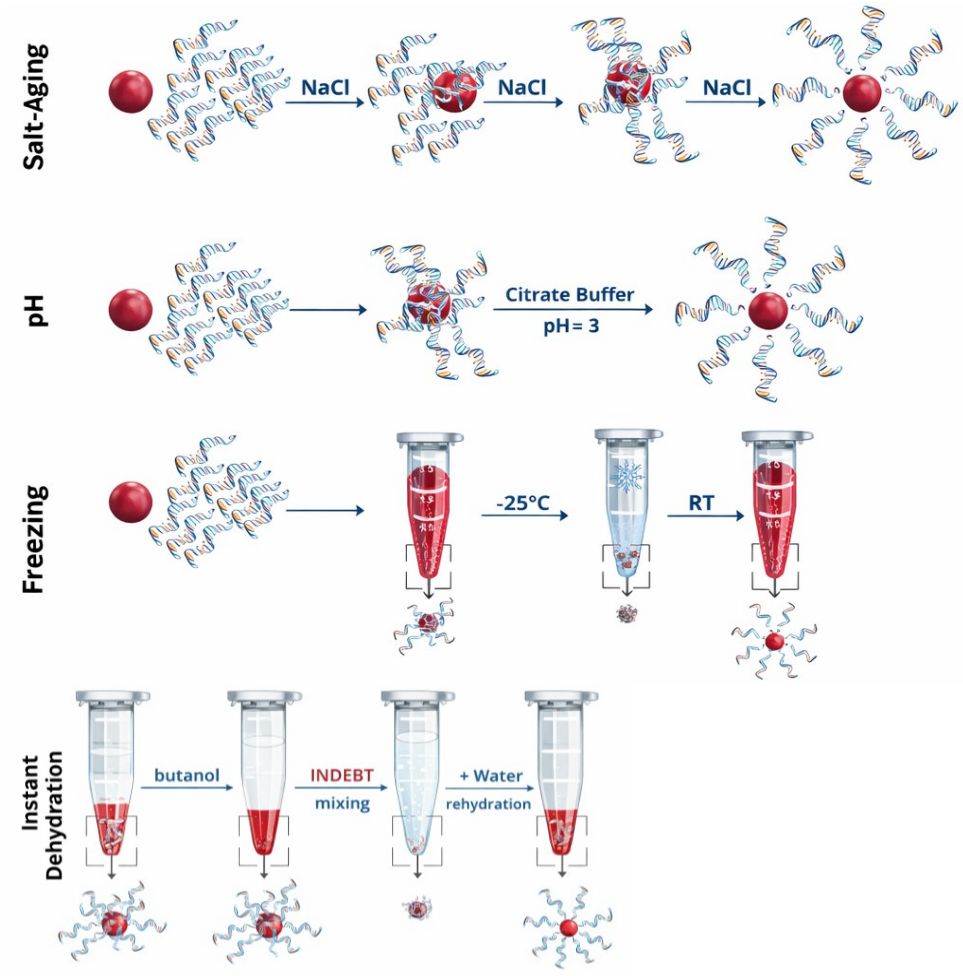

Figure 2.2 Functionalization methods of AuNPs with HS-oligos, resulting in Au-nanoprobes [103].

2.4 Biorecognition elements: aptamers and ssDNA probes

The core functionality of any biosensor lies in its ability to selectively recognize the target analyte, a task entrusted to the biorecognition element. In nucleic acid-based biosensing, two major classes of recognition ligands dominate the field: aptamers (RNA or DNA oligonucleotides), which bind complex biomolecular or cellular targets through structural complementarity, and single-strand DNA (ssDNA)

probes, which rely on sequence-specific hybridization for nucleic acid detection.

In this work, we strategically employed these two distinct biorecognition paradigms to address two fundamentally different analytical challenges: the detection of intact breast cancer-derived exosomes and environmental DNA (eDNA).

2.4.1 RNA aptamers for exosome detection

Aptamers are short, single-strand oligonucleotides (DNA or RNA) that fold into specific tertiary structures, enabling high-affinity and high-specificity binding to different molecular targets [104,105]. They are typically generated through the SELEX (Systematic Evolution of Ligands by EXponential enrichment) [106]. Owing to their rapid selection, low production cost, minimal batch-to-batch variability, ease of chemical modification, and superior thermal stability, aptamers are widely used in basic research, environmental monitoring, food safety, and increasingly in clinical diagnostics and therapeutics [106].

In this work, aptamers were used to target exosomes. Exosomes are extracellular vesicles (EVs) of 50–150 nm diameter, released by most cell types in biological fluids. Exosomes display surface proteins derived from their cell of origin, including tumor-specific markers, making them powerful, non-invasive biomarkers for early cancer detection and disease monitoring [107]. Notably, breast cancer cells release abundant, cell-specific exosomes that are stable, readily accessible from body fluids, and ideal for liquid biopsy–based diagnostics [108].

For selective capture of breast cancer-derived exosomes, a 30-mer RNA aptamer ex.50.T was previously selected via Exo-SELEX for its specific recognition of breast cancer (BC) derived exosomes [109]. This aptamer targets Gremlin 1 (GREM1), a protein overexpressed on the surface of BC-derived exosome, making it a valuable biomarker for non-invasive diagnostic [110]. The aptamer exhibits a dissociation constant (Kd) of approximately 37.7 nM for GREM1, confirming strong binding affinity.

The sequence of the aptamer employed is:
(5'-(2'F-U)G(2'F-U)GG(2'F-C)AG(2'F-U)(2'F-U)AAGAA(2'F-U)A GA(2'F-U)(2'F-C)(2'F-U)(2'F-U)(2'F-C)G(2'F-C)(2'FU)G(2'F-C)GA (2'F-U)(2'F-U)-Thiol-C6-3')

All pyrimidines (U, C) were substituted with 2'-fluoro (2'F) to enhanced nuclease resistance and binding affinity while purines (A, G) remain unmodified. A 3′-thiol modification (C6-SH) enables covalent immobilization onto AuNPs via Au–S chemistry, a critical step in biosensor functionalization.

2.4.2 ssDNA probes for environmental DNA (eDNA) detection

Single-stranded DNA (ssDNA) probes are synthetic oligonucleotides designed to recognize complementary target sequences through Watson-Crick hybridization [111]. Owing to their high sequence specificity, chemical stability, low cost, and ease of synthesis and modification, ssDNA probes are widely employed in biosensors for nucleic acid detection as: disease diagnosis [112], food security [113], pathogen identification and environmental monitoring [114].

In this work, ssDNA probes were selected to detect eDNA, fragments of genetic material shed by organisms (via skin, feces, mucus, or cell debris) into their surrounding environment (water, soil, air) [115]. eDNA has emerged as a powerful, non-invasive tool for biodiversity monitoring, detection of invasive or endangered species, and assessment of ecosystem health, eliminating the need for direct observation or capture of target organisms.

We focused on *Fusarium oxysporum*, a soilborne fungal pathogen that causes destructive vascular wilt and is one of the most widespread and economically important phytopathogens in agricultural systems worldwide [116,117].

The first step was the definition of the target sequence. A single conserved region was identified by querying the NCBI database for the Internal Transcribed Spacer 1 (ITS1) of Fusarium oxysporum, flanked by the 18S and 5.8S ribosomal RNA genes, Internal Transcribed Spacer 2 (ITS2), and Large Subunit ribosomal RNA gene (LSU) of fungi belonging to the genus *Fusarium*. All available sequences of *F. oxysporum* were retrieved, while three representative sequences for approximately 100 additional *Fusarium* species were included for comparison. The sequences were imported into MEGA7 and aligned using the ClustalW algorithm. After alignment, excessively long regions were trimmed, and the sequences were visually inspected to identify a 20 bp sequence conserved among all *F. oxysporum* accessions and differing by at least two bases from other *Fusarium* species.

Once the target sequence was defined, we designed two probes based on this sequence and its complementary strand. Both were synthesized with a 5′-thiol modifier linked via a C6 spacer to enable covalent immobilization onto AuNPs [118]. An additional 10-base spacer (poly-A and poly-C) was incorporated between the recognition sequence and the thiol anchor to minimize steric hindrance and to enhance target accessibility during hybridization.

2.5 Nucleic acid functionalization for the two biosensing platforms

In this work, two distinct colorimetric nucleic acid-based biosensors were developed, using the same AuNP platform but different biorecognition elements: an RNA aptamer for BC exosome detection and ssDNA for eDNA detection While both rely on Au–S chemistry for surface immobilization, the choice of nucleic acid, functionalization protocol, and target analyte reflect the specific requirements of each application. The experimental optimization and analytical performance of each biosensor are presented in Chapters 3 and 4, respectively.

2.6 Functionalization with RNA aptamer for BC derived exosome detection

2.6.1 SH-RNA aptamer activation, AuNPs functionalization, and surface coverage characterization

The Ex.50.T aptamer was deprotected by incubating 10 mL of aptamer solution (2.5 µg/mL) with 10 µL of 100 mM tris(2-carboxyethyl)phosphine (TCEP) for 1 h at room temperature (RT). The reduced aptamer was then mixed 1:1 (v/v) with citrate-stabilized AuNPs (OD = 4) and incubated under gentle stirring for 30 min to enable covalent Au–S immobilization.

Surface saturation was determined by monitoring the plasmon peak shift via UV-Vis spectroscopy. A stable redshift of ~2 nm indicated maximum surface coverage, achieved at aptamer concentrations above >2 µg/mL. For biosensor fabrication, the aptamer concentration was deliberately set at 1.9 µg/mL, just below saturation, to preserve the nanoparticles' ability to undergo controlled salt-induced aggregation, essential for the target-triggered anti-aggregation mechanism. Importantly, this saturation reflects the completion of the adsorption process under the chosen experimental conditions and does not correspond to full monolayer coverage. According to the effective-medium approximation [119,120], a partially coated AuNP can be modelled as a homogeneous dielectric shell whose refractive index is

$$n_{\mathrm{eff}}(f) = n_{\mathrm{w}} + f(n_{\mathrm{DNA}} - n_{\mathrm{w}}), \quad (4)$$

where *f* is the fractional surface coverage, n_{w}=1.33 is the refractive index of water, and n_{DNA}≈1.46 represents that of the DNA layer [121]. In this regime, the LSPR shift is proportional to the effective index change through the refractive-index sensitivity *S* of the nanoparticle. For spherical AuNPs in the 20–40 nm range, consistent with the particles used here, the reported sensitivity is 60–100 nm/RIU [122]. Taking a representative value *S*≈80 nm/RIU, the measured shift of 2 nm corresponds to an effective index increase $\Delta n_{\mathrm{eff}} \approx 0.025$, i.e. ≈20% of the full index contrast $\Delta n = (n_{\mathrm{DNA}} - n_{\mathrm{w}}) = 0.13$. This yields a surface-coverage estimate *f*≈0.2.

To estimate the number of aptamers per particle, we used the experimentally reported footprint (A_{DNA}) of thiolated ssDNA on 30-nm AuNPs ($A_{\mathrm{DNA}} \approx 11$ nm² per ssDNA molecule) [123], which leads to the maximum loading capacity $N_{\max} = 4\pi R^2 / A_{\mathrm{DNA}} \approx 260$ aptamers. With *f*≈0.2, the actual number of Ex.50.T molecules immobilized under our conditions is *N*≈50 aptamers per nanoparticle. This sparse but stable functionalization provides adequate probe density for target recognition while maintaining the reversible aggregation–disaggregation behavior that underpins the colorimetric response.

Bare AuNPs in water exhibit a characteristic plasmon peak at 520 nm (black curve). After aptamer functionalization, a slight redshift (~1.9 nm, red dotted curve) confirms successful binding while maintaining colloidal stability. (Figure 2.3)

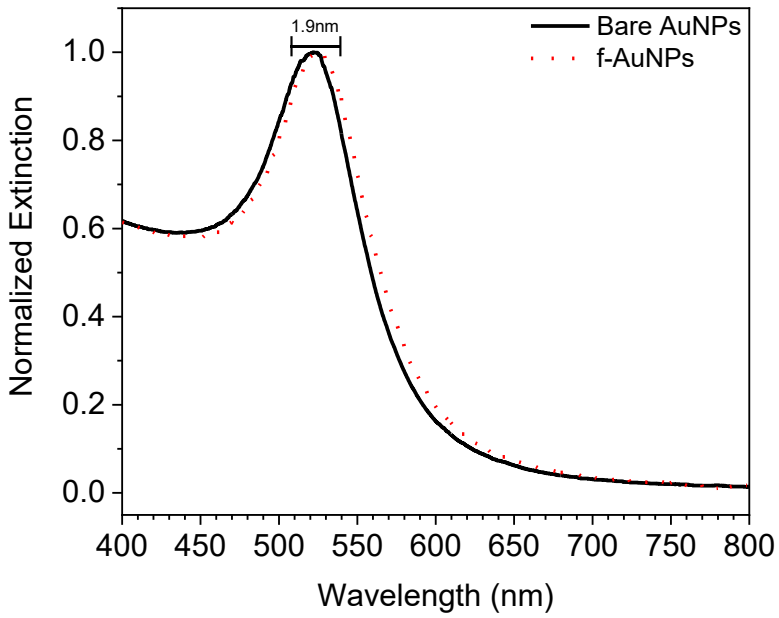

Figure 2.3 Normalized extinction spectra illustrating the formation of the sensing reagent. The black line shows the spectrum of citrate-stabilized gold nanoparticles (AuNPs) in ultrapure water. Functionalization with thiolated aptamers (red dotted line) induces a red shift of approximately 1.9 nm, consistent with surface modification.

2.7 Functionalization with ssDNA for eDNA detection

2.7.1 Probe's thiol group activation and functionalization

Two complementary ssDNA probes targeting the *Fusarium oxysporum* genome were employed:
5'Thiol-AAAAACCCCC TCA AAA CCT CAA TGA GTG CG-3' (*F. oxysporum* probe).

5'Thiol- AAAAACCCCC CGC ACT CAT TGA GGT TTT GA-3' (*F. oxysporum* C_probe).

These ssDNA probes have a C6-SH modification at 5' end so prior to functionalization, thiolated ssDNA was chemically activated by treatment with TCEP at a 100:1 molar ratio (TCEP:ssDNA) for 1 hour at RT to reduce disulfide bonds. The freshly activated ssDNA probe was used immediately after this reduction step.

2.7.2 Conjugation protocol and sequence-dependent optimization of ssDNA:AuNP ratios

AuNPs-ssDNA conjugates were prepared via Au–S bond formation using freeze-thaw technique [98]. Separate batches of AuNPs were functionalized with each probe. After TCEP activation, various ssDNA: AuNP molar ratios (200:1 to 1000:1) were tested. The mixtures were subjected to a brief freeze–thaw cycle, (2 minutes on dry ice followed by thawing at RT).

Functionalization efficiency was assessed by using the absorbance ratio A_{610}/A_{525} which value is 0.2 for fully monodispersed particles and increases upon aggregation [124]. Thus, values below 0.3 are generally considered acceptable [125]. Moreover, it is worth considering that, as shown in Figure 2.4, the optimal ssDNA:AuNP ratio depends on the probe sequence. *F. oxysporum* Probe required a ratio of 300:1 (Figure 2.4a-b), whereas *F. oxysporum* C_Probe required a ratio of 400:1 (Figure 2.4c-d). This sequence dependence can be explained by the tendency of some ssDNA sequences to form secondary structure involving the spacer and the thiol group. When thiolated ssDNA adopts a secondary structure, its attachment efficiency during the functionalization is reduced [126], necessitating a higher ssDNA:AuNP ratio to achieve a certain coverage.

2.7.3 Post-functionalization purification and colloidal stability validation

For this biosensor, we selected an ssDNA:AuNP ratio that yielded an initial absorbance ratio A_{610}/A_{525} of 0.28, a value indicative of acceptable colloidal stability with sufficient probe density. Following functionalization, AuNP–ssDNA conjugates were purified by centrifugation (16,000 g, 4 °C, 10 min) to remove excess unbound ssDNA [127] and resuspended in 5 mM PBS. This step not only eliminated free oligonucleotides but also removed aggregates formed during the freeze–thaw process. Notably, for *F. oxysporum* Probe at a 300:1 ssDNA:AuNP ratio, the A_{610}/A_{525} value decreased from 0.28 (pre-centrifugation) to 0.24 (post-centrifugation) (Figure 2.5), reflecting improved colloidal stability and confirming effective surface functionalization. To investigate how ssDNA surface density affects colloidal behavior, we compared two batches of post- washing f-AuNPs obtained using different ssDNA:AuNP molar ratios: 300:1 (A_{610}/A_{525}= 0.24) and 700:1 (A_{610}/A_{525}= 0.16) (Figure 2.6a). DLS analysis (Figure 2.6b) revealed an average hydrodynamic diameter of 23 nm for bare

AuNPs, increasing to ~45 nm for both functionalized samples but this increase in size depends by different reasons.

In the 700:1 sample, the increase arises from an excess of ssDNA forming a dense, uniform shell around each particle. This provides excellent colloidal stability also confirmed by TEM; (Figure 2.6c), where particles appear identical to bare AuNPs (Figure 2.1d, Section 2.2.2). Thus, DLS analysis confirms the presence of surface-bound DNA, as indicated by an average hydrodynamic size increase of ~20 nm. This increment is consistent with the expected contribution of a 30-base ssDNA strand (~10 nm) extending from each side of the nanoparticle surface, suggesting dense and uniform functionalization.

In contrast, the 300:1 sample shows an increase in hydrodynamic size, which is attributed to dimer formation rather than to the development of a thicker DNA shell. Although the DNA loading is lower than in the 700:1 condition, it is still sufficient for functionalization but insufficient to maintain strong interparticle repulsion, leading to partial nanoparticle aggregation. Dimer formation is further supported by TEM imaging (Figure 2.6d). These results suggest that while a high DNA excess (700:1) maximizes colloidal stability, it may limit probe accessibility, whereas a 300:1 ratio provides a more balanced compromise between stability and functional performance.

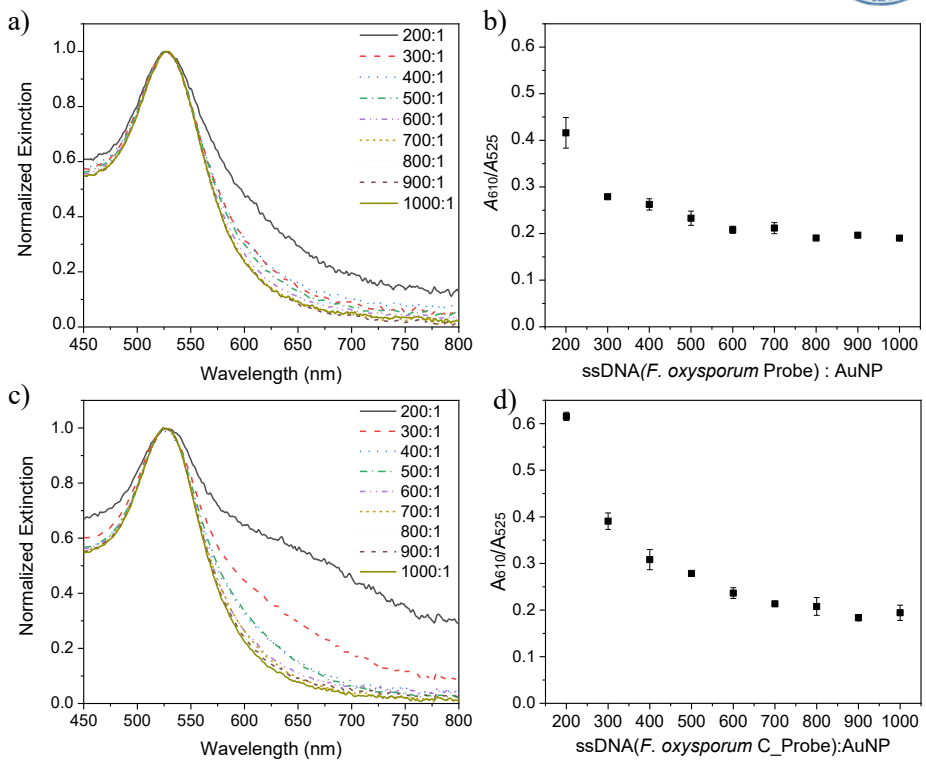

Figure 2.4 Functionalization efficiency measurements: a) Normalized UV-Vis spectra of AuNPs functionalized using different ssDNA:AuNP ratios. b) Plot of the A_{610}/A_{525} absorbance ratio for *F. oxysporum* Probe showing that a ssDNA:AuNP ratio of 300:1 is required to obtain a value of 0.28. c) Normalized UV-Vis spectra of AuNPs functionalized using different ssDNA:AuNP ratios. (*F. oxysporum* C_Probe). d) Plot of the A_{610}/A_{525} absorbance ratio for *F. oxysporum* C_Probe showing that a ssDNA:AuNP ratio of 400:1 is required to obtain a value of 0.28. All error bars in the figures represent the results of duplicate experiments.

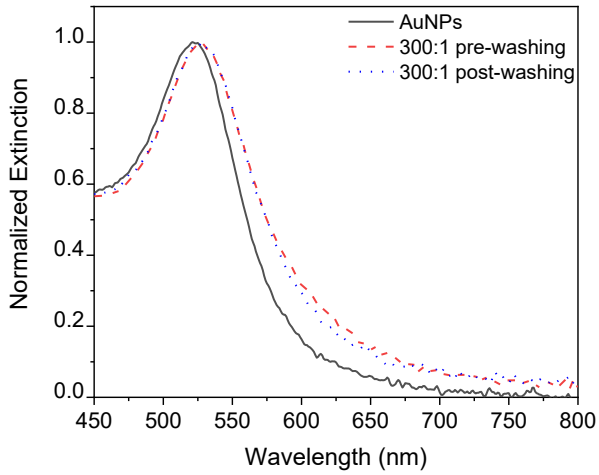

Figure 2.5 Effect of post-functionalization centrifugation on f-AuNPs. Normalized UV–Vis extinction spectra of AuNPs functionalized with the *F. oxysporum* Probe at a 300:1 ssDNA:AuNP molar ratio, measured pre and post centrifugation. The A_{610}/A_{525} ratio decreases from 0.28 to 0.24. indicating removal of aggregates or dimers formed during functionalization due to non-excess ssDNA coverage.

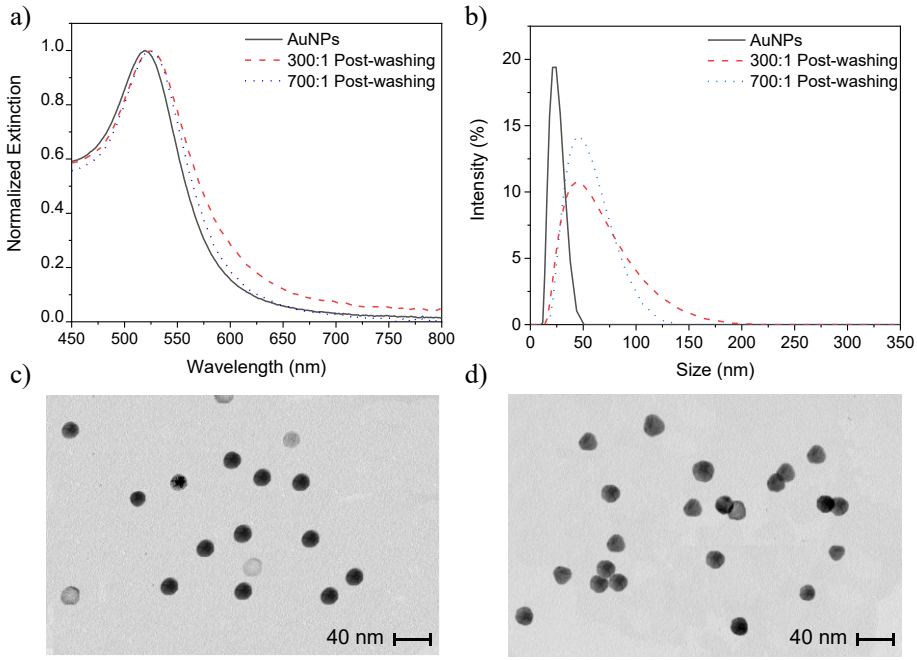

Figure 2.6 Characterization of f-AuNPs (functionalized with *F. oxysporum* Probe). a) UV–Vis extinction spectra of f-AuNPs prepared at ssDNA:AuNP molar ratios of 300:1 and 700:1. b) DLS analysis showing an increase in hydrodynamic diameter for both samples, arising from different causes: a dense ssDNA shell for the 700:1sample versus dimer formation for the 300:1 sample. c) TEM image 700:1 sample, showing well-dispersed colloidal suspension d) TEM image of the 300:1 sample, revealing the presence of dimers.

2.7.4 Quantification of ssDNA surface coverage and interstrand spacing

To investigate the impact of the DNA loading ratio, we estimated the AuNPs surface coverage by calculating the number (*N*) of ssDNA strands attached per nanoparticle for both functionalization ratios (300:1 and 700:1), according to the method described in[128]. We determined the DNA loading density on AuNPs by comparing the initial ssDNA concentration with the concentration remaining in the supernatant after centrifugation (i.e., unbound DNA). Dividing the bound DNA (in moles) by the number of nanoparticles yields the number of DNA strands per AuNPs:

$$N = \frac{C_{Added} - C_{Free}}{C_{AuNPs}} \qquad (5)$$

In Equation (4), C_{Added} is the concentration of the ssDNA added to the colloidal solution, C_{Free} is the concentration remaining in the supernatant after centrifugation, and C_{AuNPs} is the concentration of the AuNPs. For a molar ratio 300:1, we obtained $N \approx 220$, and for molar ratio 700:1, $N \approx 370$.

Once N values were obtained, the area A_{ssDNA} occupied by a ssDNA was calculated as:

$$A_{ssDNA} = \frac{\pi d^2}{N} \qquad (6)$$

where d is the AuNP diameter. The resulting values are $A_{ssDNA} = 6.0$ nm^2 for the 300:1 sample and $A_{ssDNA} = 3.5$ nm^2 for 700:1 sample.

The calculated N and A_{ssDNA} values for the 300:1 and 700:1 batches confirm a higher ssDNA surface density and reduced inter-strand spacing in the 700:1 batch, indicating increased surface coverage, thereby promote steric hindrance and potentially reducing hybridization efficiency. The specific values used in the formulas above are provided in following table.

ssDNA:AuNP	Cadded (μM)	V (μL)	Cfree (μM)	CAuNP (μM)	*N*	A_ssDNA (nm^2)
300:1	40	3	0.3	0.04	≈220	≈6.0
700:1	40	7	1.2	0.04	≈370	≈3.5

Table 1. Estimation of ssDNA surface coverage on AuNPs. Parameters used to calculate the number of ssDNA strands per gold nanoparticle and the corresponding surface area occupied by each strand. As expected, increasing the ssDNA:AuNP molar ratio results in higher DNA loading per particle and a reduced average surface area available per strand.

2.8 Transition to experimental work

The functionalization and design of the two nucleic acid–based colorimetric biosensors, one based on an RNA aptamer and the other

on single-stranded DNA (ssDNA), have been outlined in this chapter. The detection mechanisms, experimental implementation, optimization, and analytical validation of each platform are presented in the following chapters: Chapter 3 for the aptamer-based biosensor and Chapter 4 for the ssDNA-based biosensor.

Chapter 3 — A colorimetric aptasensor for exosome detection in breast cancer liquid biopsy

3.1 The clinical need for non-invasive and early-stage breast cancer detection

Breast cancer (BC) is the most common cancer and a leading cause of cancer-related mortality in women worldwide, with over 450,000 deaths annually [129]. Early detection is critical, as it dramatically improves prognosis and survival rates. When detected at an early stage, the five-year relative survival rate for breast cancer is approximately 99%, compared to only 27% when the disease has metastasized [130]. The stage at diagnosis strongly influences the therapeutic success, underscoring the urgent need for methods that enable early, non-invasive, and cost-effective detection strategies [131].

Mammography is widely used for breast cancer screening in high-income countries, yet its benefits and limitations remain the subject of ongoing international debate [132,133]. Key concerns include exposure to ionizing radiation, which may contribute to carcinogenesis, and overdiagnosis, with estimates ranging from 0% to 40–50% depending on screening age and methodology. Furthermore, mammography has limited sensitivity for small cancer and reduced accuracy in women with dense breast tissue [134].

Definitive diagnosis typically requires needle or surgical biopsy, which is not only invasive but also not necessary in most cases when tumors are benign [135]. Consequently, significant research efforts have focused on identifying non-invasive biomarkers in easily accessible body fluids. In this context, liquid biopsy has emerged as a particularly promising approach for improving BC screening [136]. However, it faces two major challenges: the identification of suitable biomarkers and the development of detection methods that are both reliable and cost-effective.

Exosomes are gaining significant attention as liquid biopsy biomarkers due to their molecular cargo, which reflects the physiological and pathological state of their cell of origin[137]. They play a critical role in intercellular communication and cancer progression, making them ideal candidates for non-invasive diagnostics.

To address this clinical need, we developed a colorimetric aptasensor based on the platform described in Chapter 2. The following sections present the detection mechanism and experimental validation of this

biosensor for the detection of breast cancer-derived exosomes, including its binding affinity toward the target protein (GREM1), recognition of purified exosomes, analytical performance in complex biological matrices, and specificity against non-target analytes.

3.2 Anti-aggregation-based detection

Although the anti-aggregation approach has traditionally been applied to small analytes (e.g., metal ions) through electrostatic interactions [138,139], this work adapts the strategy for large biological targets such as EVs. Recognition is mediated by a high-affinity, structure-switching aptamer (Ex.50.T-SH) that specifically binds GREM1 on the exosome surface, enabling selective disaggregation even in complex biological matrices. As shown in Figure 3.1, the sensing mechanism begins with AuNPs functionalized with the thiolated Ex.50.T aptamer. Controlled aggregation is then induced by adding 40 µL of 1 M NaCl to 1 mL of the functionalized AuNPs, yielding a stable clustered reagent, as confirmed by UV–Vis absorption spectroscopy (Figure 3.2a) and by TEM (Figure 3.2b).

When the aggregated system is exposed to serum containing GREM1 positive EVs, the specific aptamer–target interaction triggers a conformational change that disrupts the nanoparticle clusters. This disaggregation produces a measurable shift in the plasmonic extinction spectrum.

For each measurement, serial dilutions of EVs in 1x PBS were prepared and mixed (1:1, v/v) with an equal volume of these pre-aggregated f-AuNPs dispersed in ultrapure Milli-Q water, yielding a final reaction medium composed of 50% PBS and 50% water. Following sample addition, the mixture was incubated at room temperature for 10 min. Extinction spectra were acquired immediately thereafter, resulting in a total assay time of 10 min.

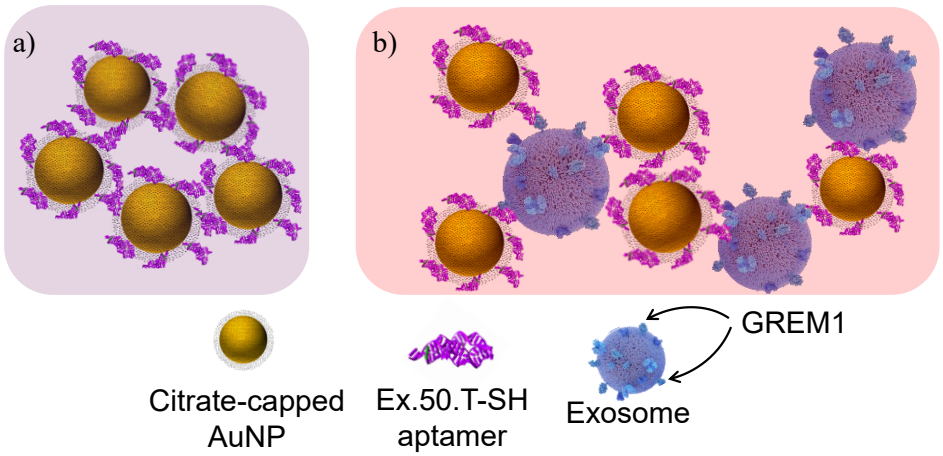

Figure 3.1 a) Functionalized Gold nanoparticles (f-AuNPs) are aggregated by the controlled addition of NaCl b) Upon exposure to serum containing GREM1 expressing exosome, the specific aptamer-target interactions promote nanoparticles disaggregation, resulting in a measurable change in the extinction spectrum.

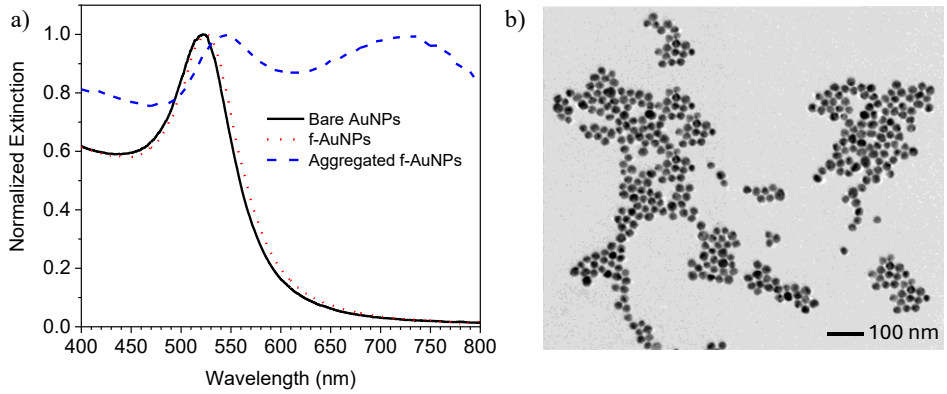

Figure 3.2 a) Normalized extinction spectra illustrating the formation of the sensing reagent. The black line shows the spectrum of citrate-stabilized gold nanoparticles (AuNPs) in ultrapure water. Functionalization with thiolated aptamers (red dotted line) induces a red shift of approximately 1.9 nm, consistent with surface modification. Addition of NaCl (blue dashed line) triggers nanoparticle aggregation, leading to a broad extinction profile characteristic of the final reagent used in the anti-aggregation assay. b) Transmission Electron Microscopy (TEM) image showing the formation of gold nanoparticle aggregates resulting from the addition of NaCl.

3.3 Interaction between GREM1 and aptamer functionalized AuNPs

After functionalizing the AuNPs with the selected aptamer (see Chapter 2, Section 2.6.1), we first verified the aptamer's ability to specifically bind GREM1 using a preliminary aggregation-based assay. In this setup, increasing concentrations of recombinant GREM1 in 1×PBS were added to aptamer-functionalized AuNPs (f-AuNPs) dispersed in ultrapure water, in the absence of added salt. As GREM1 induced nanoparticle aggregation, the extinction spectra (Figure 3.3a) showed a progressive red shift and a concomitant increase in the integrated absorbance between 530 and 800 nm—spectral features characteristic of plasmonic coupling. Quantification based on this integrated signal (Figure 3.3b) yielded a limit of detection (LOD) of approximately 10 ng/mL.

Although this aggregation-based format differs from the anti-aggregation strategy employed in the final biosensor (Section 3.2), it served as an initial proof of concept for aptamer–GREM1 recognition. However, the obtained LOD exceeds typical circulating levels of soluble GREM1 in human serum. Indeed, literature reports indicate that free GREM1 concentrations remain below 2.0 ng/mL in healthy individuals and only rise to ~14–15 ng/mL in patients with Idiopathic Pulmonary Fibrosis [140]. To evaluate the relevance of soluble GREM1 in our intended diagnostic context (breast cancer), we measured its levels in both non-tumoral and breast cancer (BC) serum samples using a commercial ELISA kit. As shown in Figure 3.4, GREM1 concentrations in all samples were consistently <2.0 ng/mL—well below the LOD of the aggregation assay—and no statistically significant difference was observed between tumoral and non-tumoral groups.

These findings support the design choice to target exosome-bound GREM1 rather than its soluble form. In the final assay (Section 3.2), signal generation relies on an anti-aggregation mechanism driven by affinity competition: the aptamer preferentially binds GREM1 exposed on the exosome surface, thereby disrupting non-specific interparticle interactions and promoting AuNP dispersion. Consequently, any optical response observed in complex biological matrices (Section 3.5) can be confidently attributed to the specific recognition of exosome-associated GREM1, not to interference from soluble protein.

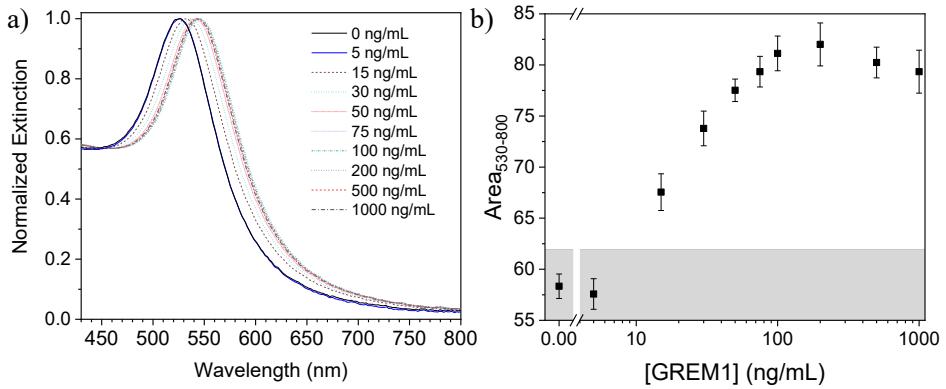

Figure 3.3. Functionalized gold nanoparticles were dispersed in ultrapure water and mixed with recombinant GREM1 (R&D System) diluted in 1X PBS at various concentrations. a) Normalized extinction spectra at increasing GREM1 concentrations. b) Integrated area in the 530–800 nm spectral range plotted against GREM1 concentration. The shaded region represents the baseline calculated with the 3SD method at the zero-concentration (blank) and leads to a minimum detectable concentration of approximately 10 ng/mL.

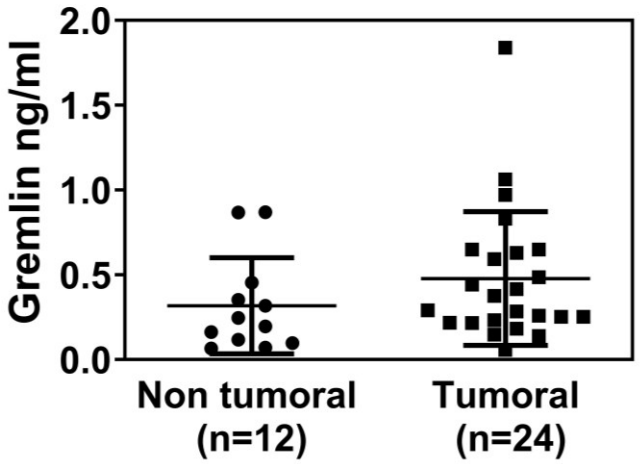

Figure 3.4. GREM1 levels in serum samples from breast cancer patients and non-tumoral controls, as measured by antibody-based ELISA. No statistically significant difference was observed between the two groups (p = 0.2203). Dot plot shows individual measurements in total serum.

3.4 Interaction between GREM1 and purified exosomes

Once confirmed the aptamer's ability to recognize GREM1, we implemented the complete anti-aggregation sensing strategy using purified EVs isolated from breast cancer serum samples. The initial EVs concentration was quantified by nanoparticle tracking analysis (NTA). The data confirm the size distribution and particle concentration ($\approx 10^{10}$ particles/mL) consistent with typical EV populations (Figure 3.5).

For each measurement, serial dilutions of EVs suspended in 1×PBS were prepared and mixed (1:1, v/v) with an equal volume of pre-aggregated f-AuNPs dispersed in ultrapure Milli-Q water (Figure 3.2b), resulting in a final reaction medium composed of 50% PBS and 50% water. The extinction spectra obtained at different EV concentrations are shown in Figure 3.6a. All spectra were normalized to the intensity of the primary plasmonic peak located at approximately 530 nm to allow for comparison of their shape across the 530–800 nm range. A clear reduction in spectral intensity at longer wavelengths was observed as the exosome concentration increased, consistent with the disaggregation of salt-induced nanoparticle clusters triggered by target binding. This behavior was quantified by calculating the integrated area in the 530–800 nm range of the normalized spectra (Figure 3.6b), yielding a well-defined dose–response curve.

The horizontal reference line in the graph corresponds to the area measured for f-AuNPs in ultrapure water, which closely matches the zero-concentration condition in PBS, confirming that the buffer does not contribute to non-specific aggregation. The limit of detection was determined using the standard signal-to-noise criterion (S/N = 3), where the signal corresponds to the spectral response and the noise is defined as the standard deviation of the control (Figure 3.6b). Under these conditions, the LOD was estimated to be approximately 10^6 EVs/mL, confirming the sensitivity and analytical reliability of the anti-aggregation assay in purified systems.

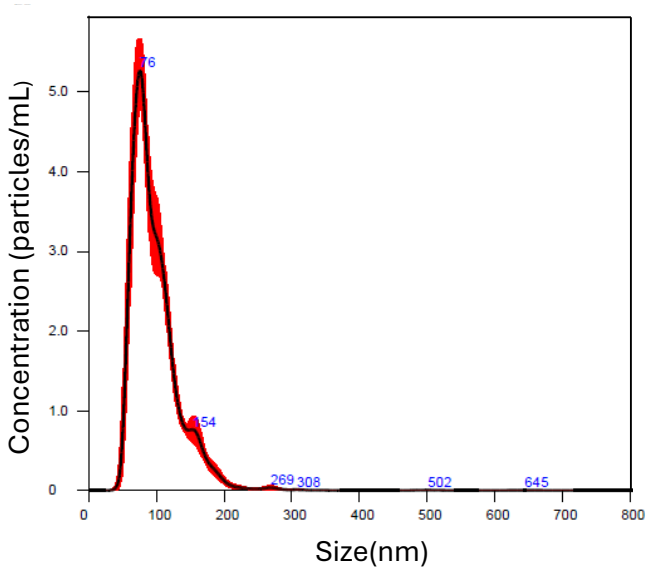

Figure 3.5 Nanoparticle Tracking Analysis (NTA) profiles of a representative sample of extracellular vesicles (EVs) isolated from tumoral human serum. The data confirm a size distribution and particle concentration (≈10^{10} particles/mL) consistent with typical EV populations, supporting the quality and reproducibility of the isolation process.

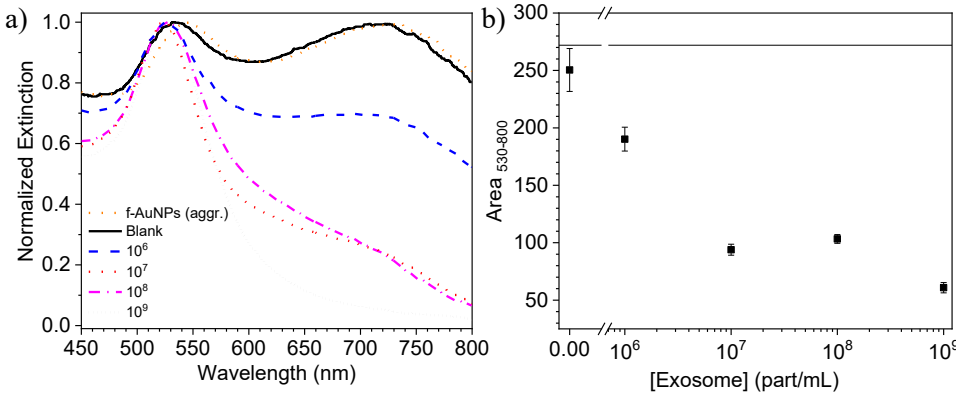

Figure 3.6 Anti-aggregation response of f-AuNPs to breast cancer exosomes. a) Normalized extinction spectra showing disaggregation with increasing exosome concentration (main peak at ~520 nm). Blank = aggregated f-AuNPs. b) Integrated area (530–800 nm) vs. exosome concentration (duplicate measurements). Horizontal line: signal from aggregated f-AuNPs (red dotted line in a).

3.5 Assay performance in real samples

3.5.1 Signal processing in complex matrices

To assess performance in complex biological matrices, the assay was applied to 100 clinical serum samples (50 from breast cancer patients and 50 from healthy donors), diluted 1:1 with Milli-Q water. Unlike purified systems, human serum exhibits significant intrinsic absorbance that varies across individuals. To overcome this, extinction spectra were acquired before and after the addition of the f-AuNP reagent. A background subtraction procedure was implemented to isolate the nanoparticle response. Furthermore, spectra were normalized to enable direct comparison across samples.

3.5.2 Diagnostic discrimination between tumoral and non-tumoral samples

Despite the increased optical complexity, a clear distinction between tumoral and non-tumoral samples could be observed, confirming the assay's applicability to real-world clinical specimens. In fact, as shown in Figure 3.7a, the extinction spectra recorded after incubation with pre-aggregated f-AuNPs displayed significant differences between the two groups.

Tumoral samples exhibited a marked drop in absorbance near 600 nm, consistent with nanoparticle disaggregation due to the presence of GREM1-positive exosomes. Non-tumoral samples retained the typical aggregated plasmonic signature, indicating minimal interaction. Spectral data were integrated over the 530–700 nm range and used to construct a receiver operating characteristic (ROC) curve (Figure 3.7b). ROC analysis yielded an area under the curve (AUC) of 0.92 (95% confidence interval: 0.86–0.98), indicating excellent diagnostic performance and robustness of the assay. At the optimal diagnostic threshold, corresponding to an integrated spectral value of 18 (Figure 3.7b), the assay achieved a sensitivity of 84% and a specificity of 90%.

3.5.3 Morphological Validation by Transmission Electron Microscopy

To corroborate the optical data, transmission electron microscopy (Figure 3.7c). Compared to the compact aggregates observed in the absence of the target (Figure 3.2b), the presence of exosomes results in visibly disrupted nanoparticle assemblies.

The micrograph clearly shows exosomes inserted within and physically separating the gold nanoparticle clusters, thereby destabilizing their structure. This direct morphological evidence corroborates the proposed mechanism: aptamer-mediated recognition of exosomal GREM1 sterically hinders nanoparticle aggregation, leading to measurable optical disaggregation.

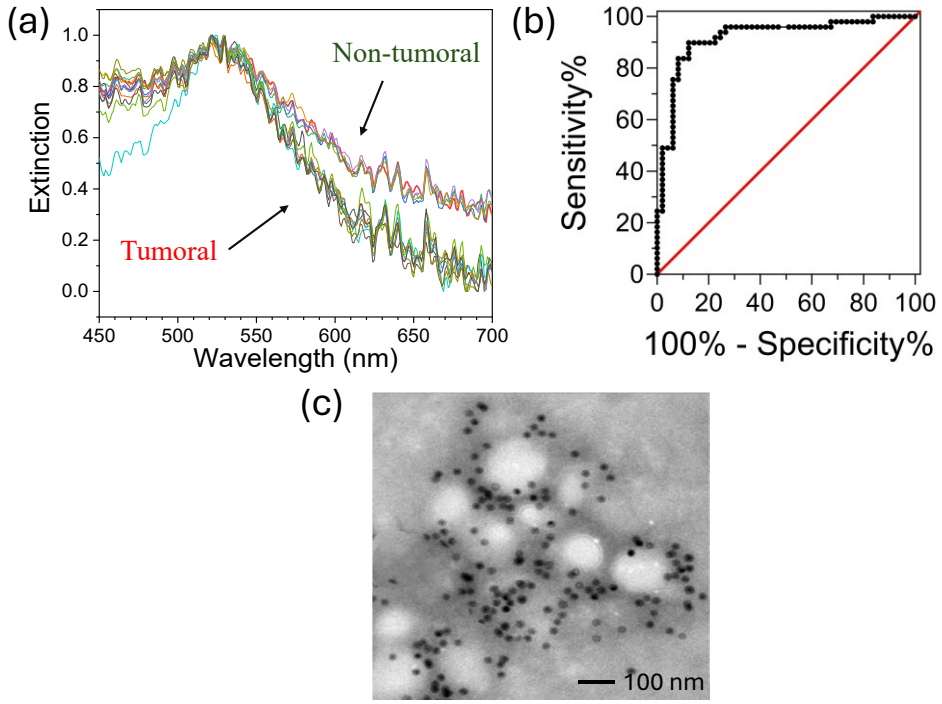

Figure 3.7 Clinical performance and mechanistic validation of the anti-aggregation aptasensor. a) Extinction spectra of serum samples from breast cancer patients (tumoral) and healthy donors (non-tumoral), showing pronounced differences around 600 nm, indicative of nanoparticle disaggregation driven by exosome interaction. b) Receiver Operating Characteristic (ROC) curve based on spectral area analysis. The optimal diagnostic threshold is indicated by the arrow and yields a sensitivity of 84% and a specificity of 90%. c) Transmission electron microscopy (TEM) image of the nanoparticle–exosome system. The comparison with the micrograph reported in Figure 3.2 shows the exosomes that scatter the nanoparticle aggregates, directly supporting the proposed mechanism of target-induced disaggregation.

3.6 Assay specificity

3.6.1 Specificity against non-target cancers

To further explore assay specificity, serum samples from patients affected by non-small cell lung cancer (NSCL) and pancreatic cancer were analysed (Figure 3.8). While samples from pancreatic cancer patients and healthy donors yielded negligible responses, a partial signal was observed in the presence of NSCLC–derived vesicles. This result suggests limited cross-reactivity, potentially due to the expression of shared surface epitopes. This is consistent with literature reports indicating GREM1 expression, in both breast and NSCLC cancers, but not reported prominently expressed in pancreatic-derived EVs [141–143]. Statistical analysis confirmed the selectivity of the assay ($p < 0.05$), supporting the conclusion that disaggregation is driven by a specific interaction between the Ex.50.T-SH aptamer and GREM1-expressing exosomes. The targeted nature of the aptamer-based interaction enables not only the detection of exosomes, but also their molecular profiling—an essential feature for cancer diagnostics.

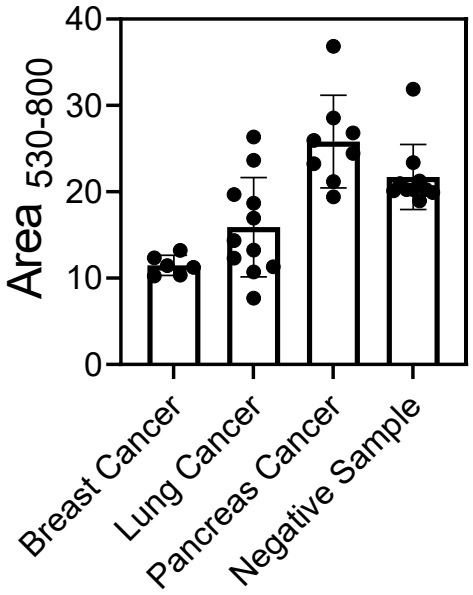

Figure 3.8 Specificity assessment of the aptasensor against non-target cancers. Integrated spectral area (530–800 nm) for serum samples from breast cancer (BC), non-small cell lung cancer (NSCLC), pancreatic cancer (PC), and healthy donors. NSCLC samples show partial cross-reactivity, while PC and healthy samples yield negligible signals, consistent with known GREM1 expression profiles. Each group included 10 independent serum samples.

3.6.2 Benchmarking against conventional detection methods

The performance of our exosome-targeted colorimetric assay was compared to two standard approaches: a commercial GREM1 ELISA (Figure 3.4) and an aptamer-based ELONA (Figure 3.9), using a subset of 36 serum samples (24 breast cancer, 12 controls). The ELISA, which detects total soluble GREM1, failed to distinguish tumoral from non-tumoral samples ($p = 0.2203$). ELONA showed modest but significant separation ($p=0.0133$), yet with limited dynamic range. In contrast, our assay, targeting exosome-associated GREM1, achieved superior discrimination, highlighting the diagnostic advantage of focusing on

vesicle-bound biomarkers rather than total circulating protein in complex biofluids.

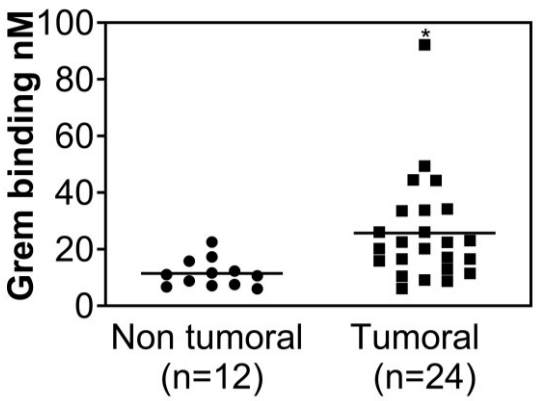

Figure 3.9 Signal from an aptamer-based ELONA assay on the same serum subset (n = 36), showing limited discrimination between BC and non-tumoral groups. Data are presented as mean ± SD of duplicate measurements.

3.6 Discussion and key findings

In this work, we developed and validated a novel colorimetric biosensor based on an anti-aggregation strategy utilizing gold nanoparticles functionalized with the thiolated aptamer Ex.50.T-SH, designed for the detection of (GREM-1)-positive exosomes in human serum. The method is characterized by simplicity, rapidity, and high reproducibility, offering significant advantages over conventional detection platforms such as ELISA and ELONA. The specific interaction between the Ex.50.T-SH aptamer and EVs GREM-1 enabled sensitive detection both in purified environments and in complex biological matrices, including minimally diluted clinical serum samples. The assay operates in a mix-and-measure format, requiring only a single dilution step and no specialized equipment, making it particularly suited for decentralized diagnostics.

A key strength of the developed platform lies in its ability to function effectively in 1:1 (v/v) diluted serum, overcoming the fouling issues that typically hinder the performance of nanoparticle-based biosensors in biological fluids. This represents a significant methodological advancement, as alternative approaches often require dilution factors

as high as 1:1000, compromising analytical sensitivity. Although the biosensor showed low responsiveness to the free GREM-1 protein, it proved highly sensitive to the exosome-bound form, achieving a detection limit of 106 exosomes/mL (isolated EV). More importantly, in real serum samples, the system exhibited robust on-off behavior, allowing for a clear distinction between healthy and breast cancer-derived exosomes. A total of 100 clinical samples were analyzed, yielding excellent diagnostic performance, with a sensitivity of 84% and specificity of 90%, as validated by ROC curve analysis. The system was also shown to selectively respond to exosomes derived from cancers expressing GREM-1 (breast and possibly lung), while showing no significant response to exosomes from pancreatic cancer, thus confirming the assay's biomarker specificity.

Microscopy analyses (TEM) further corroborated the spectroscopic findings, revealing morphological changes in gold nanoparticle aggregates upon exosome binding, thereby supporting the proposed sensing mechanism. Taken together, these findings highlight the potential of this anti-aggregation aptamer-based biosensor for the development of non-invasive, point-of-care diagnostic tools. Its performance, ease of use, and ability to discriminate among exosomal populations based on biomarker expression open new perspectives for liquid biopsy applications in precision oncology. Future efforts will aim to integrate this sensing platform into microfluidic systems to enable high-throughput analysis, as well as to expand its diagnostic scope through the inclusion of additional aptamers targeting alternative exosomal biomarkers.

Chapter 4 — Development of a Colorimetric ssDNA Biosensor for the Detection of *Fusarium oxysporum* Environmental DNA

4.1 The agricultural need for field-deployable detection of *Fusarium oxysporum* in soil

Environmental DNA (eDNA) has rapidly become a cornerstone in ecological monitoring, enabling the detection of organisms through trace nucleic acids shed into the environment (e.g., water, soil, air) [144]. Its non-invasive nature and capacity to reveal low-abundance taxa make it a powerful tool for biodiversity assessment, invasive species surveillance, and pathogen tracking [145]. However, the utility of eDNA approaches hinges on the performance of the molecular assays employed. Ideal eDNA detection methods must combine high sensitivity and specificity with speed, simplicity, robustness against inhibitors in environmental matrices, and feasibility for field or high-throughput deployment [146].

Typically, rapid and accurate detection in complex samples depends on nucleic acid amplification methods like Polymerase Chain Reaction (PCR). While PCR is highly effective, it can be time-consuming, expensive, and requires specialized equipment; its reliance on precise temperature control further limits its applicability in on-site settings [147]. Alternative methods such as Loop-mediated Isothermal Amplification (LAMP) offer faster and less intensive equipment solutions but still involve multiple preparation steps and are not exempt from technical complications [148].

A major challenge across many platforms is the long hybridization times required for hybridization-based detection methods. Thus, despite advances in PCR and metabarcoding, many published assays fall short in one or more of the characteristics required for large-scale measurements, highlighting the need for alternative formats that better reconcile operational ease and analytical rigor.

Colorimetric and optical sensors are emerging as the most widely used class of biosensors, as they offer several advantages over conventional analytical techniques, enabling real-time, rapid, cost-effective, and label-free detection of a wide range of analytes [149–151]. In this context, gold nanoparticles (AuNPs) have been extensively employed as a sensing element for colorimetric detection owing to their unique optical properties and the straightforward functionalization of their surfaces.

To address the limitations of current detection strategies in environmental monitoring, we applied this biosensing approach to the detection of *Fusarium oxysporum*, a soil-borne ascomycete fungus responsible for fusarium wilt, a lethal vascular disease affecting numerous crops worldwide [152].

The species includes over 100 host-specific forms, known as formae speciales (ff. spp), which are widely distributed [153]. It infects a range of economically important plants, including Solanaceae crops such as tomatoes, potatoes, peppers, and eggplants, as well as oil palm, legumes, strawberries, sugarcane, lettuce, watermelon, and bananas.

The fungus reproduces asexually through spores that can remain viable in soil for up to 30 years, making management difficult [154]. Infection occurs when hyphae penetrate the epidermal cells of both wounded and intact roots. Dispersal of *F. oxysporum* occurs via contaminated seeds, planting material, farm equipment, and through air and water movement [155].

While the species affects many plants, each forma specialis typically targets specific hosts. Its global distribution and persistence make it one of the most challenging threats to agricultural systems [116,117].

Under favorable conditions, *Fusarium* infections cause severe yield losses, with major repercussions for the agro-food sector. Current management relies heavily on preventive measures—ranging from chemical pesticides, which risk environmental and food safety issues [156,157], to biological agents like *Trichoderma harzianum* [158]. However, the lack of reliable tools to quantify *Fusarium* populations in soil often leads to excessive or untargeted applications of these treatments, increasing costs and ecological impact [159]. Overall, the presence of this pathogen entails additional management costs, ultimately affecting the final price of agro-food products.

In this work, we address this gap by testing a novel biosensor for the detection of *Fusarium oxysporum*, a model phytopathogen whose accurate monitoring in soil could significantly improve the precision and sustainability of disease management strategies.

4.2 Complementary-Probe anti aggregation assay

Once functionalized with HS-ssDNA (Chapter 2 section 2.7.2), f-AuNPs can be used for colorimetric detection through target-induced

nanoparticle aggregation, which typically occurs via two mechanisms classified as either cross-linking (CL) [160] or non-cross-linking (NCL) [161]. The CL DNA detection method employs two sets of AuNPs functionalized with ssDNA probes that recognize the two ends of the ssDNA target. If the ssDNA target is recognized this results in particle aggregation and a visible color shift from red to blue [160]. In the NCL method, a single batch of AuNPs bearing ssDNA probes hybridizes with the target, converting flexible, highly charged ssDNA into more rigid dsDNA with lower charge density. This reduces electrostatic and steric stabilization, so in the presence of salt the AuNPs lose colloidal stability and aggregate without forming interparticle cross-links. The NCL method is generally faster and less temperature-dependent than the CL approach [162,163], but the latter typically offers higher specificity and sensitivity [164]. NCL performance, however, is strongly influenced by ionic strength, as aggregation occurs only under optimized salt conditions [165]. Both methods are highly sequence-length dependent: the CL assay fails when the target is truncated or embedded in longer fragments, while the NCL assay is particularly sensitive to terminal mismatches or length variations. These features limit their applicability to real samples, where DNA fragments often display heterogeneous lengths. Consequently, there is a clear need for a more robust and adaptable detection strategy.

To overcome these limitations, we developed a novel two-step, label-free colorimetric biosensor based on an anti-aggregation mechanism, in which the presence of the ssDNA target inhibits nanoparticle aggregation (Complementary-Probe Anti-Aggregation Assay, CPAA).

The assay uses two batches of AuNPs functionalized with ssDNA Probe and its complementary (C_Probe). As illustrated in Figure 4.1, the target first hybridizes with Probe–AuNPs (first step), after which C_Probe–AuNPs are introduced (second step). When the target is present, its binding to Probe prevents Probe /C_probe hybridization, maintaining the red color of the colloid; in its absence, Probe and C_Probe hybridize, causing aggregation and a visible color shift. Each hybridization step is freeze-mediated [166,167], enabling rapid detection and completion of the entire assay within 5 minutes.

The biosensor operates through a two-step, label-free colorimetric mechanism based on the anti-aggregation of gold nanoparticles

(AuNPs), with hybridization promoted by freezing. This approach allows rapid detection of the target DNA sequence (5′ CGCACTCATTGAGGTTTTGA 3′) within 5 minutes. Two batches of AuNPs are employed: one functionalized with *F. oxysporum* Probe and the other with *F. oxysporum* C_Probe. The overall detection principle depicted in Figure 4.1 is realized by the following procedure.

1) Mix 10 µL of *F. oxysporum* Probe-AuNPs (OD 4) with 40 µL of target sequence suspension at concentrations in a range of 0–200 nM.
2) Incubate for 1 minute at −80°C on dry ice.
3) Thaw at room temperature and add 10 µL of *F. oxysporum* C_Probe-AuNPs (OD 4).
4) Incubate for 1 minute at −80 °C on dry ice.
5) Acquire the extinction spectra.

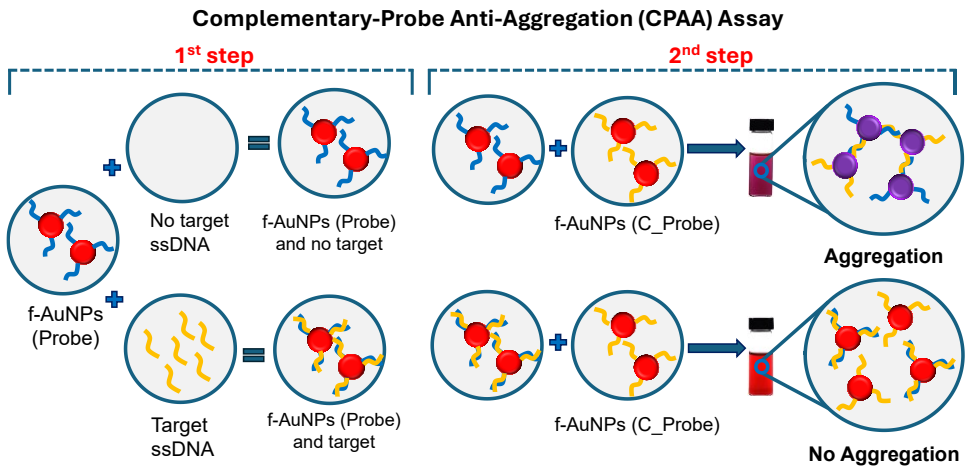

Figure 4.1 Schematic representation of the colorimetric assay: In the presence of the target, hybridization with Probe–AuNPs prevents aggregation upon addition of C_Probe–AuNPs. In the absence of the target, Probe–AuNPs and C_Probe–AuNPs hybridize with each other, leading to nanoparticles aggregation and a visible color change.

4.3. Dose–response curve and Limit of Detection (LOD) Determination

4.3.1 Dose-response curve in ultra-pure water

To identify the optimal biosensing parameter, the full extinction spectrum was measured for several target sequence concentrations. Spectra were normalized to their maximum optical density (OD), and the 550–800 nm range—where spectral changes are most pronounced—was selected, as it provides the clearest information on ssDNA presence and nanoparticle aggregation (Figure 4.2a-b). In this system, absence of the ssDNA target results in maximal aggregation, like the control (no ssDNA), whereas increasing target concentration progressively reduces aggregation (Figure 4.3a). TEM analysis confirmed this trend: large aggregates form in the absence of the target (Figure 4.3b), while they are absent at high concentrations (200 nM; Figure 4.3c).

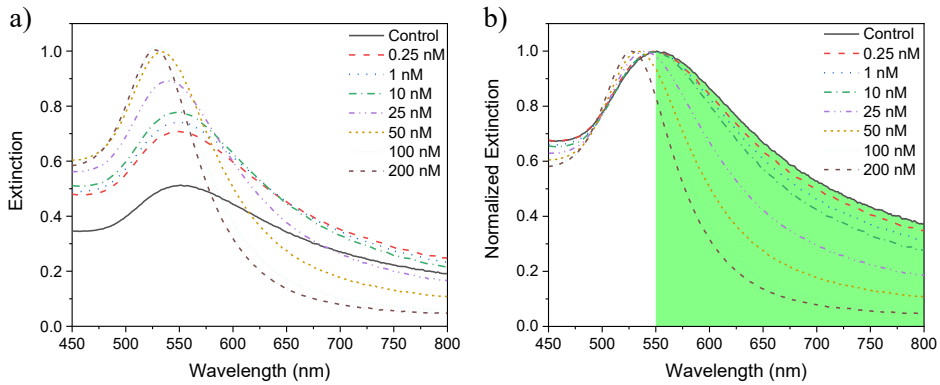

Figure 4.2. Extinction spectra and sensing parameter. a) Extinction spectra at several concentrations. b) Normalized extinction spectra highlighting the 550–800 nm range.

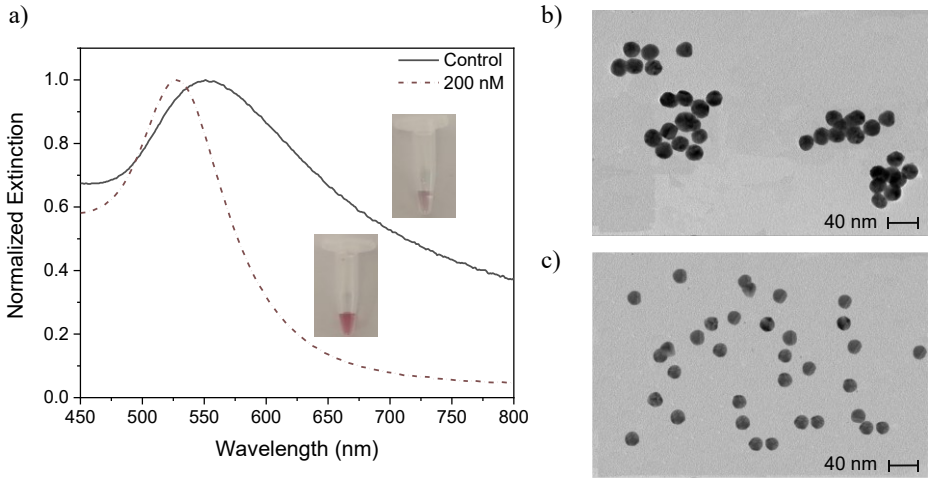

Figure 4.3. a) Normalized extinction spectra for some of the condition tested. Control extinction spectrum (no target ssDNA) which shows maximum AuNPs aggregation compared to the extinction spectrum for 200 nM target ssDNA (maximum concertation tested), showing the minimal aggregation. b) TEM image of control solution, confirming extensive nanoparticles aggregation. c) TEM image of 200 nM of ssDNA target detection, confirming reduced aggregation at high target concentration.

To obtain a robust sensing parameter, we introduced the integrated absorbance difference, $\Delta A_{550\text{-}800} = A_{\text{control}} - A_{\text{sample}}$. Plotting $\Delta A_{550\text{-}800}$ as a function of the ssDNA target concentration yielded the dose–response curve in ultrapure water (Figure 4.4). The measurements were performed in triplicate and fitted using a three-parameter Hill equation:

$$y = \frac{V_{\text{max}} \cdot x^n}{{K_m}^n + x^n} \qquad (7)$$

In Eq. (7) V_{max} is the saturation value, and K_m is the analyte concentration at which half of this saturation value is reached, and *n* is the Hill coefficient. Applying the 3σ criterion (shaded area in Figure 4.4), we achieved a LOD of 2 nM (12 pg/µL). Here the LOD was calculated by adding three times the standard deviation of the signal obtained from

multiple measurements of the zero-concentration sample (i.e., in the absence of the target) to its mean value [168,169]. Various f-AuNPs having different A_{610}/A_{525} ratios were tested, revealing optimal performance for f-AuNPs with a A_{610}/A_{525} ratio of 0.24 (Figure 4.5).

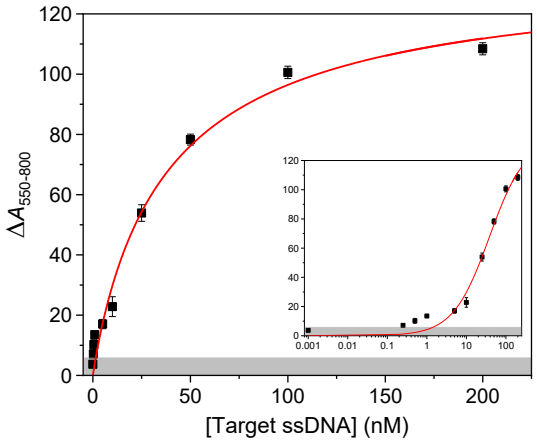

Figure 4.4. Dose-response curve obtained detecting the target ssDNA sequence in ultrapure water. The inset displays the same curve on a semi-logarithmic scale. The error bars in the figure represent the results of triplicate experiments.

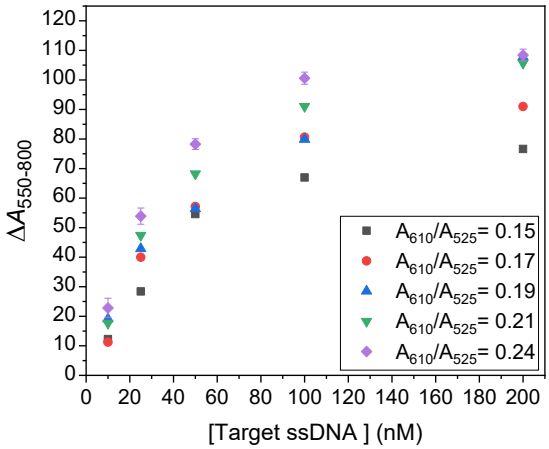

Figure 4.5 Detection performed using f-AuNPs with different A_{610}/A_{525} ratios. The results show that nanoparticles with an A_{610}/A_{525} ratio of 0.24 (After washing) yield the strongest signal, indicating that higher ssDNA surface density can obstruct target sequence detection.

4.4 Specificity assessment

4.4.1 Specificity against non-target sequence in complex mixture

To evaluate the specificity of the developed biosensor, we assessed its response against various ssDNA sequences (Table 2, entries 3–9). Initially, we tested each non-target sequence individually as well as the target sequence under identical experimental conditions; all sequences were tested at 200 nM (the highest concentration tested in dose-response curve). In Figure 4.6a, it is showed how the non-target sequences elicit only negligible responses, while the target sequence generates a significant signal.

Next, to determine whether the biosensor could detect the target sequence in the presence of other ssDNA sequences, we first prepared a mixture of non-target sequences, each at 200 nM. Testing this mixture alone produced no significant signal. We then added the target ssDNA at two different concentrations, 10 nM and 200 nM, and observed that the resulting signals closely matched those obtained from the target sequence alone (Figure 4.6b). These results demonstrate that the biosensor effectively detects its target even in a complex mixture.

Overall, these results confirm that the DNA biosensor displays excellent specificity, reliably distinguishing fully complementary targets from non-complementary sequences.

Table 2

List of ssDNA sequences used in AuNPs-based colorimetric biosensor.

	ssDNA sequences	**Sequence 5' to 3'**
1	*F. oxysporum* Probe	Thiol-C6- AAAAACCCCC TCA AAA CCT CAA TGA GTG CG
2	*F. oxysporum* C_Probe	Thiol-C6- AAAAACCCCC CGC ACT CAT TGA GGT TTT GA
3	*F. oxysporum* target (TS)	CGC ACT CAT TGA GGT TTT GA
4	Non-target sequence 1 (NTS1)	GTG CGA TGG TTG GTA GTA GT
5	Non-target sequence 2 (NTS2)	ACT ACT ACC AAC CAT CGC AC
6	Non-target sequence 3 (NTS3)	GCT GGT CAA GGT TTC TCT GC
7	Non-target sequence 4 (NTS4)	ACT GAA AGA GAG GGA AAT GGA GGG ACG GTC

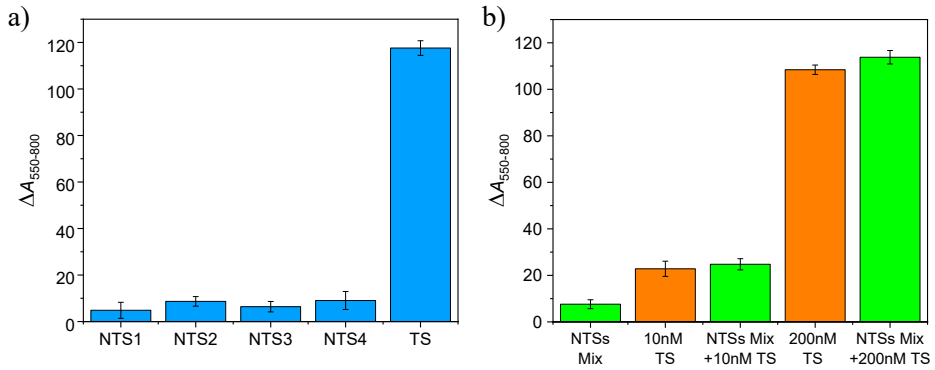

Figure 4.6 Specificity of the developed DNA biosensor. a) Response of the biosensor to individual ssDNA sequences: the target sequence (200 nM) produces a strong signal, whereas non-target sequences (200 nM) show only negligible responses.b) Response of the biosensor to the target sequence in the presence of a mixture of non-target ssDNA (each at 200 nM): the mixture alone yields no signal, but upon adding the target sequence at concentrations of 10 nM and 200 nM (green bars), the signal intensity closely matches that of the target tested alone (orange bars). All error bars in the figures represent the results of duplicate experiments.

4.4.2 Supporting evidence from preliminary studies

Additional confidence in the biosensor's design was drawn from earlier preliminary experiments (not part of this specific validation campaign). In these studies, AuNPs were functionalized with different probes and tested against the ssDNA sequences listed in the Table 3. These studies demonstrated that the system could detect the target even when it is embedded within a longer sequence (30 bp), and that a longer non-target sequence (50 bp) does not affect the biosensor's specificity (Figure 4.7a-b). Additionally, we evaluated the stability of these functionalized AuNPs: they remained fully functional for 15 days, after which a gradual 10 % loss of activity was observed between days 16 and 140 (Figure 4.8).

Table 3. List of probes and ssDNA sequences for preliminary specificity and stability assays.

	ssDNA sequences	bp	Sequence 5' to 3'
1	Probe	30	Thiol-C6- AAAAACCCCC TCC CTC CAT TTC CCT CTC TT
2	C_Probe	30	Thiol-C6- AAAAACCCCC AAG AGA GGG AAA TGG AGG GA
3	Non-target sequence 1 (NTS1)	20	GTG CGA TGG TTG GTA GTA GT
4	Non-target sequence 2 (NTS2)	20	ACT ACT ACC AAC CAT CGC AC
5	Non-target sequence 3 (NTS3)	20	GCT GGT CAA GGT TTC TCT GC
6	Non-target sequence 4(LNTS)	50	CCT ACG TAG CTA GCA TAC GGT ACT AGC TAT ACG CAA TGC TAC GTA CGC AT
7	Target sequence (TS)	20	AAG AGA GGG AAA TGG AGG GA
8	Long Target sequence (LTS)	30	**ACT GA**A AGA GAG GGA AAT GGA GGG A**CG GTC**
9	Target sequence 1m.m (TSM)	20	AAG AGA GGG TAA TGG AGG GA

In the table, bold indicates bases added to the target sequence, while underlining denotes mismatches.

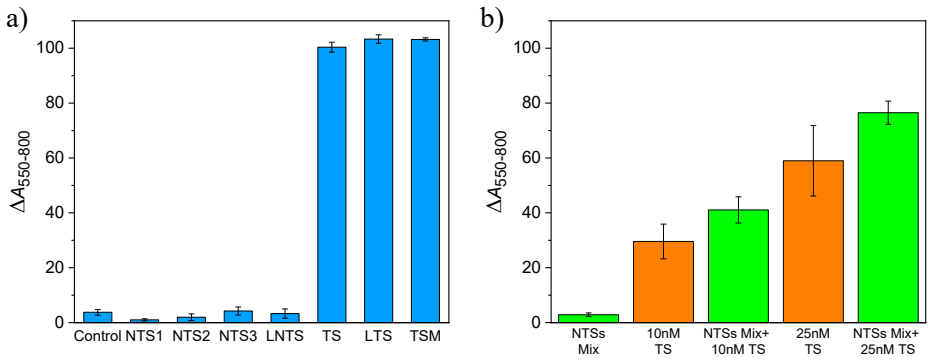

Figure 4.7 Specificity test conducted using AuNPs functionalized with probe sequences listed in Table 3 (a) Specificity tested against sequences in the Table 3 (lines 3-9), each sequence was tested at a concentration of 200nM. The results shown how the system is specific, and it is capable of detect target sequence also if it is included in a longer sequence. Non target sequences did not give any significant value. (b) Specificity test conducting mixing the all the non-target sequences (200nM each) the target sequence was added at varying concentrations (10nM and 25 nM). The results (green bars) closely match those obtained with the target sequence alone (orange bars), indicating that the biosensor detects the target effectively even in the presence of multiple non-target sequences. All error bars in the figures represent the results of duplicate experiments.

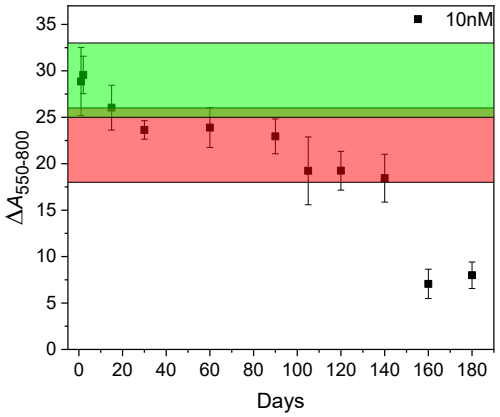

Figure 4.8 AuNP batches functionalized with the probe sequences listed in Table 3 were evaluated for stability.
The f-AuNPs were stored in the dark at 4°C, and their sensing response was monitored over time using a 10 nM target sequence. As shown, the f-AuNPs retained 100% activity for up to 15 days. From day 16 to day 120, functionality declined by approximately 10%, demonstrating robust long-term stability under these storage conditions**.** All error bars in the figures represent the results of duplicate experiments.

4.5 Real sample test

4.5.1 Sample preparation and DNA extraction

Soil samples were obtained from a controlled-environment experiment designed to test the mycorrhization of *Quercus pubescens* with *Tuber aestivum*. Prior to use, the absence of *F. oxysporum* in the soil was confirmed through a metagenomic analysis aimed at characterizing the fungal community (mycobiota), using ITS1 and ITS2 regions as primers. The bulk soil was subsequently divided into two aliquots. One aliquot was left untreated and served as a control, free of *F. oxysporum*. The second aliquot was inoculated with *F. oxysporum* suspension. The inoculum was prepared by scrapping the surface of a 60 mm diameter petri dish to remove *F. oxysporum* mycelium. The collected sample, corresponding to around 0.5 g of fresh mycelium, was then diluted in 5 mL of sterile water and mixed by stirring for 3 minutes until the suspension appeared homogenized by visual inspection. The *F. oxysporum* suspension was subsequently added to the prepared 50 g soil sample. The soil was thoroughly mixed by stirring for 1 minute and was then used for total DNA extraction.

Prior to extraction, a subsample of 2 g of soil was diluted in 20 mL of PBS (phosphate-buffered saline) to promote osmotic imbalance and facilitate the breakdown of mycelial membranes. The solution was concentrated by centrifugation at 12000 g for 2 minutes; the supernatant was discarded, and the pellet was used for DNA extraction. Total DNA from each soil sample was extracted through multiple independent extractions using the DNeasy PowerSoil Kit (Qiagen, Hilden, Germany), and the final volume was adjusted to 100 µL in the buffer C6 (10 mM Tris-HCl, pH 8.5), the elution buffer supplied with the kit.

4.5.2 DNA Fragment size control and quality verification

To ensure efficient hybridization in the colorimetric assay, genomic DNA extracted from real samples was fragmented to an optimal size range (200–500 bp). For routine use, a widely accessible bath-type sonicator (Elmasonic S 40 H, 37 kHz) was employed, and fragmentation efficiency was evaluated at increasing sonication times: 30, 60, 90, 120, and 150 minutes (labeled S-30 to S-150).

Additionally, a high-power focused-ultrasonicator (Bioruptor Plus, Diagenode) was used only for comparative purposes to investigate whether fragmentation time could be significantly reduced with more

intense energy input. Under standard ChIP conditions (10 minutes, 30 s ON/30 s OFF, high power), this system produced DNA fragments in the 200–500 bp range — demonstrating that high-power sonication can achieve in 10 minutes what requires hours with a conventional bath sonicator. However, for all biosensor validation experiments, only the Elmasonic system was used, ensuring compatibility with standard laboratory settings.

For electrophoretic analysis, 10 µL of each sonicated DNA sample was mixed with 2 µL of 6×DNA loading dye (1:5 v/v). A 1% (w/v) agarose gel was prepared in 1×TAE buffer using Ultrapure agarose (Thermo Scientific) and stained with GelRed (1:10,000). Each sample (12 µL) was loaded alongside a GeneRuler 50 bp DNA Ladder (Thermo Scientific, SM0371). Electrophoresis was performed at 100 V for 45–60 min in 1×TAE running buffer, and DNA fragments were visualized under UV light using a ChemiDoc Imaging System (Bio-Rad).

As shown in Figure 4.7 non-sonicated DNA (NS) appeared as a high-molecular-weight smear (>10 kb). With the Elmasonic system, effective fragmentation into the 200–500 bp range was achieved after 120 minutes (S-120), with no further size reduction at 150 minutes. In contrast, the Bioruptor Plus yielded a comparable fragment profile in just 10 minutes, confirming that sonication time is highly dependent on ultrasonic power.

These results validate the use of 120-minute sonication with the Elmasonic bath as a robust, accessible protocol for preparing DNA samples compatible with the biosensor's hybridization requirements.

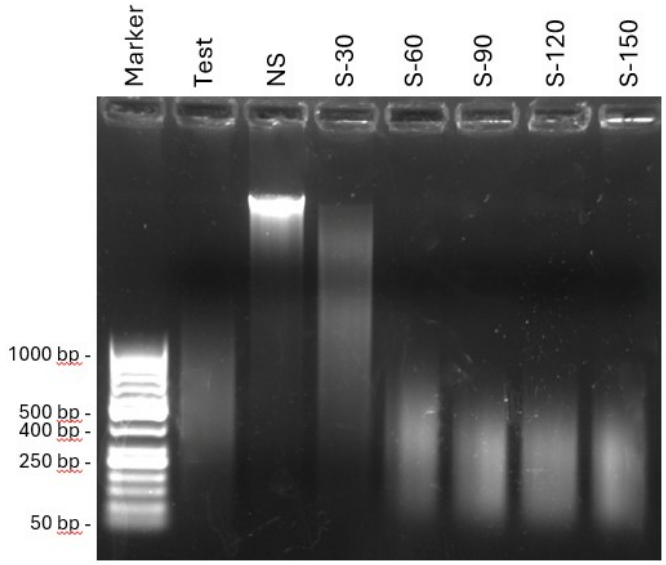

Figure 4.9 Fragmentation sizing through agarose gel electrophoresis. Agarose gel is 1% Ultrapure agarose (Thermo Scientific) in Tris-acetate-EDTA solution (TAE 1X). Marker: GeneRuler 50bp DNA (Thermo Scientific) indicating bp sizing; Test: DNA sonicated for 10 minutes under ChIP standard condition using Bioruptor plus Sonicator; NS: Non sonicated DNA; S-30, S-60, S-90, S-120 and S-150: DNA sonicated at 30, 60, 90, 120 and 150 minutes in Elmasonic Sonicator (S 40 (H), 37 kHz).The result demonstrate effective DNA fragmentation and indicate that, when using a high-power sonicator, the required fragmentation time can be significantly reduced.

4.5.4 Recovery in real matrices

After evaluating the biosensor's specificity, we tested its performance using DNA extracted from soil samples, referred to here as real samples. Unlike the samples previously prepared in water, the real samples were sonicated for 2 hours in an ultrasonic bath (Elmasonic S 40 (H), 37 kHz). Sonication was used to fragment the DNA, producing shorter ssDNA strands and thus improving detection specificity. The effectiveness of the sonication process was verified by gel electrophoresis (Figure 4.9).

Two identical soil samples were prepared as described in Section 4.5.1. After confirming the absence of *F. oxysporum* DNA in both samples, one was inoculated with *F. oxysporum*, while the other served as a control. Fresh *F. oxysporum* mycelium was introduced into the soil to achieve a concentration consistent with levels typically used in laboratory studies [159,170]. Following DNA purification, spectrophotometer measurements showed total DNA concentrations of 22 ng/µL and 15 ng/µL for the non-contaminated and contaminated soils, respectively. This indicates that the presence of *F. oxysporum* DNA did not significantly alter the total DNA content in the soil. Undiluted and serially diluted extracts (1:2, 1:10, 1:50, 1:100) from both samples were then tested using AuNPs functionalized with *F. oxysporum* probes, and the results are presented in Figure 4.10.

In the extract from the non-contaminated soil (control) (Figure 4.10), no detectable signal was observed across all dilutions, except at the highest concentrations (undiluted and 1:2). In contrast, the extract from the contaminated soil produced strong signals. The elevated signals at low dilutions obtained in both samples were not due to a lack of specificity — both the biosensing system and probes had already been validated — but rather resulted from interference caused by the extraction buffer. We identified the C6 buffer used in the final step of DNA extraction, as the potential source of this interference. To verify this hypothesis, we tested the AuNPs functionalized with *Fusarium* probes against the buffer itself, and the data confirmed that the increased signals observed at the undiluted and 1:2 dilutions were indeed caused by the high buffer concentration. To account for this interference in quantitative analysis, data were fitted using the same Hill equation applied to the reference dose–response curve. However, because the C6 buffer interferes at lower dilutions (undiluted and 1:2), these points do not reflect true system saturation. To avoid biasing the fit with these distorted low-dilution values, $V_{\max}$ was fixed to the value obtained from the interference-free dose–response curve, while the remaining Hill parameters were estimated from the data. This approach yields a robust and biologically meaningful fit, free from artefactual inflation or suppression of the plateau.

Under this constraint, the non-contaminated sample exhibits a response indistinguishable from that of the buffer C6: both experimental points and the fitted curve lie within the background noise region,

confirming the absence of a specific analyte signal. These results conclusively demonstrate that the control sample contains no detectable *F. oxysporum* DNA, as its response is fully consistent with baseline interference. In contrast, the contaminated sample exhibited a clear, concentration-dependent response that rose well above background interference even at high dilutions, although signals at the lowest dilutions (undiluted and 1:2) remained affected by residual buffer interference. To ensure accurate detection and minimize this effect, we recommend the dilution of the samples. Consistently, we consider as the optimal detectable signal that obtained at the 1:10 dilution. According to the dose–response curve (Figure 4.4) and considering the dilution factor, the estimated *F. oxysporum* DNA concentration of the sample was approximately 50 nM. By considering a mean value of 250 bp for the fragment distribution (Figure 4.9), this corresponds to approximately 4 ng/µL, a value consistent with a contamination level too low to significantly impact the total soil DNA content. Notably, a detectable signal was still obtained at the 1:100 dilution, indicating that the initial *F. oxysporum* concentration used to contaminate the soil could be reduced by at least one order of magnitude without compromising detection performance.

For practical, real-world applications, the biosensing platform could be further optimized by reducing the required initial *F. oxysporum* concentration. This can be achieved by extracting DNA from larger soil samples, increasing the total amount of target DNA available. Additional improvements could be obtained by concentrating the extracted DNA or by removing residual extraction buffer through an extra washing step. Implementing these strategies would lower the minimum amount of *F. oxysporum* needed for reliable detection—potentially by one or more orders of magnitude— making the assay more applicable to field conditions.

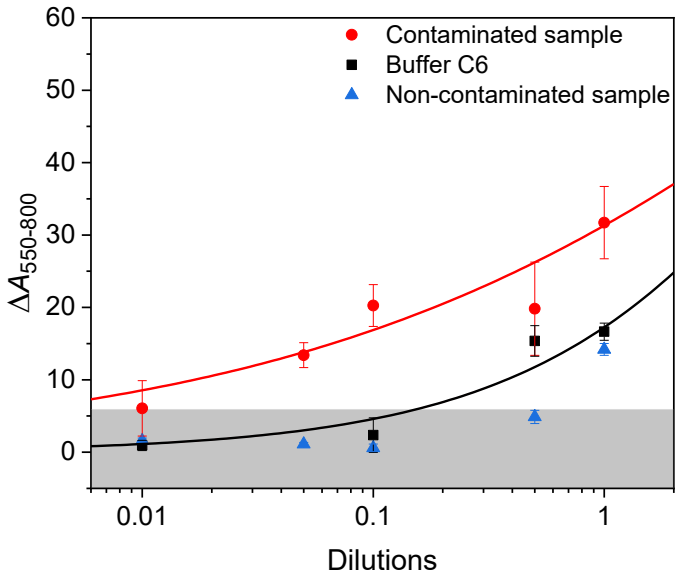

Figure 4.10 Signal response across serial dilutions for contaminated soil (red circles), C6 buffer alone (black squares). and non-contaminated soil (blue triangles). Both soil samples exhibited elevated signals at the highest concentrations (undiluted and 1:2), but only the contaminated sample showed a clear dose-dependent response at higher dilutions (1:10–1:100), where buffer interference is negligible. The non-contaminated sample displayed no specific signal beyond the background level, with its undiluted and 1:2 responses matching those of the buffer control, confirming that the elevated signals at low dilutions can be ascribed to buffer-induced interference. To account for this effect in quantitative analysis, all data were fitted using a Hill equation with $V_{\max} = 135$, which is the value obtained from the interference-free calibration curve. The resulting fits confirm that the non-contaminated sample's response is indistinguishable from background noise, whereas the contaminated sample yields a robust analyte-specific signal. Error bars represent duplicate measurements.

4.6 Final considerations

Rapid and accurate detection of *Fusarium oxysporum* in soil is crucial for effective crop protection, as its presence strongly influences agricultural management strategies. The use of chemical pesticides, for instance, poses risks such as food safety concerns (chemical residues), loss of biodiversity in adjacent natural ecosystems, and reduction of beneficial microbial communities in agricultural soils [171]. Less impactful strategies rely on biological control agents, including mycoparasitic fungi of the genus *Trichoderma* (e.g., *T. harzianum*), which are widely applied against Fusarium wilt [156]. In all cases, the presence of the pathogen entails additional management costs that ultimately affect the price of agro-food products. Yet, the lack of tools capable of accurately quantifying *Fusarium* populations in soils hampers targeted interventions and often leads to the excessive use of both chemical and biological control agents [158].

In this work, we developed a rapid, label-free colorimetric biosensor that integrates freeze–thaw-mediated hybridization with AuNP anti-aggregation for the detection of *F. oxysporum* ssDNA. By tuning nanoparticle size, probe density and freezing conditions, the assay achieved a 2 nM detection limit and required only 5 minutes to complete. The biosensor strongly discriminated against non-complementary sequences while tolerating a single central mismatch without affecting the colorimetric output. Rather than reducing selectivity, this controlled mismatch tolerance improves practical sensitivity when analysing fragmented or partially degraded DNA, which is the typical form found in real environmental matrices.

When tested on DNA extracted from soil, the sensor maintained both sensitivity and selectivity despite the presence of matrix inhibitors, confirming its robustness for real-sample applications. The minimal reaction volume (40 µL) and visual readout make the assay particularly suitable for on-site diagnostics, especially in resource-limited settings.

Overall, the proposed platform represents a reliable, affordable and amplification-free alternative to conventional molecular assays. Its modular architecture allows rapid adaptation to other DNA targets by simply changing probe sequences. Future integration with automated handling systems and AI-assisted spectral analysis may further enhance throughput, reduce user variability, and support real-time decision-making in agricultural, clinical and environmental monitoring.

5. — Conclusions

This thesis addresses two urgent diagnostic challenges, one in oncology and one in agricultural sustainability—through the development of two innovative colorimetric biosensors based on a shared gold nanoparticle (AuNP) platform. In an era where rapid, instrument-free, and field-deployable molecular diagnostics are increasingly needed, this work demonstrates how a single plasmonic transducer can be adaptively functionalized with distinct nucleic acid architectures to serve divergent yet equally critical applications: early cancer detection via liquid biopsy and on-site surveillance of a devastating soil-borne pathogen.

The first major contribution is an aptamer-based biosensor for breast cancer-derived exosomes, which operates through a target-induced disaggregation mechanism. AuNPs are first functionalized with a thiolated RNA aptamer (Ex.50.T) and deliberately aggregated using controlled salt addition, yielding a stable, blue-shifted colloidal state. Upon exposure to exosomes bearing the target protein GREM1, the aptamer undergoes a conformational switch that disrupts interparticle interactions, leading to nanoparticle disaggregation and a visible blue-to-red color transition. This strategy enables direct detection in diluted serum without purification, offering a rapid alternative to conventional exosome analysis methods.

The second contribution is a DNA-based biosensor for *Fusarium oxysporum* genomic DNA, which employs a two-step, competition-based anti-aggregation approach. Two separate AuNP populations are functionalized with a target-specific probe (Probe) and its fully complementary sequence (C_Probe). In the absence of the target DNA, Probe and C_Probe hybridize upon mixing, cross-linking the nanoparticles and inducing aggregation (red-to-blue shift). However, when the target is present, it preferentially binds to Probe–AuNPs during the first detection step, sequestering the probe and preventing hybridization with C_Probe. This inhibits aggregation, and the solution remains red. Critically, both hybridization steps are accelerated by freeze-mediated kinetics, enabling the entire assay to be completed in just 5 minutes—without labels, amplification, or instrumentation.

Together, these systems exemplify the adaptability of AuNP-based LSPR biosensing: one leverages target-triggered disaggregation, while the other exploits target-mediated inhibition of aggregation—two distinct optical strategies built on the same nanoplatform. This duality

underscores a central theme of this work: that rational nucleic acid engineering can reconfigure a simple plasmonic system for diverse diagnostic scenarios, from clinical liquid biopsy to environmental pathogen screening.

Future improvements and extensions of this platform include its straightforward adaptation to detect other cancer biomarkers by simply replacing the RNA aptamer, demonstrating the modularity of the disaggregation-based biosensor for different tumor targets. Similarly, the DNA-based anti-aggregation biosensor will be validated under real-field conditions for *Fusarium oxysporum* detection and can be readily reconfigured to identify other microorganisms by exchanging the DNA probe sequence.

In both cases, signal readout can be enhanced through smartphone-based imaging coupled with artificial intelligence (AI)-assisted analysis, enabling rapid, objective, and semi-quantitative interpretation directly at the point of need. This paves the way toward a truly versatile, field-deployable, and nucleic acid-programmable diagnostic system for diverse clinical and environmental applications

In conclusion, this thesis delivers two rapid, low-cost, and instrument-free biosensors that bridge the gap between laboratory performance and field applicability. By harnessing two complementary modulation strategies of LSPR, disaggregation and competitive anti-aggregation, this work advances the vision of a versatile, nucleic acid-programmable diagnostic platform for challenges spanning human health and environmental monitoring.

References

[1] H. Aldewachi, T. Chalati, M.N. Woodroofe, N. Bricklebank, B. Sharrack, P. Gardiner, Gold nanoparticle-based colorimetric biosensors, Nanoscale 10 (2018) 18–33. https://doi.org/10.1039/c7nr06367a.

[2] W. Wei, K. Chen, G. Ge, Strongly coupled nanorod vertical arrays for plasmonic sensing, Advanced Materials 25 (2013) 3863–3868. https://doi.org/10.1002/adma.201301181.

[3] S. Link, M.A. El-Sayed, Size and temperature dependence of the plasmon absorption of colloidal gold nanoparticles, Journal of Physical Chemistry B 103 (1999) 4212–4217. https://doi.org/10.1021/jp984796o.

[4] Y. Wang, J. Zhou, J. Li, Construction of Plasmonic Nano-Biosensor-Based Devices for Point-of-Care Testing, Small Methods 1 (2017). https://doi.org/10.1002/smtd.201700197.

[5] M. Zhou, Z. Geng, Integrated LSPR Biosensing Signal Processing Strategy and Visualization Implementation, Micromachines (Basel). 15 (2024). https://doi.org/10.3390/mi15050631.

[6] A. Uniyal, G. Srivastava, A. Pal, S. Taya, A. Muduli, Recent Advances in Optical Biosensors for Sensing Applications: a Review, Plasmonics 18 (2023) 735–750. https://doi.org/10.1007/s11468-023-01803-2.

[7] P.R. Boro, P.P. Borthakur, E. Baruah, Advancements in Optical Biosensor Technology for Food Safety and Quality Assurance, in: MDPI AG, 2025: p. 6. https://doi.org/10.3390/engproc2025106006.

[8] M.A. Morales, J.M. Halpern, Guide to Selecting a Biorecognition Element for Biosensors, Bioconjug. Chem. 29 (2018) 3231–3239. https://doi.org/10.1021/acs.bioconjchem.8b00592.

[9] F. Shalileh, H. Sabahi, M. Golbashy, M. Dadmehr, M. Hosseini, Recent developments in DNA nanostructure-based biosensors for the detection of melamine adulteration in milk, Microchemical Journal 195 (2023). https://doi.org/10.1016/j.microc.2023.109316.

[10] I. Palchetti, M. Mascini, Nucleic acid biosensors for environmental pollution monitoring, Analyst 133 (2008) 846–854. https://doi.org/10.1039/b802920m.

[11] O.B. Daramola, R.K. Omole, B.A. Akinsanola, Emerging applications of biorecognition elements-based optical biosensors for food safety monitoring, Discover Sensors 1 (2025). https://doi.org/10.1007/s44397-025-00003-3.

[12] Y. Du, S. Dong, Nucleic acid biosensors: Recent advances and perspectives, Anal. Chem. 89 (2017) 189–215. https://doi.org/10.1021/acs.analchem.6b04190.

[13] C. Tuerk, L. Gold, Systematic Evolution of Ligands by Exponential Enrichment: RNA Ligands to Bacteriophage T4 DNA Polymerase, n.d. https://www.science.org.

[14] A. Mishra, R. Pilloton, S. Jain, S. Roy, M. Khanuja, A. Mathur, J. Narang, Paper-Based Electrodes Conjugated with Tungsten Disulfide Nanostructure and Aptamer for Impedimetric Detection of Listeria monocytogenes, Biosensors (Basel). 12 (2022). https://doi.org/10.3390/bios12020088.

[15] M. Liss, B. Petersen, H. Wolf, E. Prohaska, An aptamer-based quartz crystal protein biosensor, Anal. Chem. 74 (2002) 4488–4495. https://doi.org/10.1021/ac011294p.

[16] M.B. Kulkarni, N.H. Ayachit, T.M. Aminabhavi, A Short Review on Miniaturized Biosensors for the Detection of Nucleic Acid Biomarkers, Biosensors (Basel). 13 (2023). https://doi.org/10.3390/bios13030412.

[17] K. Han, Z. Liang, N. Zhou, Design strategies for aptamer-based biosensors, Sensors 10 (2010) 4541–4557. https://doi.org/10.3390/s100504541.

[18] N.A. Hanjani, N. Esmaelizad, S. Zanganeh, A.T. Gharavi, P. Heidarizadeh, M. Radfar, F. Omidi, R. MacLoughlin, M. Doroudian, Emerging role of exosomes as biomarkers in cancer treatment and diagnosis, Crit. Rev. Oncol. Hematol. 169 (2022). https://doi.org/10.1016/j.critrevonc.2021.103565.

[19] Z. He, Z. Chen, M. Tan, S. Elingarami, Y. Liu, T. Li, Y. Deng, N. He, S. Li, J. Fu, W. Li, A review on methods for diagnosis of breast

cancer cells and tissues, Cell Prolif. 53 (2020). https://doi.org/10.1111/cpr.12822.

[20] S.H. Jafari, Z. Saadatpour, A. Salmaninejad, F. Momeni, M. Mokhtari, J.S. Nahand, M. Rahmati, H. Mirzaei, M. Kianmehr, Breast cancer diagnosis: Imaging techniques and biochemical markers, J. Cell. Physiol. 233 (2018) 5200–5213. https://doi.org/10.1002/jcp.26379.

[21] T.W.F. Yen, J. Li, R.A. Sparapani, P.W. Laud, A.B. Nattinger, The interplay between hospital and surgeon factors and the use of sentinel lymph node biopsy for breast cancer, Medicine (United States) 95 (2016). https://doi.org/10.1097/MD.0000000000004392.

[22] E.J. Abel, A. Carrasco, S.H. Culp, S.F. Matin, P. Tamboli, N.M. Tannir, C.G. Wood, Limitations of preoperative biopsy in patients with metastatic renal cell carcinoma: Comparison to surgical pathology in 405 cases, BJU Int. 110 (2012) 1742–1746. https://doi.org/10.1111/j.1464-410X.2012.11124.x.

[23] L. Wang, Early diagnosis of breast cancer, Sensors (Switzerland) 17 (2017). https://doi.org/10.3390/s17071572.

[24] C. Théry, E. Aikawa, M.J. Alcaraz, J.D. Anderson, A. Bedina Zavec, A. Benmoussa, A.C. Berardi, Minimal information for studies of extracellular vesicles 2018 (MISEV2018): a position statement of the International Society for Extracellular Vesicles and update of the MISEV2014 guidelines, J. Extracell. Vesicles 7 (2018). https://doi.org/10.1080/20013078.2018.1535750.

[25] J. Zhao, F. Shen, Y.M. Hu, K. Yin, Y. Chen, Y.J. Chen, Q.C. Hu, L. Liang, Prognostic value and microenvironmental crosstalk of exosome-related signatures in human epidermal growth factor receptor 2 positive breast cancer, Open Life Sci. 19 (2024). https://doi.org/10.1515/biol-2022-0899.

[26] N. McNamee, R. Daly, J. Crown, L. O'Driscoll, A method of separating extracellular vesicles from blood shows potential clinical translation, and reveals extracellular vesicle cargo gremlin-1 as a diagnostic biomarker, Transl. Oncol. 15 (2022). https://doi.org/10.1016/j.tranon.2021.101274.

[27] M. Wang, S. Ji, G. Shao, J. Zhang, K. Zhao, Z. Wang, A. Wu, Effect of exosome biomarkers for diagnosis and prognosis of

breast cancer patients, Clinical and Translational Oncology 20 (2018) 906–911. https://doi.org/10.1007/s12094-017-1805-0.

[28] J. Lin, J. Li, B. Huang, J. Liu, X. Chen, X.M. Chen, Y.M. Xu, L.F. Huang, X.Z. Wang, Exosomes: Novel Biomarkers for Clinical Diagnosis, Scientific World Journal 2015 (2015). https://doi.org/10.1155/2015/657086.

[29] L. Jiang, Y. Gu, Y. Du, J. Liu, Exosomes: Diagnostic Biomarkers and Therapeutic Delivery Vehicles for Cancer, Mol. Pharm. 16 (2019) 3333–3349. https://doi.org/10.1021/acs.molpharmaceut.9b00409.

[30] K.M. Ruppert, R.J. Kline, M.S. Rahman, Past, present, and future perspectives of environmental DNA (eDNA) metabarcoding: A systematic review in methods, monitoring, and applications of global eDNA, Glob. Ecol. Conserv. 17 (2019). https://doi.org/10.1016/j.gecco.2019.e00547.

[31] C. Anu Reddy, S. Oraon, S. Dayal Bharti, A. Kumar Yadav, S. Hazarika, Advancing Disease Management in Agriculture: A Review of Plant Pathology Techniques. Plant Science Archives, (2023) 16–18. https://doi.org/10.5147/PSA.2024.9.1.16.

[32] Q. Ali, S. Ahmar, M. Aamir Sohail, M. Kamran, M. Ali, M. Hamzah Saleem, M. Rizwan, A. Mushtaque Ahmed, F. Mora-Poblete, A. Teixeira do Amaral Júnior, M. Mubeen, S. Ali, Research advances and applications of biosensing technology for the diagnosis of pathogens in sustainable agriculture, (n.d.). https://doi.org/10.1007/s11356-021-12419-6/Published.

[33] T.R. Gordon, Fusarium oxysporum and the Fusarium Wilt Syndrome, Annu. Rev. Phytopathol. (2017) 15. https://doi.org/10.1146/annurev-phyto-080615.

[34] T.I. Ekwomadu, M. Mwanza, Fusarium Fungi Pathogens, Identification, Adverse Effects, Disease Management, and Global Food Security: A Review of the Latest Research, Agriculture (Switzerland) 13 (2023). https://doi.org/10.3390/agriculture13091810.

[35] X. Yan, S. Guo, K. Gao, S. Sun, C. Yin, Y. Tian, The Impact of the Soil Survival of the Pathogen of Fusarium Wilt on Soil Nutrient Cycling Mediated by Microorganisms, Microorganisms 11 (2023). https://doi.org/10.3390/microorganisms11092207.

[36] A.D. van Diepeningen, B. Brankovics, J. Iltes, T.A.J. van der Lee, C. Waalwijk, Diagnosis of Fusarium Infections: Approaches to Identification by the Clinical Mycology Laboratory, Curr. Fungal Infect. Rep. 9 (2015) 135–143. https://doi.org/10.1007/s12281-015-0225-2.

[37] D.R. Thévenot, K. Toth, R.A. Durst, G.S. Wilson, D.R. Thévenot, Electrochemical biosensors: recommended definitions and classification, 2001. www.elsevier.com/locate/bios.

[38] D.W.G. Morrison, M.R. Dokmeci, U. Demirci, A. Khademhosseini, Clinical Applications of Micro- and Nanoscale Biosensors, in: Biomedical Nanostructures, Wiley, 2007: pp. 439–460. https://doi.org/10.1002/9780470185834.ch17.

[39] B.B. Lal Srivastava, Biosensor-signal transducers, Fundamentals of Biosensors in Healthcare: Volume 1 (2025) 71–85. https://doi.org/10.1016/B978-0-443-21658-9.00029-2.

[40] Varnakavi. Naresh, N. Lee, A Review on Biosensors and Recent Development of Nanostructured Materials-Enabled Biosensors, Sensors 21 (2021) 1109. https://doi.org/10.3390/s21041109.

[41] C. Chen, J. Wang, Optical biosensors: An exhaustive and comprehensive review, Analyst 145 (2020) 1605–1628. https://doi.org/10.1039/c9an01998g.

[42] C. Karunakaran, R. Rajkumar, K. Bhargava, Introduction to Biosensors, in: Biosens. Bioelectron., Elsevier Inc., 2015: pp. 1–68. https://doi.org/10.1016/B978-0-12-803100-1.00001-3.

[43] P. Damborský, J. Švitel, J. Katrlík, Optical biosensors, Essays Biochem. 60 (2016) 91–100. https://doi.org/10.1042/EBC20150010.

[44] Y. Chen, J. Liu, Z. Yang, J.S. Wilkinson, X. Zhou, Optical biosensors based on refractometric sensing schemes: A review, Biosens. Bioelectron. 144 (2019). https://doi.org/10.1016/j.bios.2019.111693.

[45] G. Mie, Beiträge zur Optik trüber Medien, speziell kolloidaler Metallösungen, Ann. Phys. 330 (1908) 377–445. https://doi.org/10.1002/andp.19083300302.

[46] S. Kaye, Z. Zeng, M. Sanders, K. Chittur, P.M. Koelle, R. Lindquist, U. Manne, Y. Lin, J. Wei, Label-free detection of DNA

hybridization with a compact LSPR-based fiber-optic sensor, Analyst 142 (2017) 1974–1981. https://doi.org/10.1039/c7an00249a.

[47] C.F.. Bohren, D.R.. Huffman, Absorption and scattering of light by small particles, Wiley-VCH, 2009.

[48] O. Calvo-Lozano, M. Sierra, M. Soler, M.C. Estévez, L. Chiscano-Camón, A. Ruiz-Sanmartin, J.C. Ruiz-Rodriguez, R. Ferrer, J.J. González-López, J. Esperalba, C. Fernández-Naval, L. Bueno, R. López-Aladid, A. Torres, L. Fernández-Barat, S. Attoumani, R. Charrel, B. Coutard, L.M. Lechuga, Label-Free Plasmonic Biosensor for Rapid, Quantitative, and Highly Sensitive COVID-19 Serology: Implementation and Clinical Validation, Anal. Chem. 94 (2022) 975–984. https://doi.org/10.1021/acs.analchem.1c03850.

[49] N. Nath, A. Chilkoti, A colorimetric gold nanoparticle sensor to interrogate biomolecular interactions in real time on a surface, Anal. Chem. 74 (2002) 504–509. https://doi.org/10.1021/ac015657x.

[50] S. Alizadeh Bu-Ali, S. Alizadeh, Z. Nazari, A Review on Gold Nanoparticles Aggregation and Its Applications, Journal of Chemical Reviews 2 (2020) 228–242. https://doi.org/10.33945/SAMI/JCR.2020.4.2.

[51] S.A.. Maier, Plasmonics : fundamentals and applications, Springer, 2007.

[52] A. Bozzola, S. Perotto, F. De Angelis, Hybrid plasmonic-photonic whispering gallery mode resonators for sensing: A critical review, Analyst 142 (2017) 883–898. https://doi.org/10.1039/c6an02693a.

[53] G. Mie, Beiträge zur Optik trüber Medien, speziell kolloidaler Metallösungen, Ann. Phys. 330 (1908) 377–445. https://doi.org/10.1002/andp.19083300302.

[54] K.L. Kelly, E. Coronado, L.L. Zhao, G.C. Schatz, The optical properties of metal nanoparticles: The influence of size, shape, and dielectric environment, Journal of Physical Chemistry B 107 (2003) 668–677. https://doi.org/10.1021/jp026731y.

[55] G. Mie, Beiträge zur Optik trüber Medien, speziell kolloidaler Metallösungen, Ann. Phys. 330 (1908) 377–445. https://doi.org/10.1002/andp.19083300302.

[56] S. Link, M.A. El-Sayed, Shape and size dependence of radiative, non-radiative and photothermal properties of gold nanocrystals, Int. Rev. Phys. Chem. 19 (2000) 409–453. https://doi.org/10.1080/01442350050034180.

[57] PART I FUNDAMENTALS OF PLASMONICS, n.d.

[58] K.M. Mayer, J.H. Hafner, Localized surface plasmon resonance sensors, Chem. Rev. 111 (2011) 3828–3857. https://doi.org/10.1021/cr100313v.

[59] S0009261410001193 (1), (n.d.).

[60] S.K. Ghosh, T. Pal, Interparticle coupling effect on the surface plasmon resonance of gold nanoparticles: From theory to applications, Chem. Rev. 107 (2007) 4797–4862. https://doi.org/10.1021/cr0680282.

[61] P.K. Jain, X. Huang, I.H. El-Sayed, M.A. El-Sayed, Review of some interesting surface plasmon resonance-enhanced properties of noble metal nanoparticles and their applications to biosystems, Plasmonics 2 (2007) 107–118. https://doi.org/10.1007/s11468-007-9031-1.

[62] S.A. Maier, M.L. Brongersma, P.G. Kik, H.A. Atwater, Observation of near-field coupling in metal nanoparticle chains using far-field polarization spectroscopy, Phys. Rev. B Condens. Matter Mater. Phys. 65 (2002) 1–4. https://doi.org/10.1103/PhysRevB.65.193408.

[63] B. Della Ventura, M. Cennamo, A. Minopoli, R. Campanile, S.B. Censi, D. Terracciano, G. Portella, R. Velotta, Colorimetric test for fast detection of SARS-COV-2 in nasal and throat swabs, ACS Sens. 5 (2020) 3043–3048. https://doi.org/10.1021/acssensors.0c01742.

[64] G. Matteoli, S. Luin, L. Bellucci, R. Nifosì, F. Beltram, G. Signore, Aptamer-based gold nanoparticle aggregates for ultrasensitive amplification-free detection of PSMA, Sci. Rep. 13 (2023). https://doi.org/10.1038/s41598-023-46974-4.

[65] L. Gunnarsson, T. Rindzevicius, J. Prikulis, B. Kasemo, M. Käll, S. Zou, G.C. Schatz, Confined plasmons in nanofabricated single silver particle pairs: Experimental observations of strong interparticle interactions, Journal of Physical Chemistry B 109 (2005) 1079–1087. https://doi.org/10.1021/jp049084e.

[66] B. Sepúlveda, P.C. Angelomé, L.M. Lechuga, L.M. Liz-Marzán, LSPR-based nanobiosensors, Nano Today 4 (2009) 244–251. https://doi.org/10.1016/j.nantod.2009.04.001.

[67] I.M. White, X. Fan, Optical resonators; (230.3990) Micro-optical devices, (2008). https://doi.org/10.1007/s10404-007.

[68] N.L. Kazanskiy, S.N. Khonina, M.A. Butt, Plasmonic sensors based on Metal-insulator-metal waveguides for refractive index sensing applications: A brief review, Physica E Low. Dimens. Syst. Nanostruct. 117 (2020). https://doi.org/10.1016/j.physe.2019.113798.

[69] D. Marra, A. Acunzo, A. Fulgione, M. De Luca, R. Villalonga, F. Pisani, L. Biondi, F. Capuano, R. Velotta, B. Della Ventura, V. Iannotti, Advances in gluten detection: A rapid colorimetric approach using core-satellite magnetic particles, Biosens. Bioelectron. X 21 (2024). https://doi.org/10.1016/j.biosx.2024.100545.

[70] D. Zhai, W. Xu, L. Zhang, Y.T. Chang, The role of “disaggregation” in optical probe development, Chem. Soc. Rev. 43 (2014) 2402–2411. https://doi.org/10.1039/c3cs60368g.

[71] S. Zeng, K.T. Yong, I. Roy, X.Q. Dinh, X. Yu, F. Luan, A Review on Functionalized Gold Nanoparticles for Biosensing Applications, Plasmonics 6 (2011) 491–506. https://doi.org/10.1007/s11468-011-9228-1.

[72] M.R. Kumalasari, R. Alfanaar, A.S. Andreani, Gold nanoparticles (AuNPs): A versatile material for biosensor application, Talanta Open 9 (2024). https://doi.org/10.1016/j.talo.2024.100327.

[73] P. Suchomel, L. Kvitek, R. Prucek, A. Panacek, A. Halder, S. Vajda, R. Zboril, Simple size-controlled synthesis of Au nanoparticles and their size-dependent catalytic activity, Sci. Rep. 8 (2018). https://doi.org/10.1038/s41598-018-22976-5.

[74] M. Kus-liśkiewicz, P. Fickers, I. Ben Tahar, Biocompatibility and cytotoxicity of gold nanoparticles: Recent advances in methodologies and regulations, Int. J. Mol. Sci. 22 (2021). https://doi.org/10.3390/ijms222010952.

[75] Y. Ghafari, A. Asefnejad, D. Otasowie Ogbemudia, Gold Nanoparticles in Biomedicine: Advancements in Cancer Therapy, Drug Delivery, Diagnostics, and Tissue Regeneration, n.d. https://scientifichypotheses.org/.

[76] P. Sakore, S. Bhattacharya, S. Belemkar, B.G. Prajapati, G.M. Elossaily, The theranostic potential of green nanotechnology-enabled gold nanoparticles in cancer: A paradigm shift on diagnosis and treatment approaches, Results Chem. 7 (2024). https://doi.org/10.1016/j.rechem.2023.101264.

[77] faraday-1997-x-the-bakerian-lecture-experimental-relations-of-gold-(and-other-metals)-to-light, (n.d.).

[78] N. Nuraje, S. Mohammed, L. Yang, H. Matsui, Biomineralization nanolithography: Combination of bottom-up and top-down fabrication to grow arrays of monodisperse gold nanopartieles along peptide lines, Angewandte Chemie - International Edition 48 (2009) 2546–2548. https://doi.org/10.1002/anie.200805145.

[79] M. Liu, X. Xue, B. Karmakar, W. Eltantawy, A.F. El-Kott, E.M. El Nashar, E.M. Abd-Ella, Sonochemical synthesis of gold nanoparticles mediated by potato starch: Its performance in the treatment of esophageal cancer, Open Chem. 22 (2024). https://doi.org/10.1515/chem-2023-0193.

[80] A. Tsarapkin, K. Maćkosz, C.S. Jureddy, I. Utke, K. Höflich, Area-Selective Chemical Vapor Deposition of Gold by Electron Beam Seeding, Advanced Materials 36 (2024). https://doi.org/10.1002/adma.202313571.

[81] D.A. Migulin, J. V. Rozanova, A.A. Zharikov, V.I. Feldman, O. V. Emelyanova, A.A. Zezin, Preparation of gold nanoparticles by photolysis and radiolysis in alcohol solutions of functional hyperbranched polyorganosiloxane/H[AuCl4]: Effect of irradiation mode on nanoparticle size and formation mechanism, J. Photochem. Photobiol. A Chem. 458 (2025). https://doi.org/10.1016/j.jphotochem.2024.115980.

[82] J. Turkevich, P.C. Stevenson, J. Hillier, A study of the nucleation and growth processes in the synthesis of colloidal gold, Discuss. Faraday Soc. 11 (1951) 55–75. https://doi.org/10.1039/DF9511100055.

[83] T. Patil, R. Gambhir, A. Vibhute, A.P. Tiwari, Gold Nanoparticles: Synthesis Methods, Functionalization and Biological Applications, J. Clust. Sci. 34 (2023) 705–725. https://doi.org/10.1007/s10876-022-02287-6.

[84] T.M.S. Erlangga, A.B.D. Nandiyanto, R. Ragadhita, Preliminary reactor design for the gold nanoparticles production by the Turkevich method on an industrial scale, Sustainable Engineering and Innovation 5 (2023) 22–30. https://doi.org/10.37868/sei.v5i1.id191.

[85] V. Amendola, M. Meneghetti, Size evaluation of gold nanoparticles by UV-vis spectroscopy, Journal of Physical Chemistry C 113 (2009) 4277–4285. https://doi.org/10.1021/jp8082425.

[86] W. Haiss, N.T.K. Thanh, J. Aveyard, D.G. Fernig, Determination of size and concentration of gold nanoparticles from UV-Vis spectra, Anal. Chem. 79 (2007) 4215–4221. https://doi.org/10.1021/ac0702084.

[87] G. Zhang, Functional gold nanoparticles for sensing applications, Nanotechnol. Rev. 2 (2013) 269–288. https://doi.org/10.1515/ntrev-2012-0088.

[88] S. Alex, A. Tiwari, Functionalized gold nanoparticles: Synthesis, properties and applications-A review, J. Nanosci. Nanotechnol. 15 (2015) 1869–1894. https://doi.org/10.1166/jnn.2015.9718.

[89] J.M. Carnerero, A. Jimenez-Ruiz, P.M. Castillo, R. Prado-Gotor, Covalent and Non-Covalent DNA–Gold-Nanoparticle Interactions: New Avenues of Research, ChemPhysChem 18 (2017) 17–33. https://doi.org/10.1002/cphc.201601077.

[90] Z. Xue, L. Wang, S. Pan, J. Yan, M. You, C. Yao, The nucleic acid reactions on the nanomaterials surface for biomedicine, Journal of Nanobiotechnology 23 (2025). https://doi.org/10.1186/s12951-025-03374-2.

[91] S. Shi, J. Chen, X. Wang, M. Xiao, A.R. Chandrasekaran, L. Li, C. Yi, H. Pei, Biointerface Engineering with Nucleic Acid Materials for Biosensing Applications, Adv. Funct. Mater. 32 (2022). https://doi.org/10.1002/adfm.202201069.

[92] T.P. Patil, A.A. Vibhute, A. Vinu, A. Pandey-Tiwari, Nucleic acid conjugated gold nanoparticles for biosensing applications: a review, World J. Microbiol. Biotechnol. 41 (2025). https://doi.org/10.1007/s11274-025-04454-z.

[93] C.O. Timmons, W.A. Zisman, G.L. Gaines, D.L. Allara, R.G. Nuzzo, H.W. Langmuir ; Thompson, N.P. Skerrett, Methanethiol-^ (CD3SH) was obtained from Merck Sharp & Dohme11) (a) Weak scattering was also seen for the case of methanethiol chemisorption, Press, 1987.

[94] D.Y. Choi, S. Kim, J.W. Oh, J.M. Nam, Conjugation strategies of DNA to gold nanoparticles, Bull. Korean Chem. Soc. 43 (2022) 1298–1306. https://doi.org/10.1002/bkcs.12621.

[95] J.J. Storhoff, R.C. Muck, C.A. Mirkin, Strategies for Organizing Nanoparticles into Aggregate Structures and Functional Materials, 1997.

[96] X. Zhang, M.R. Servos, J. Liu, Instantaneous and quantitative functionalization of gold nanoparticles with thiolated DNA using a pH-assisted and surfactant-free route, J. Am. Chem. Soc. 134 (2012) 7266–7269. https://doi.org/10.1021/ja3014055.

[97] B. Liu, J. Liu, Freezing Directed Construction of Bio/Nano Interfaces: Reagentless Conjugation, Denser Spherical Nucleic Acids, and Better Nanoflares, J. Am. Chem. Soc. 139 (2017) 9471–9474. https://doi.org/10.1021/jacs.7b04885.

[98] R. O'concubhair, J.R. Sodeau, The effect of freezing on reactions with environmental impact, Acc. Chem. Res. 46 (2013) 2716–2724. https://doi.org/10.1021/ar400114e.

[99] B. Liu, J. Liu, Freezing-Driven DNA Adsorption on Gold Nanoparticles: Tolerating Extremely Low Salt Concentration but Requiring High DNA Concentration, Langmuir 35 (2019) 6476–6482. https://doi.org/10.1021/acs.langmuir.9b00746.

[100] Y. Hao, Y. Li, L. Song, Z. Deng, Flash Synthesis of Spherical Nucleic Acids with Record DNA Density, J. Am. Chem. Soc. 143 (2021) 3065–3069. https://doi.org/10.1021/jacs.1c00568.

[101] Z. Ye, W. Liao, Z. Deng, L. Wang, B. Wen, D. Zhang, H. Wang, W. Xie, H. Peng, Fast-track synthesis of DNA-functionalized gold nanoparticles for biosensing applications, TrAC - Trends in Analytical Chemistry 175 (2024). https://doi.org/10.1016/j.trac.2024.117724.

[102] M. Enea, A. Leite, R. Franco, E. Pereira, Gold Nanoprobes for Robust Colorimetric Detection of Nucleic Acid Sequences Related to Disease Diagnostics, Nanomaterials 14 (2024) 1833. https://doi.org/10.3390/nano14221833.

[103] A.D. Ellington, J.W. Szostak, In vitro selection of RNA molecules that bind specific ligands, Nature 346 (1990) 818–822. https://doi.org/10.1038/346818a0.

[104] C. Tuerk, L. Gold, Systematic Evolution of Ligands by Exponential Enrichment: RNA Ligands to Bacteriophage T4 DNA Polymerase, n.d. https://www.science.org.

[105] C. Zhu, L. Li, Z. Wang, M. Irfan, F. Qu, Recent advances of aptasensors for exosomes detection, Biosens. Bioelectron. 160 (2020). https://doi.org/10.1016/j.bios.2020.112213.

[106] E. Bazzan, M. Tinè, A. Casara, D. Biondini, U. Semenzato, E. Cocconcelli, E. Balestro, M. Damin, C.M. Radu, G. Turato, S. Baraldo, P. Simioni, P. Spagnolo, M. Saetta, M.G. Cosio, Critical review of the evolution of extracellular vesicles' knowledge: From 1946 to today, Int. J. Mol. Sci. 22 (2021). https://doi.org/10.3390/ijms22126417.

[107] S. Chia, Y.P. Low, Q. Wang, P. Li, Z. Gao, Advances in Exosome Quantification Techniques, n.d.

[108] C.L. Esposito, C. Quintavalle, F. Ingenito, D. Rotoli, G. Roscigno, S. Nuzzo, R. Thomas, S. Catuogno, V. de Franciscis, G. Condorelli, Identification of a novel RNA aptamer that selectively targets breast cancer exosomes, Mol. Ther. Nucleic Acids 23 (2021) 982–994. https://doi.org/10.1016/j.omtn.2021.01.012.

[109] W. Qin, L. Wang, H. Tian, X. Wu, C. Xiao, Y. Pan, M. Fan, Y. Tai, W. Liu, Q. Zhang, Y. Yang, CAF-derived exosomes transmitted

Gremlin-1 promotes cancer progression and decreases the sensitivity of hepatoma cells to sorafenib, Mol. Carcinog. 61 (2022) 764–775. https://doi.org/10.1002/mc.23416.

[110] Nucleic Acid Hybridization - an overview | ScienceDirect Topics, (n.d.). https://www.sciencedirect.com/topics/engineering/nucleic-acid-hybridization (accessed September 23, 2025).

[111] H.T. Ngo, N. Gandra, A.M. Fales, S.M. Taylor, T. Vo-Dinh, Sensitive DNA detection and SNP discrimination using ultrabright SERS nanorattles and magnetic beads for malaria diagnostics, Biosens. Bioelectron. 81 (2016) 8–14. https://doi.org/10.1016/j.bios.2016.01.073.

[112] E. Dester, K. Kao, E.C. Alocilja, Detection of Unamplified E. coli O157 DNA Extracted from Large Food Samples Using a Gold Nanoparticle Colorimetric Biosensor, Biosensors (Basel). 12 (2022). https://doi.org/10.3390/bios12050274.

[113] S.T. Rishan, R.J. Kline, M.S. Rahman, Applications of environmental DNA (eDNA) to detect subterranean and aquatic invasive species: A critical review on the challenges and limitations of eDNA metabarcoding, Environmental Advances 12 (2023). https://doi.org/10.1016/j.envadv.2023.100370.

[114] M.W. Pedersen, S. Overballe-Petersen, L. Ermini, C. Der Sarkissian, J. Haile, M. Hellstrom, J. Spens, P.F. Thomsen, K. Bohmann, E. Cappellini, I.B. Schnell, N.A. Wales, C. Carøe, P.F. Campos, A.M.Z. Schmidt, M.T.P. Gilbert, A.J. Hansen, L. Orlando, E. Willerslev, Ancient and modern environmental DNA, Philosophical Transactions of the Royal Society B: Biological Sciences 370 (2015). https://doi.org/10.1098/rstb.2013.0383.

[115] E. Jackson, J. Li, T. Weerasinghe, X. Li, The Ubiquitous Wilt-Inducing Pathogen Fusarium oxysporum—A Review of Genes Studied with Mutant Analysis, Pathogens 13 (2024). https://doi.org/10.3390/pathogens13100823.

[116] Q. Zuriegat, Y. Zheng, H. Liu, Z. Wang, Y. Yun, Current progress on pathogenicity-related transcription factors in Fusarium oxysporum, Mol. Plant Pathol. 22 (2021) 882–895. https://doi.org/10.1111/mpp.13068.

[117] Y. Lu, J. Liu, Functional DNA nanotechnology: emerging applications of DNAzymes and aptamers, Curr. Opin. Biotechnol.

17 (2006) 580–588. https://doi.org/10.1016/j.copbio.2006.10.004.

[118] K. Hasegawa, E. Porter, O. Nazarov, Analysis of homogeneous layer approximations in the modeling of localized surface plasmon resonance biosensors, Appl. Opt. 58 (2019) 6519. https://doi.org/10.1364/AO.58.006519.

[119] D. Foiles, K. Hasegawa, Theoretical approach for modeling LSPR biosensors for the detection of biopolymer nucleation, Appl. Opt. 60 (2021) 9303. https://doi.org/10.1364/AO.435364.

[120] S. Elhadj, G. Singh, R.F. Saraf, Optical Properties of an Immobilized DNA Monolayer from 255 to 700 nm, Langmuir 20 (2004) 5539–5543. https://doi.org/10.1021/la049653.

[121] Z. Bradley, D. Cunningham, N. Bhalla, Refractive Index-Modulated LSPR Sensing in 20–120 nm Gold and Silver Nanoparticles: A Simulation Study, ECS Sensors Plus 2 (2023) 043402. https://doi.org/10.1149/2754-2726/ad08d8.

[122] H.D. Hill, J.E. Millstone, M.J. Banholzer, C.A. Mirkin, The Role Radius of Curvature Plays in Thiolated Oligonucleotide Loading on Gold Nanoparticles, ACS Nano 3 (2009) 418–424. https://doi.org/10.1021/nn800726e.

[123] X. Liu, Y. Zhao, Y. Ding, J. Wang, J. Liu, Stabilization of Gold Nanoparticles by Hairpin DNA and Implications for Label-Free Colorimetric Biosensors, Langmuir 38 (2022) 5542–5549. https://doi.org/10.1021/acs.langmuir.2c00119.

[124] X. Wang, Z. Yang, Y. Li, K. Huang, N. Cheng, Towards rational design: Developing universal freezing routes for anchoring DNA onto gold nanoparticles, J. Colloid Interface Sci. 655 (2024) 830–840. https://doi.org/10.1016/j.jcis.2023.11.041.

[125] M. Hu, C. Yuan, T. Tian, X. Wang, J. Sun, E. Xiong, X. Zhou, Single-Step, Salt-Aging-Free, and Thiol-Free Freezing Construction of AuNP-Based Bioprobes for Advancing CRISPR-Based Diagnostics, J. Am. Chem. Soc. 142 (2020) 7506–7513. https://doi.org/10.1021/jacs.0c00217.

[126] R. Dutour, G. Bruylants, Gold Nanoparticles Coated with Nucleic Acids: An Overview of the Different Bioconjugation Pathways,

Bioconjug. Chem. 36 (2025) 1133–1156. https://doi.org/10.1021/acs.bioconjchem.5c00098.

[127] F. Liu, H. Wu, Q. Chen, J. Gao, G. Wang, Demonstration of a Magic Reaction: Accelerating DNA Functionalization of Gold Nanoparticles by Freezing, J. Chem. Educ. 100 (2023) 2009–2014. https://doi.org/10.1021/acs.jchemed.3c00022.

[128] N. Harbeck, M. Gnant, Breast cancer, The Lancet 389 (2017) 1134–1150. https://doi.org/10.1016/S0140-6736(16)31891-8.

[129] Advancements in Early Detection and Targeted Therapies for Breast Cancer; A Comprehensive Analysis, Asia Pacific Journal of Cancer Research 1 (2024). https://doi.org/10.70818/apjcr.2024.v01i01.04.

[130] D.P. Joyce, M.J. Kerin, R.M. Dwyer, Exosome-encapsulated microRNAs as circulating biomarkers for breast cancer, Int. J. Cancer 139 (2016) 1443–1448. https://doi.org/10.1002/ijc.30179.

[131] M. Madani, M.M. Behzadi, S. Nabavi, The Role of Deep Learning in Advancing Breast Cancer Detection Using Different Imaging Modalities: A Systematic Review, Cancers (Basel). 14 (2022). https://doi.org/10.3390/cancers14215334.

[132] P.J. Ho, C.M. Bok, H.M. Mohd Ishak, L.Y. Lim, J. Liu, F.Y. Wong, K.S. Chia, M.H. Tan, W.Y. Chay, M. Hartman, J. Li, Factors associated with false-positive mammography at first screen in an Asian population, PLoS One 14 (2019). https://doi.org/10.1371/journal.pone.0213615.

[133] J. Li, X. Guan, Z. Fan, L.M. Ching, Y. Li, X. Wang, W.M. Cao, D.X. Liu, Non-invasive biomarkers for early detection of breast cancer, Cancers (Basel). 12 (2020) 1–28. https://doi.org/10.3390/cancers12102767.

[134] M.E. Sherman, R.A. Vierkant, S.J. Winham, C.M. Vachon, J.M. Carter, L. Pacheco-Spann, M.R. Jensen, B.M. McCauley, T.L. Hoskin, L. Seymour, D. Gehling, J. Fischer, K. Ghosh, D.C. Radisky, A.C. Degnim, Benign Breast Disease and Breast Cancer Risk in the Percutaneous Biopsy Era, JAMA Surg. 159 (2024) 193–201. https://doi.org/10.1001/jamasurg.2023.6382.

[135] J. Gooding, The Liquid Biopsy, ACS Sens. 10 (2025) 3192–3193. https://doi.org/10.1021/acssensors.5c01389.

[136] R. Yadav, A.V. Singh, S. Kushwaha, D.S. Chauhan, Emerging role of exosomes as a liquid biopsy tool for diagnosis, prognosis &; monitoring treatment response of communicable &; noncommunicable diseases, Indian Journal of Medical Research 159 (2024) 163–180. https://doi.org/10.4103/ijmr.ijmr_2344_22.

[137] F. Najafzadeh, F. Ghasemi, M.R. Hormozi-Nezhad, Anti-aggregation of gold nanoparticles for metal ion discrimination: A promising strategy to design colorimetric sensor arrays, Sens. Actuators B Chem. 270 (2018) 545–551. https://doi.org/10.1016/j.snb.2018.05.065.

[138] R. Kataria, K. Sethuraman, D. Vashisht, A. Vashisht, S.K. Mehta, A. Gupta, Colorimetric detection of mercury ions based on anti-aggregation of gold nanoparticles using 3, 5-dimethyl-1-thiocarboxamidepyrazole, Microchemical Journal 148 (2019) 299–305. https://doi.org/10.1016/j.microc.2019.04.068.

[139] Y. Aoshima, Y. Enomoto, S. Muto, S. Meguro, H. Kawasaki, I. Kosugi, T. Fujisawa, N. Enomoto, N. Inui, Y. Nakamura, T. Suda, T. Iwashita, Gremlin-1 for the Differential Diagnosis of Idiopathic Pulmonary Fibrosis Versus Other Interstitial Lung Diseases: A Clinical and Pathophysiological Analysis, Lung 199 (2021) 289–298. https://doi.org/10.1007/s00408-021-00440-y.

[140] C. Quintavalle, F. Ingenito, G. Roscigno, B. Pattanayak, C.L. Esposito, A. Affinito, D. Fiore, G. Petrillo, S. Nuzzo, B. Della Ventura, F. D'Aria, C. Giancola, S. Mitola, E. Grillo, M. Pirozzi, G. Donati, F.S. Di Leva, L. Marinelli, Z. Minic, F. De Micco, G. Thomas, M. V. Berezovski, G. Condorelli, Ex.50.T aptamer impairs tumor–stroma cross-talk in breast cancer by targeting gremlin-1, Cell Death Discov. 11 (2025). https://doi.org/10.1038/s41420-025-02363-6.

[141] C.L. Esposito, C. Quintavalle, F. Ingenito, D. Rotoli, G. Roscigno, S. Nuzzo, R. Thomas, S. Catuogno, V. de Franciscis, G. Condorelli, Identification of a novel RNA aptamer that selectively targets breast cancer exosomes, Mol. Ther. Nucleic Acids 23 (2021) 982–994. https://doi.org/10.1016/j.omtn.2021.01.012.

[142] N. McNamee, R. Daly, J. Crown, L. O'Driscoll, A method of separating extracellular vesicles from blood shows potential clinical translation, and reveals extracellular vesicle cargo

gremlin-1 as a diagnostic biomarker, Transl. Oncol. 15 (2022). https://doi.org/10.1016/j.tranon.2021.101274.

[143] T. Çevik, N. Çevik, Environmental DNA (eDNA): A review of ecosystem biodiversity detection and applications, Biodivers. Conserv. 34 (2025) 2999–3035. https://doi.org/10.1007/s10531-025-03112-y.

[144] H.J. Yoon, J.H. Seo, S.H. Shin, M.A.A. Abdelhamid, S.P. Pack, Bioinformation and Monitoring Technology for Environmental DNA Analysis: A Review, Biosensors (Basel). 15 (2025) 494. https://doi.org/10.3390/bios15080494.

[145] M. Schwentner, R. Zahiri, S. Yamamoto, M. Husemann, B. Kullmann, R. Thiel, eDNA as a tool for non-invasive monitoring of the fauna of a turbid, well-mixed system, the Elbe estuary in Germany, PLoS One 16 (2021). https://doi.org/10.1371/journal.pone.0250452.

[146] M. Tan, C. Liao, L. Liang, X. Yi, Z. Zhou, G. Wei, Recent advances in recombinase polymerase amplification: Principle, advantages, disadvantages and applications, Front. Cell. Infect. Microbiol. 12 (2022). https://doi.org/10.3389/fcimb.2022.1019071.

[147] L. Becherer, N. Borst, M. Bakheit, S. Frischmann, R. Zengerle, F. Von Stetten, Loop-mediated isothermal amplification (LAMP)-review and classification of methods for sequence-specific detection, Analytical Methods 12 (2020) 717–746. https://doi.org/10.1039/c9ay02246e.

[148] K. Sharma, M. Sharma, Optical biosensors for environmental monitoring: Recent advances and future perspectives in bacterial detection, Environ. Res. 236 (2023) 116826. https://doi.org/10.1016/j.envres.2023.116826.

[149] J. Zhou, Y. Liu, X. Du, Y. Gui, J. He, F. Xie, J. Cai, Recent Advances in Design and Application of Nanomaterials-Based Colorimetric Biosensors for Agri-food Safety Analysis, ACS Omega 8 (2023) 46346–46361. https://doi.org/10.1021/acsomega.3c06409.

[150] A. Acunzo, E. Scardapane, M. De Luca, D. Marra, R. Velotta, A. Minopoli, Plasmonic Nanomaterials for Colorimetric Biosensing:

A Review, Chemosensors 10 (2022). https://doi.org/10.3390/chemosensors10040136.

[151] J. Flood, A review of fusarium wilt of oil palm caused by Fusarium oxysporum f. sp. elaeidis, in: Phytopathology, 2006: pp. 660–662. https://doi.org/10.1094/PHYTO-96-0660.

[152] E. Jackson, J. Li, T. Weerasinghe, X. Li, The Ubiquitous Wilt-Inducing Pathogen Fusarium oxysporum—A Review of Genes Studied with Mutant Analysis, Pathogens 13 (2024). https://doi.org/10.3390/pathogens13100823.

[153] R. Joshi, A review of Fusarium oxysporum on its plant interaction and industrial use, ~ 112 ~ Journal of Medicinal Plants Studies 6 (2018) 112–115.

[154] K. Mendgen, M. Hahn, H. Deising, Annual Reviews MENDTEXT.DUN AR14-19, 1996.

[155] F. Matarese, S. Sarrocco, S. Gruber, V. Seidl-Seiboth, G. Vannacci, Biocontrol of Fusarium head blight: Interactions between Trichoderma and mycotoxigenic Fusarium, Microbiology (N Y). 158 (2012) 98–106. https://doi.org/10.1099/mic.0.052639-0.

[156] R. Sarnaik, J. Shelake, M. Waghmare, Fusarium wilt of brinjal: impact, pathogenicity, and sustainable management strategies, Discover Plants 2 (2025). https://doi.org/10.1007/s44372-025-00331-z.

[157] C. Alabouvette, P. Lemanceau, C. Steinberg, Recent advances in the biological control of fusarium wilts, Pestic. Sci. 37 (1993) 365–373. https://doi.org/10.1002/ps.2780370409.

[158] X. Yan, S. Guo, K. Gao, S. Sun, C. Yin, Y. Tian, The Impact of the Soil Survival of the Pathogen of Fusarium Wilt on Soil Nutrient Cycling Mediated by Microorganisms, Microorganisms 11 (2023). https://doi.org/10.3390/microorganisms11092207.

[159] C.A. Mirkin, R.L. Letsinger, R.C. Mucic, J.J. Storhoff, A DNA-based method for rationally assembling nanoparticles into macroscopic materials, Nature 382 (1996) 607–609. https://doi.org/10.1038/382607a0.

[160] K. Sato, K. Hosokawa, M. Maeda, Non-cross-linking gold nanoparticle aggregation as a detection method for single-base

substitutions., Nucleic Acids Res. 33 (2005). https://doi.org/10.1093/nar/gni007.

[161] H. Ahmadpour-Yazdi, M.R. Hormozi-Nezhad, A.R. Abadi, M.H. Sanati, B. Kazemi, Colorimetric assay for exon 7 SMN1/SMN2 single nucleotide polymorphism using gold nanoprobes, BioImpacts 3 (2013) 185–194. https://doi.org/10.5681/bi.2013.037.

[162] G. Wang, Y. Akiyama, S. Shiraishi, N. Kanayama, T. Takarada, M. Maeda, Cross-linking versus non-cross-linking aggregation of gold nanoparticles induced by DNA hybridization: A comparison of the rapidity of solution color change, Bioconjug. Chem. 28 (2017) 270–277. https://doi.org/10.1021/acs.bioconjchem.6b00410.

[163] Z. Heidari, S.E. Rezatofighi, S. Rastegarzadeh, Development and comparison of cross-linking and non-crosslinking probe-gold nanoparticle hybridization assays for direct detection of unamplified bovine viral diarrhea virus-RNA, BMC Biotechnol. 21 (2021). https://doi.org/10.1186/s12896-021-00691-w.

[164] K. Sato, K. Hosokawa, M. Maeda, Rapid aggregation of gold nanoparticles induced by non-cross-linking DNA hybridization, J. Am. Chem. Soc. 125 (2003) 8102–8103. https://doi.org/10.1021/ja034876s.

[165] Y. Xu, K. Huang, A. Lopez, W. Xu, J. Liu, Freezing promoted hybridization of very short DNA oligonucleotides, Chemical Communications 55 (2019) 10300–10303. https://doi.org/10.1039/c9cc04608a.

[166] B. Liu, T. Wu, Z. Huang, Y. Liu, J. Liu, Freezing-directed Stretching and Alignment of DNA Oligonucleotides, Angewandte Chemie 131 (2019) 2131–2135. https://doi.org/10.1002/ange.201814352.

[167] T. D'Aponte, M. De Luca, E. de Alteriis, F. Cartenì, S. Mazzoleni, R. Velotta, V. Iannotti, B. Della Ventura, Electrochemical biosensor with custom fluidics for amplification-free, low-picomolar DNA detection, Anal. Chim. Acta 1374 (2025). https://doi.org/10.1016/j.aca.2025.344554.

[168] H. Moulahoum, F. Ghorbanizamani, The LOD paradox: When lower isn't always better in biosensor research and development,

Biosens. Bioelectron. 264 (2024). https://doi.org/10.1016/j.bios.2024.116670.

[169] J.J. Hao, M.E. Yang, R.M. Davis, Effect of soil inoculum density of fusarium oxysporum f. sp. vasinfectum race 4 on disease development in cotton, Plant Dis. 93 (2009) 1324–1328. https://doi.org/10.1094/PDIS-93-12-1324.

[170] A. Bellini, G. Gilardi, M. Idbella, M. Zotti, M. Pugliese, G. Bonanomi, M.L. Gullino, Trichoderma enriched compost, BCAs and potassium phosphite control Fusarium wilt of lettuce without affecting soil microbiome at genus level, Applied Soil Ecology 182 (2023). https://doi.org/10.1016/j.apsoil.2022.104678.

[171] A.R. Shafiqa, A. Abdul Aziz, B. Mehrdel, Nanoparticle Optical Properties: Size Dependence of a Single Gold Spherical Nanoparticle, in: J. Phys. Conf. Ser., Institute of Physics Publishing, 2018. https://doi.org/10.1088/1742-6596/1083/1/012040.

Appendix

Gantt chart

Publications

- Rapid Label-Free Colorimetric ssDNA Biosensor Based on Gold Nanoparticles: Application *to Fusarium oxysporum* Detection in Soil.
  Erica Cavaliere, Tina D'Aponte, Emanuela Palomba, Maurizio Zotti, Pasquale Termolino, Vincenzo Iannotti, Stefano Mazzoleni, Raffaele Velotta, Bartolomeo Della Ventura
  Article under review at Microchemical Journal

- Colorimetric Aptasensor for Exosome Detection in Breast Cancer Liquid Biopsy.
  Bartolomeo Della Ventura, Cristina Quintavalle, Erica Cavaliere, Kristin Tkalčec, Paolo Aniello,Vincenzo Iannotti, Gerolama Condorelli, and Raffele Velotta
  Article under review at Sensors and Actuators B: Chemical.

Conferences and schools

7–8 February 2024: Poster presentation titled *"Rapid colorimetric biosensor for the detection of environmental DNA"* at the Agritech Mid-Term Meeting, Portici (Italy).

3–7 June 2024: Attendance of the 5th edition of the *National School of Optical Biosensors and Biophotonics (BiO&B)*, organized by the Italian Society of Optics and Photonics (SIOF), Lecce .

3–5 October 2024: Oral presentation titled *"Development of a colorimetric biosensor for the detection of environmental DNA"* at the Eleventh International Workshop on Biosensors, Marrakech (Morocco).

4 July 2025: Attendance of the Advanced Course in the Design of Nucleic Acid-Functionalized Nanostructured Materials for Therapeutic and Diagnostic Applications, Hotel Marad, Torre del Greco (Italy).

26–29 October 2025: Poster and Flash Presentation titled *"A user-friendly and rapid colorimetric biosensor for environmental DNA detection"* at the 5th European Biosensor Symposium (EBS 2025), Tarragona (Spain).

12–14 November 2025: Participation in the 12th International Electronic Conference on Sensors and Applications, held online.

17–19 November 2025: Poster presentation titled *"Rapid DNA-based colorimetric biosensor for Fusarium oxysporum detection"* at the 11th International Symposium on Sensor Science (I3S 2025), Barcelona (Spain).

Colorimetric Aptasensor for Exosome Detection in Breast Cancer Liquid Biopsy

Bartolomeo Della Ventura[1], Cristina Quintavalle[2], Erica Cavaliere[1], Kristin Tkalčec[3], Paolo Aniello[1], Vincenzo Iannotti[1,4], Gerolama Condorelli[2,3*], and Raffele Velotta[1*]

[1]Department of Physics "Ettore Pancini", University of Naples Federico II, Via Cintia 26 - 80126 Naples (Italy)

[2]CNR-Institute of Endotypes in Oncology, Metabolism and Immunology "G. Salvatore" (IEOMI), Via Sergio Pansini, 5 - 80131 Naples (Italy)

[3]Department of Molecular Medicine and Medical Biotechnology, University of Naples Federico II, Via Sergio Pansini, 5 - 80131 Naples (Italy)

[4]CNR–Institute for SuPerconductors, INnovative materials, and devices (SPIN), Via Cintia 26 - 80126 Naples (Italy)

*Corresponding authors: rvelotta@unina.it; gecondor@unina.it.

Finanziato dall'Unione europea NextGenerationEU
Italiadomani PIANO NAZIONALE DI RIPRESA E RESILIENZA
agritech

ABSTRACT

Exosomes are nanoscale extracellular vesicles that carry molecular signatures reflective of their cells of origin, making them attractive biomarkers for liquid biopsy applications. In this study, we present a rapid and highly specific colorimetric aptasensor for the detection of Gremlin 1 (GREM-1)-expressing exosomes in serum. The sensing strategy relies on the disaggregation of gold nanoparticle (AuNP) clusters, initially formed by NaCl-induced aggregation, upon selective binding of the target. AuNPs were functionalized with a thiolated Ex.50.T aptamer specifically recognizing exosomal GREM-1, and the binding event triggers a measurable spectral shift in the plasmonic profile. A detection limit below 10^6 exosomes/mL was achieved using serial dilutions of purified exosomes isolated from breast cancer serum samples, demonstrating the method's sensitivity and robustness under controlled conditions. Applied to 100 clinical serum samples, the assay demonstrated excellent diagnostic performance, with 84% sensitivity and 90% specificity—values comparable to those of mammography—without requiring extensive sample processing. Comparative analysis with commercial ELISA and Ex.50.T aptamer-based ELONA confirmed the superior discriminatory power of the method proposed here. Transmission electron microscopy further corroborated the mechanism by revealing exosomes physically disrupting AuNP aggregates. These results highlight the diagnostic potential of exosome-focused sensing strategies and establish this aptamer-based colorimetric platform as a promising candidate for non-invasive screening of breast cancer through liquid biopsy.

Keywords: Aptasensor, colorimetric sensor, liquid biopsy, exosome detection, gold nanoparticles (AuNPs), anti-aggregation assay.

1. Introduction

Breast cancer (BC) remains the most commonly diagnosed cancer and the leading cause of cancer-related death among women worldwide, with an estimated 2.3 million new cases and 670,000 deaths in 2022 [1]. Its burden is particularly severe in low- and middle-income countries, where mortality-to-incidence ratios often exceed 50% due to limited access to early diagnosis and effective treatments[2]. Mammography is currently regarded as the gold standard for BC screening due to its widespread clinical adoption. However, it has notable limitations, including reduced sensitivity in women with dense breast tissue [3], exposure to ionizing radiation, and the need for painful breast compression. These drawbacks, along with infrastructure and personnel requirements, limit its accessibility and effectiveness, particularly in younger women and underserved populations. Moreover, the sensitivity and specificity of the various mammographic techniques exhibit considerable variability, with sensitivity values ranging from 55% to 91%, and specificity ranging from 84% to 97% [4].

Among the alternative strategies being explored to improve BC screening, liquid biopsy has emerged as a particularly promising approach [5]. However, it faces two major challenges: the identification of suitable biomarkers and the development of detection methods that are both reliable and cost-effective. In this context, exosomes are gaining significant attention as potential biomarkers due to their molecular content, which reflects the physiological and pathological state of their cells of origin [6,7]. Exosomes are EVs (extracellular vesicles) with a diameter ranging from 30 to 150 nm, playing a critical role in intercellular communication and disease progression. They have been widely studied as potential biomarkers for early cancer detection due to their presence in various biological fluids and their cargo of proteins, lipids, and nucleic acids [8–10].

Among these, exosome surface proteins have gained attention as key targets for biosensing applications [11–13].

Several biosensors and analytical techniques have been developed for detecting exosomes, each offering distinct advantages and limitations. Enzyme-Linked Immunosorbent Assay (ELISA) remains one of the most widely used methods due to its high specificity and sensitivity [14,15]. However, it requires multiple processing steps, expensive reagents, and long incubation times, which can limit its practicality in rapid diagnostic settings [16]. Surface Plasmon Resonance (SPR) provides a label-free optical detection platform that allows real-time monitoring of biomolecular interactions. Despite its high sensitivity, SPR requires sophisticated instrumentation and specialized expertise, making it less accessible for routine diagnostics [17,18]. Another category of biosensors includes electrochemical approaches, which detect changes in electrical signals upon the binding of a target. These systems are often portable, cost-effective, and suitable for point-of-care applications, although surface modifications and environmental factors can influence their sensitivity [19–21]. Fluorescence-based assays, which utilize fluorescently labeled antibodies or aptamers, enable sensitive detection of exosomes in biological samples. However, they are susceptible to photobleaching and background fluorescence interference, which may impact the accuracy of results in complex biological matrices [22,23]. Mass spectrometry (MS) is another powerful analytical tool for protein characterization and quantification. While it provides high sensitivity and specificity, its application in routine diagnostics is hindered by the need for expensive instrumentation and extensive sample preparation [24,25].

In contrast, colorimetric biosensors based on gold nanoparticles (AuNPs) offer a simple and effective alternative for detecting target analytes [26–28]- However, their often-limited sensitivity requires the implementation of aggregation-based strategies to improve detection performance.

Scheme 1. Anti-aggregation method

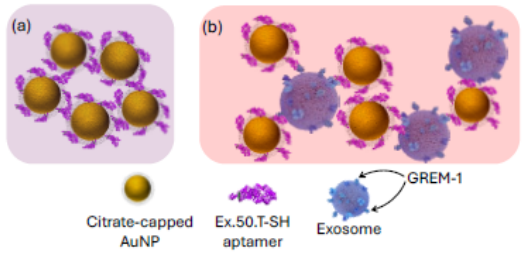

Scheme 1. (a) Gold nanoparticles (AuNPs) are aggregated by the controlled addition of NaCl, forming a relatively stable reagent. (b) Upon exposure to serum containing GREM1-expressing exosomes, specific Ex.50.T-SH aptamer–target interactions promote nanoparticle disaggregation, resulting in a measurable change in the extinction spectrum.

This is the case for the so-called anti-aggregation method (Scheme 1), which has been traditionally used for detecting small analytes such as metal ions and heavy metals [29,30]. This approach is inherently label-free and relies on the initial aggregation of AuNPs followed by a controlled disaggregation event occurring when the target interacts with the system. In the case of metal ion detection, disaggregation occurs due to the electrostatic interactions between the target ion and the negatively charged citrate-stabilized AuNPs [31]. The detection of larger targets such as exosomes requires gold nanoparticles to be functionalized with a biomolecule that strongly recognizes specific surface proteins on the exosome, thereby destabilizing the initial aggregates.

In this manuscript, we describe a colorimetric biosensor based on the anti-aggregation approach, in which AuNPs were functionalized with a terminal modification of the aptamer Ex.50.T [32]. This aptamer is the short form of a single-stranded oligonucleotide developed through SELEX (Systematic Evolution of Ligands by EXponential enrichment) for high specificity and affinity toward breast cancer EVs, able to recognize the protein Gremlin-1 (GREM-1) as a target [32,33].

GREM-1 is overexpressed in exosomes derived from BC cells, making it a valuable biomarker for non-invasive diagnostic approaches [33–35]. Although Ex.50.T might bind recombinant GREM-1 in vitro, the aptamer was originally selected against intact exosomes and exhibits functional activity only when GREM-1 is present on the exosomal surface. This, together with the multivalent display of GREM-1 in serum-derived samples, strongly suggests that Ex.50.T effectively binds exosomal GREM-1 in complex biological fluids. Moreover, its strong target-binding capacity and high stability made it an ideal tool for exosome detection.

For the purpose of this work, Ex.50.T was modified with a thiol (-SH) terminal modification, allowing covalent attachment to gold nanoparticles, ensuring stable functionalization for biosensing applications. Thus, we will refer to the resulting sequence as Ex.50.T-SH. The specific binding of Ex.50.T-SH to GREM-1 resulted in a measurable spectral shift of the resonance in the extinction spectra, which strongly correlated with exosome concentration. Applied to 1:1 diluted serum samples, the biosensor achieved a sensitivity of 84% and a specificity of 90%, matching the diagnostic performance typically associated with mammography [4]. Since the single test requires minimal sample preparation followed by a rapid analysis, the biosensor proposed here lends itself not only to large-scale population screening but also to deployment in low-resource settings. Furthermore, due to its high sensitivity and specificity, this method is suitable for younger women, for whom traditional imaging, such as mammography, is inappropriate.

2. Materials and methods

2.1 Reagents and materials

Gold nanoparticles (AuNPs) with an average diameter of ~30 nm were synthesized using the citrate reduction method (Turkevich method) [36]. The aptamer Ex.50.T-SH, designed to specifically bind to the exosomes, was synthesized with a thiol (-SH) terminal modification to enable covalent

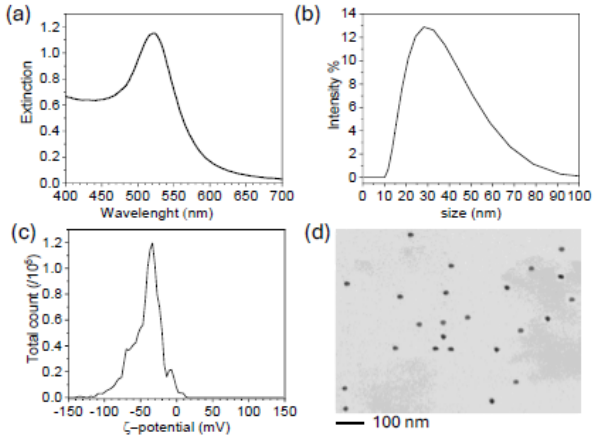

Figure 1. (a) Extinction spectrum of the synthesized AuNPs, showing a well-defined plasmon resonance peak centered at 522 nm, indicative of monodispersity and colloidal stability. (b) Dynamic Light Scattering (DLS) analysis confirms a narrow size distribution with an average hydrodynamic diameter of approximately 30 nm. (c) ζ-potential measurements reveal a surface charge of –50 mV, indicating strong electrostatic repulsion and high colloidal stability. (d) transmission Electron Microscopy (TEM) micrographs further confirm the spherical morphology and uniform size distribution of the gold nanoparticles.

attachment to the AuNP surface (Bio-Fab research s.r.l.) [37]. The aptamer was previously characterized through (Enzyme-Linked Oligonucleotide Assay) ELONA [33], and surface plasmon resonance (SPR), showing a dissociation constant (K_d) of approximately 37.7 nM for GREM-1, confirming its strong binding affinity. Other chemicals, including sodium chloride (NaCl, 1M), tris(2-carboxyethyl)phosphine (TCEP, 100 mM), and phosphate-buffered saline (PBS), were obtained from Merck group and used as received.

2.2 Synthesis of Gold Nanoparticles

The AuNPs were synthesized by boiling an aqueous solution of $HAuCl_4$ (1 mM), purchased by Merck group, and rapidly adding sodium citrate (38.8 mM) under vigorous stirring. The color

change from pale yellow to deep red indicated the formation of stable AuNPs. The particles were then extensively characterized to confirm their optical, dimensional, and surface properties. UV-Vis spectroscopy was employed to monitor the localized surface plasmon resonance (LSPR) peak (Figure 1a), confirming the expected spectral profile of well-dispersed gold nanoparticles. Dynamic Light Scattering (DLS) analysis provided quantitative measurements of the hydrodynamic diameter (Figure 1b), supporting the uniformity of particle size distribution.

Additionally, ζ-potential analysis confirmed the colloidal stability of the nanoparticles by measuring their surface charge (Figure 1c). To further validate their morphology, Transmission Electron Microscopy (TEM) images were acquired by depositing the AuNPs on a gold sheet with very low roughness, so that a high-contrast image could be achieved. Figure 1d confirms that the AuNP size distribution is quite narrow with an average value for the diameter of ≈ 25 nm. The TEM micrograph images clearly confirmed both the spherical shape and consistent size of the synthesized particles.

2.3 Functionalization of Gold Nanoparticles

The functionalization of AuNPs with the Ex.50.T.SH aptamer was carried out by reducing the thiol-protected aptamer using TCEP. Specifically, 10 mL of aptamer solution (2.5 µg/mL) was incubated with 10 µL of 100 mM TCEP for 1 hour to remove the thiol protecting group. The reduced aptamer was then mixed 1:1 (v:v) with AuNPs (optical density OD = 4) and incubated under gentle stirring for 30 minutes at room temperature to promote stable attachment. The initial deprotected aptamer solution (2.5 µg/mL) was subsequently diluted to identify the optimal functionalization conditions. The corresponding kinetic curve—obtained by monitoring the plasmonic peak shift associated with aptamer binding to the AuNP surface—is shown in Figure

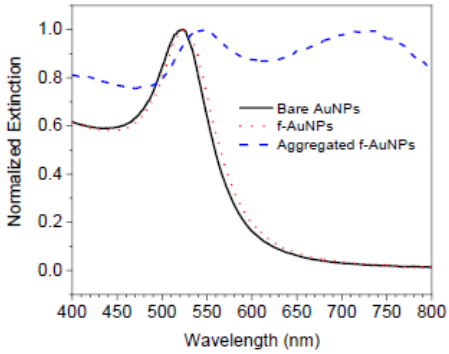

Figure 2. Normalized extinction spectra illustrating the formation of the sensing reagent. The black line shows the spectrum of citrate-stabilized gold nanoparticles (AuNPs) in ultrapure water. Functionalization with thiolated aptamers (red dotted line) induces a red shift of approximately 1.9 nm, consistent with surface modification. Addition of NaCl (blue dashed line) triggers nanoparticle aggregation, leading to a broad extinction profile characteristic of the final reagent used in the anti-aggregation assay.

S1. A saturation value of approximately 2 nm is reached when the aptamer concentration is around 2 µg/mL.

Importantly, this saturation reflects the completion of the adsorption process under the chosen experimental conditions and does not correspond to full monolayer coverage. According to the effective-medium approximation [38,39], a partially coated AuNP can be modelled as a homogeneous dielectric shell whose refractive index is

$$n_{\mathrm{eff}}(f) = n_{\mathrm{w}} + f(n_{\mathrm{DNA}} - n_{\mathrm{w}}), \quad (1)$$

where f is the fractional surface coverage, n_{w}=1.33 is the refractive index of water, and n_{DNA}≈1.46 represents that of the DNA layer [40]. In this regime, the LSPR shift is proportional to the effective index change through the refractive-index sensitivity S of the nanoparticle. For spherical AuNPs

in the 20–40 nm range, consistent with the particles used here, the reported sensitivity is 60–100 nm/RIU [41]. Taking a representative value $S \approx 80$ nm/RIU, the measured shift of 2 nm corresponds to an effective index increase $\Delta n_{\mathrm{eff}} \approx 0.025$, i.e. ≈20% of the full index contrast $\Delta n = (n_{\mathrm{DNA}} - n_{\mathrm{w}}) = 0.13$. This yields a surface-coverage estimate $f \approx 0.2$.

To estimate the number of aptamers per particle, we used the experimentally reported footprint (A_{DNA}) of thiolated ssDNA on 30-nm AuNPs ($A_{\mathrm{DNA}} \approx 11$ nm² per ssDNA molecule) [42], which leads to the maximum loading capacity $N_{\mathrm{max}} = 4\pi R^2 / A_{\mathrm{DNA}} \approx 260$ aptamers. With $f \approx 0.2$, the actual number of Ex.50.T molecules immobilized under our conditions is $N \approx 50$ aptamers per nanoparticle. This sparse but stable functionalization provides adequate probe density for target recognition while maintaining the reversible aggregation–disaggregation behavior that underpins the colorimetric response.

2.4 Preparation of the aggregated sensing reagent

The progressive changes in the extinction spectrum during reagent preparation are shown in Figure 2. The spectrum of bare AuNPs in water (black curve) features the expected plasmonic peak at ~520 nm. As reported in the previous section 2.3, following aptamer functionalization, a slight red shift (2 nm) is observed (red dotted curve), consistent with surface modification without loss of colloidal stability. The subsequent addition of 10 mM NaCl promotes controlled interparticle aggregation (blue dashed curve), evidenced by peak broadening and increased extinction at longer wavelengths. This pre-aggregated state constitutes the sensing reagent used in all detection experiments.

2.5 TEM Sample Preparation and Imaging

To ascertain the occurrence of the salt-induced AuNPs aggregation Transmission Electron Microscopy (TEM) analyses were performed. A careful sample preparation protocol was followed

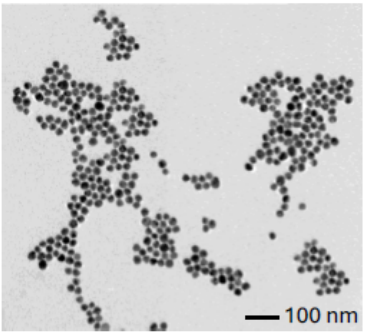

Figure 3. Transmission Electron Microscopy (TEM) image showing the formation of gold nanoparticle aggregates resulting from the addition of NaCl.

to ensure high-quality imaging and reliable structural characterization. Gold nanoparticles were first synthesized and functionalized with aptamers designed to specifically interact with exosomes. For control samples, the functionalized AuNPs were incubated with sodium chloride (NaCl) in the absence of exosomes, to induce aggregation through charge screening. In contrast, to investigate the disaggregation effect, other samples were first incubated with exosome-containing solutions to allow aptamer-exosome binding, followed by NaCl addition. To preserve the structural integrity of the resulting aggregates or disaggregated particles, samples were fixed with 2.5% glutaraldehyde in sodium cacodylate buffer and post-fixed with osmium tetroxide. A small volume of each sample was deposited onto carbon-coated TEM grids, negatively stained with 2% uranyl acetate, and examined using a FEI Tecnai 12 transmission electron microscope (120 kV, FEI Company, The Netherlands). A representative TEM micrograph is shown in Figure 3, illustrating the large and well-defined AuNP clusters formed in the absence of exosomes.

3. Results and Discussion

3.1 Interaction between GREM-1 and aptamer-functionalized AuNPs

To verify the interaction between recombinant GREM-1 and the aptamer-functionalized AuNPs, a preliminary test was performed using an aggregation-based strategy. In this setup, increasing concentrations of GREM-1 in 1X PBS were added to the f-AuNPs dispersed in ultrapure water, without salt. As shown in Figure S2a, the extinction spectra show a red shift and a gradual increase in the integrated area between 530–800 nm, consistent with a GREM-1-induced nanoparticle aggregation. This interaction was analyzed using the integrated area (Figure S2b), yielding a minimum detectable concentration of approximately 10 ng/mL. Although this aggregation-based configuration differs from the anti-aggregation strategy employed in the actual biosensing assay, it confirms the ability of the aptamer to bind GREM-1. It is worth noticing that — although measured with the aggregation method — the LOD for free GREM-1 is relatively high compared to the level expected in serum, which is lower than 2.0 ng/mL in healthy people and approximately 14-15 ng/mL in patients with Idiopathic Pulmonary Fibrosis [43]. Moreover, by using commercial ELISA, we also measured the concentration of GREM-1 in non-tumoral and tumoral (BC) serum samples and found that such a value never exceeded 2.0 ng/mL (see Figure S3a). Even more important, ELISA analysis revealed no statistically significant difference in free GREM-1 levels between tumoral and non-tumoral serum. We attribute the disaggregation mechanism primarily to affinity competition: the aptamer preferentially binds GREM-1 on the exosomal surface, thereby disengaging from non-specific interparticle interactions and leading to nanoparticle dispersion.

3.2 Interaction between GREM-1 and purified exosomes

Having confirmed the aptamer's ability to recognize GREM-1, we next implemented the complete anti-aggregation sensing strategy using purified EVs isolated from breast cancer serum samples.

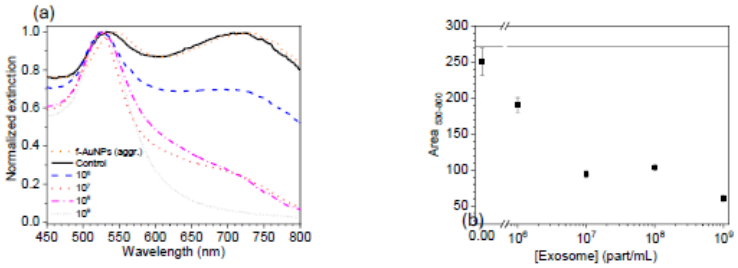

Figure 4. (a) Extinction spectra at different exosome concentration normalized at the height of the first peak whose position is at approximately 520 nm. Blank corresponds to the null concentration that provides a spectrum with a high contribution of aggregates. In fact, the disaggregation induced by the exosomes is clearly visible in the decrease of the area in the range 530-800 nm as a function of the exosome concentration. (b) Area in the range 530–800 nm versus purified exosome concentration. The error bars come from the measurements carried out in duplicate. The horizontal line corresponds to the area of the signal from the aggregated f-AuNP (dotted red line in the panel (a)).

The initial EV concentration was quantified by nanoparticle tracking analysis (NTA) (Figure S4). For each measurement, serial dilutions of EVs suspended in 1× PBS were prepared and mixed (1:1, v/v) with an equal volume of pre-aggregated f-AuNPs dispersed in ultrapure Milli-Q water, resulting in a final reaction medium composed of 50% PBS and 50% water. The extinction spectra obtained at different EV concentrations are shown in Figure 4a. All spectra were normalized to the intensity of the primary plasmonic peak located at approximately 530 nm to allow for comparison of their shape across the 530–800 nm range. A clear reduction in spectral intensity at longer wavelengths was observed as the exosome concentration increased, consistent with the disaggregation of salt-induced nanoparticle clusters triggered by target binding. This behavior was quantified by calculating the integrated area in the 530–800 nm range of the normalized spectra (Figure 4b), yielding a well-defined dose–response curve. The horizontal reference line in the graph corresponds to the area measured for f-AuNPs in ultrapure water, which closely matches the zero-concentration condition in PBS, confirming that the buffer does not contribute to nonspecific

aggregation. The limit of detection was determined using the standard signal-to-noise criterion (S/N = 3), where the signal corresponds to the spectral response and the noise is defined as the standard deviation of the control (Figure 4b). Under these conditions, the LOD was estimated to be approximately 10^6 EVs/mL, confirming the sensitivity and analytical reliability of the anti-aggregation assay in purified systems.

3.3 Assay performance in real samples

To assess performance in complex biological matrices, the assay was applied to 100 clinical serum samples (50 from breast cancer patients and 50 from healthy donors), diluted 1:1 with Milli-Q water. Unlike purified systems, human serum exhibits significant intrinsic absorbance that varies across individuals. To address this, the extinction spectrum was acquired before and after the addition of the f-AuNP reagent, and a background subtraction procedure was implemented to isolate the nanoparticle response. Furthermore, spectra were normalized to enable direct comparison across samples. Despite the increased optical complexity, a clear distinction between tumoral and non-tumoral samples could be observed, confirming the assay's applicability to real-world clinical specimens. In fact, as shown in Figure 5a, the extinction spectra recorded after incubation with pre-aggregated f-AuNPs displayed significant differences between the two groups. Tumoral samples exhibited a marked drop in absorbance near 600 nm, consistent with nanoparticle disaggregation due to the presence of GREM-1-positive exosomes. Non-tumoral samples retained the typical aggregated plasmonic signature, indicating minimal interaction. It is worth noting that the clear and statistically significant separation between the two groups observed with our aptamer-based biosensor (Figure 5a) is not present when the same samples are analysed using ELISA targeting free GREM-1 (Figure S3a). We can therefore confidently exclude a significant contribution of free GREM-1 to the optical signal observed in serum assays.

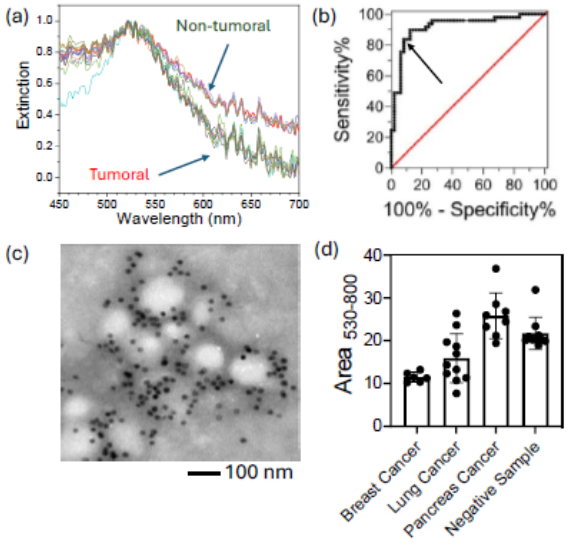

Figure 5. (a) Extinction spectra of serum samples from breast cancer patients (tumoral) and healthy donors (non-tumoral), showing pronounced differences around 600 nm, indicative of nanoparticle disaggregation driven by exosome interaction. (b) Receiver Operating Characteristic (ROC) curve based on spectral area analysis. The optimal diagnostic threshold is indicated by the arrow and yields a sensitivity of 84% and a specificity of 90%. (c) Transmission electron microscopy (TEM) image of the nanoparticle–exosome system. The comparison with the micrograph reported in Figure 3 shows the exosomes that scatter the nanoparticle aggregates, directly supporting the proposed mechanism of target-induced disaggregation. (d) Cross-reactivity test with serum from patients affected by other cancers. Minimal signal was observed for pancreatic cancer and negative controls, while a partial response was seen in non-small cell lung cancer samples. Each group included 10 independent serum samples.

Spectral data were integrated over the 530–800 nm range and used to build a Receiver Operating Characteristic (ROC) curve (Figure 5b). The Area Under the ROC Curve (AUC) was 0.92 (95% Confidence Interval: 0.86–0.98), indicating excellent diagnostic performance and robustness of the assay. The analysis of the ROC yielded a sensitivity of 84% and a specificity of 90%, with an

optimal diagnostic threshold corresponding to a value of the area in the range 530–800 nm equal to 18.

Further structural insight into the disaggregation mechanism was obtained through transmission electron microscopy (Figure 5c). Compared to the compact aggregates observed in the absence of the target (Figure 3), the presence of exosomes results in visibly disrupted nanoparticle assemblies. The micrograph clearly shows exosomes inserted within and physically separating the gold nanoparticle clusters, thereby destabilizing their structure. This direct morphological evidence corroborates the proposed model of target-induced disaggregation driven by aptamer-mediated exosome recognition. We attribute the disaggregation mechanism primarily to affinity competition: the aptamer preferentially binds GREM-1 on the exosomal surface, thereby disengaging from non-specific interparticle interactions and leading to nanoparticle dispersion.

We point out that the assay was performed directly in human serum with only a 1:1 dilution in PBS, thus preserving the complexity of the biological matrix. Under these conditions, the sensor exhibited a robust and reproducible signal, indicating good tolerance to potential interfering components such as proteins, lipids, or salts present in serum. Moreover, it is worth noting that all experiments were conducted using nanoparticles synthesized on different days and in independent batches. The reproducibility of the calibration curves and consistent diagnostic accuracy across the dataset support the robustness of the system against batch-to-batch variation.

3.4 Assay specificity

To further explore assay specificity, serum samples from patients affected by non-small cell lung cancer (NSCL) and pancreatic cancer were analyzed (Figure 5d). While samples from pancreatic cancer patients and healthy donors yielded negligible responses, a partial signal was observed in the presence of NSCLC–derived vesicles. This result suggests limited cross-reactivity, potentially

due to the expression of shared surface epitopes. Such a finding is consistent with the known expression profile of GREM-1, which is associated with breast and NSCLC cancers but not reported prominently expressed in pancreatic-derived EVs [33,34,44]. Statistical analysis confirmed the selectivity of the assay ($p < 0.05$), supporting the conclusion that disaggregation is driven by a specific interaction between the Ex.50.T-SH aptamer and GREM-1-expressing exosomes. The targeted nature of the aptamer-based interaction enables not only the detection of exosomes, but also their molecular profiling—an essential feature for cancer diagnostics.

To benchmark the performance of our exosome-targeted colorimetric assay, we compared it with two conventional approaches: a commercially available ELISA (Figure S3a) and an aptamer-based ELONA (Figure S3b). The analysis was conducted on a subset of 36 serum samples, including 24 breast cancer patients and 12 non-tumoral controls. The ELISA designed to detect total GREM-1 protein in whole serum failed to discriminate between tumoral and non-tumoral groups ($p=0.2203$). In contrast, although statistically significant ($p=0.0133$), the variation observed with the aptamer-based ELONA was modest, suggesting only limited sensitivity. These results highlight a key advantage of our approach: by targeting GREM1-expressing EVs rather than total serum protein, the assay achieves higher analytical performance. The selective recognition of vesicle-associated GREM-1 accounts for the superior discrimination observed with our method, underscoring the diagnostic value of focusing on exosomal markers in complex biological fluids.

4. Conclusions

In this work, we developed and validated a novel colorimetric biosensor based on an anti-aggregation strategy utilizing gold nanoparticles functionalized with the thiolated aptamer Ex.50.T-SH, designed for the detection of (GREM-1)-positive exosomes in human serum. The method is characterized by simplicity, rapidity, and high reproducibility, offering significant

advantages over conventional detection platforms such as ELISA and ELONA. The specific interaction between the Ex.50.T-SH aptamer and EVs GREM-1 enabled sensitive detection both in purified environments and in complex biological matrices, including minimally diluted clinical serum samples. The assay operates in a mix-and-measure format, requiring only a single dilution step and no specialized equipment, making it particularly suited for decentralized diagnostics.

A key strength of the developed platform lies in its ability to function effectively in 1:1 (v/v) diluted serum, overcoming the fouling issues that typically hinder the performance of nanoparticle-based biosensors in biological fluids. This represents a significant methodological advancement, as alternative approaches often require dilution factors as high as 1:1000, compromising analytical sensitivity. Although the biosensor showed low responsiveness to the free GREM-1 protein, it proved highly sensitive to the exosome-bound form, achieving a detection limit of 10^6 exosomes/mL (isolated EV). More importantly, in real serum samples, the system exhibited robust on-off behavior, allowing for a clear distinction between healthy and breast cancer-derived exosomes. A total of 100 clinical samples were analyzed, yielding excellent diagnostic performance, with a sensitivity of 84% and specificity of 90%, as validated by ROC curve analysis. The system was also shown to selectively respond to exosomes derived from cancers expressing GREM-1 (breast and possibly lung), while showing no significant response to exosomes from pancreatic cancer, thus confirming the assay's biomarker specificity.

Microscopy analyses (TEM) further corroborated the spectroscopic findings, revealing morphological changes in gold nanoparticle aggregates upon exosome binding, thereby supporting the proposed sensing mechanism. Taken together, these findings highlight the potential of this anti-aggregation aptamer-based biosensor for the development of non-invasive, point-of-care diagnostic tools. Its performance, ease of use, and ability to discriminate among exosomal

populations based on biomarker expression open new perspectives for liquid biopsy applications in precision oncology. Future efforts will aim to integrate this sensing platform into microfluidic systems to enable high-throughput analysis, as well as to expand its diagnostic scope through the inclusion of additional aptamers targeting alternative exosomal biomarkers.

CRediT authorship contribution statement

Bartolomeo Della Ventura: Conceptualization, Methodology, Formal analysis, Investigation, Writing-original draft preparation, Funding acquisition. **Cristina Quintavalle**: Conceptualization, Methodology, Formal analysis, Data curation, Visualization resources. **Erica Cavaliere**: Methodology, Investigation, Data curation, Writing-original draft preparation, Visualization. **Kristin Tkalčec**: Investigation, Data curation, Visualization. **Paolo Aniello**: formal analysis. **Vincenzo Iannotti**: Formal analysis, Writing-review and editing, Project administration. **Gerolama Condorelli**: Writing-review and editing, Resources, Supervision, Project administration, Funding acquisition. **Raffaele Velotta**: Formal analysis, Writing-review and editing, Supervision, Project administration, Funding acquisition.

Declaration of Competing Interest

G. Condorelli and C. Quintavalle disclose being inventors of the following patent: ANTICANCER APTAMERS AND USES THEREOF PCT/EP2021/066448 (National Research Council-CNR). The other authors declare no competing interests.

Acknowledgements

We acknowledge the financial support from the Italian Ministry of University and Research (MUR) under the following grants: PRIN projects P2022J3ZPW, 2022WFRAE7 and P2022 F3ZKJF. Additional funding was also provided by the European Union through Next Generation

EU, Mission 4 Component 2 (Project CUP E63C22000920005), PNRR-MUR NextGenerationEU cod. CN00000041, and Horizon Europe Project MSCA-DN CanDoIt (ID 101120186).

Appendix A. Supplementary data

Supplementary data for this article can be found online.

Data availability

Data will be made available on request.

Ethics approval and consent to participate

Samples were collected according to the Declaration of Helsinki, and each subject signed an informed consent before participating in the study. The study was approved by the Research Ethics Committee of the AUO-University of Naples Federico II n° 119/15ES1.

REFERENCES

[1] J. Kim, A. Harper, V. McCormack, H. Sung, N. Houssami, E. Morgan, M. Mutebi, G. Garvey, I. Soerjomataram, M.M. Fidler-Benaoudia, Global patterns and trends in breast cancer incidence and mortality across 185 countries, Nat Med 31 (2025) 1154–1162. https://doi.org/10.1038/s41591-025-03502-3.

[2] N.Q. Agussalim, M. Ahmad, P. Prihantono, A.N. Usman, S. Rafiah, D.I. Agustin, Physical activity and quality of life in breast cancer survivors, Breast Dis 43 (2024) 161–171. https://doi.org/10.3233/BD-249005.

[3] N.R. Payne, S.E. Hickman, R. Black, A.N. Priest, S. Hudson, F.J. Gilbert, Breast density effect on the sensitivity of digital screening mammography in a UK cohort, Eur Radiol 35 (2025) 177–187. https://doi.org/10.1007/s00330-024-10951-w.

[4] J. Shi, J. Li, Y. Gao, W. Chen, L. Zhao, N. Li, J. Tian, Z. Li, The screening value of mammography for breast cancer: an overview of 28 systematic reviews with evidence mapping, J Cancer Res Clin Oncol 151 (2025) 102. https://doi.org/10.1007/s00432-025-06122-z.

[5] J. Gooding, The Liquid Biopsy, ACS Sens 10 (2025) 3192–3193. https://doi.org/10.1021/acssensors.5c01389.

[6] S.H. Jalalian, M. Ramezani, S.A. Jalalian, K. Abnous, S.M. Taghdisi, Exosomes, new biomarkers in early cancer detection, Anal Biochem 571 (2019) 1–13. https://doi.org/10.1016/j.ab.2019.02.013.

[7] R. Uyar, G. Özçelikay-Akyıldız, S.İ. Kaya, S. Bereketoğlu Nergis, Ö. Beşbinar, M.A. Ünal, A. Yilmazer, S.A. Özkan, Early cancer detection based on exosome biosensors in biological samples, Sens Actuators B Chem 400 (2024) 134886. https://doi.org/10.1016/j.snb.2023.134886.

[8] S.H. Jalalian, M. Ramezani, S.A. Jalalian, K. Abnous, S.M. Taghdisi, Exosomes, new biomarkers in early cancer detection, Anal Biochem 571 (2019) 1–13. https://doi.org/10.1016/j.ab.2019.02.013.

[9] R. Tenchov, A.K. Sapra, J. Sasso, K. Ralhan, A. Tummala, N. Azoulay, Q.A. Zhou, Biomarkers for Early Cancer Detection: A Landscape View of Recent Advancements, Spotlighting Pancreatic and Liver Cancers, ACS Pharmacol Transl Sci 7 (2024) 586–613. https://doi.org/10.1021/acsptsci.3c00346.

[10] S. Das, M.K. Dey, R. Devireddy, M.R. Gartia, Biomarkers in Cancer Detection, Diagnosis, and Prognosis., Sensors (Basel) 24 (2023) 37. https://doi.org/10.3390/s24010037.

[11] F.Z. Farhana, M. Umer, A. Saeed, A.S. Pannu, M. Shahbazi, A. Jabur, H.J. Nam, K. Ostrikov, P. Sonar, S.H. Firoz, M.J.A. Shiddiky, Isolation and Detection of Exosomes Using Fe2O3Nanoparticles, ACS Appl Nano Mater 4 (2021) 1175–1186. https://doi.org/10.1021/acsanm.0c02807.

[12] Y. Wu, Z. Wu, W. Xu, R. Zeng, J. Weng, L. Sun, A label-free colorimetric biosensor utilizing natural material for highly sensitive exosome detection, Talanta 275 (2024) 126182. https://doi.org/10.1016/j.talanta.2024.126182.

[13] W. Zhang, Z. Tian, S. Yang, J. Rich, S. Zhao, M. Klingeborn, P.-H. Huang, Z. Li, A. Stout, Q. Murphy, E. Patz, S. Zhang, G. Liu, T.J. Huang, Electrochemical micro-aptasensors for exosome detection based on hybridization chain reaction amplification, Microsyst Nanoeng 7 (2021) 63. https://doi.org/10.1038/s41378-021-00293-8.

[14] M. Logozzi, R. Di Raimo, D. Mizzoni, S. Fais, Immunocapture-based ELISA to characterize and quantify exosomes in both cell culture supernatants and body fluids, Methods Enzymol 645 (2020) 155–180. https://doi.org/10.1016/bs.mie.2020.06.011.

[15] T.A.P. Driedonks, L. Jiang, O. Gololobova, Z. Liao, K.W. Witwer, ELISA-based detection of immunoglobulins against extracellular vesicles in blood plasma, Journal of Extracellular Biology 3 (2024) e129. https://doi.org/10.1002/jex2.129.

[16] R. Rodpai, L. Sadaow, P. Boonroumkaew, W. Phupiewkham, T. Thanchomnang, Y. Limpanont, P. Chusongsang, O. Sanpool, H. Ohmae, H. Yamasaki, P.M. Intapan, W. Maleewong, Comparison of point-of-care test and enzyme-linked immunosorbent assay for detection of immunoglobulin G antibodies in the diagnosis of human schistosomiasis japonica, International Journal of Infectious Diseases 107 (2021) 47–52. https://doi.org/10.1016/j.ijid.2021.04.039.

[17] Y. Yang, C. Zhai, Q. Zeng, A.L. Khan, H. Yu, Multifunctional Detection of Extracellular Vesicles with Surface Plasmon Resonance Microscopy, Anal Chem 92 (2020) 4884–4890. https://doi.org/10.1021/acs.analchem.9b04622.

[18] C. Liu, X. Zeng, Z. An, Y. Yang, M. Eisenbaum, X. Gu, J.M. Jornet, G.K. Dy, M.E. Reid, Q. Gan, Y. Wu, Sensitive Detection of Exosomal Proteins via a Compact Surface Plasmon Resonance Biosensor for Cancer Diagnosis, ACS Sens 3 (2018) 1471–1479. https://doi.org/10.1021/acssensors.8b00230.

[19] J. Su, S. Chen, Y. Dou, Z. Zhao, X. Jia, X. Ding, S. Song, Smartphone-Based Electrochemical Biosensors for Directly Detecting Serum-Derived Exosomes and Monitoring Their Secretion, Anal Chem 94 (2022) 3235–3244. https://doi.org/10.1021/acs.analchem.1c04910.

[20] Y. Guo, S. Liu, H. Yang, P. Wang, Q. Feng, Regenerable electrochemical biosensor for exosomes detection based on the dual-recognition proximity binding-induced DNA walker, Sens Actuators B Chem 349 (2021) 130765. https://doi.org/10.1016/j.snb.2021.130765.

[21] E. Dezhakam, B. Khalilzadeh, M. Mahdipour, I. Isildak, H. Yousefi, M. Ahmadi, A. Naseri, R. Rahbarghazi, Electrochemical biosensors in exosome analysis; a short journey to the present and future trends in early-stage evaluation of cancers, Biosens Bioelectron 222 (2023) 114980. https://doi.org/10.1016/j.bios.2022.114980.

[22] Y. Wu, Z. Gao, Y. Chai, A. Zhang, S. He, X. Liu, H. Yuan, L. Tan, L. Ding, Y. Wu, One-step and label-free ratiometric fluorescence assay for the detection of plasma exosome towards cancer diagnosis, Talanta 271 (2024) 125700. https://doi.org/10.1016/j.talanta.2024.125700.

[23] X. Wang, H. Shang, C. Ma, L. Chen, A Fluorescence Assay for Exosome Detection Based on Bivalent Cholesterol Anchor Triggered Target Conversion and Enzyme-Free Signal Amplification, Anal Chem 93 (2021) 8493–8500. https://doi.org/10.1021/acs.analchem.1c00796.

[24] Y. Zhu, H. Pick, N. Gasilova, X. Li, T.E. Lin, H.P. Laeubli, A. Zippelius, P.C. Ho, H.H. Girault, MALDI Detection of Exosomes: A Potential Tool for Cancer Studies, Chem 5 (2019) 1318–1336. https://doi.org/10.1016/j.chempr.2019.04.007.

[25] B.A. Brown, X. Zeng, A.R. Todd, L.F. Barnes, J.M.A. Winstone, J.C. Trinidad, M. V. Novotny, M.F. Jarrold, D.E. Clemmer, Charge Detection Mass Spectrometry Measurements of Exosomes and other Extracellular Particles Enriched from Bovine Milk, Anal Chem 92 (2020) 3285–3292. https://doi.org/10.1021/acs.analchem.9b05173.

[26] A. Minopoli, N. Sakač, B. Lenyk, R. Campanile, D. Mayer, A. Offenhäusser, R. Velotta, B. Della Ventura, LSPR-based colorimetric immunosensor for rapid and sensitive 17β-estradiol detection in tap water, Sens Actuators B Chem 308 (2020) 127699. https://doi.org/10.1016/j.snb.2020.127699.

[27] B. Della Ventura, M. Cennamo, A. Minopoli, R. Campanile, S. Bolletti Censi, D. Terracciano, G. Portella, R. Velotta, Colorimetric Test for Fast Detection of SARS-CoV-2 in Nasal and Throat Swabs, ACS Sens 5 (2020) 3043–3048. https://doi.org/10.1021/acssensors.0c01742.

[28] M. Iarossi, C. Schiattarella, I. Rea, L. De Stefano, R. Fittipaldi, A. Vecchione, R. Velotta, B. Della Ventura, Colorimetric Immunosensor by Aggregation of Photochemically Functionalized Gold Nanoparticles, ACS Omega 3 (2018) 3805–3812. https://doi.org/10.1021/acsomega.8b00265.

[29] F. Najafzadeh, F. Ghasemi, M.R. Hormozi-Nezhad, Anti-aggregation of gold nanoparticles for metal ion discrimination: A promising strategy to design colorimetric sensor arrays, Sens Actuators B Chem 270 (2018) 545–551. https://doi.org/10.1016/j.snb.2018.05.065.

[30] R. Kataria, K. Sethuraman, D. Vashisht, A. Vashisht, S.K. Mehta, A. Gupta, Colorimetric detection of mercury ions based on anti-aggregation of gold nanoparticles using 3, 5-dimethyl-1-thiocarboxamidepyrazole, Microchemical Journal 148 (2019) 299–305. https://doi.org/10.1016/j.microc.2019.04.068.

[31] X. Shao, D. Yang, M. Wang, Q. Yue, A colorimetric detection of Hg2+ based on gold nanoparticles synthesized oxidized N-methylpyrrolidone as a reducing agent, Sci Rep 13 (2023) 1–8. https://doi.org/10.1038/s41598-023-49551-x.

[32] C.L. Esposito, C. Quintavalle, F. Ingenito, D. Rotoli, G. Roscigno, S. Nuzzo, R. Thomas, S. Catuogno, V. de Franciscis, G. Condorelli, Identification of a novel RNA aptamer that selectively targets breast cancer exosomes, Mol Ther Nucleic Acids 23 (2021) 982–994. https://doi.org/10.1016/j.omtn.2021.01.012.

[33] C. Quintavalle, F. Ingenito, G. Roscigno, B. Pattanayak, C.L. Esposito, A. Affinito, D. Fiore, G. Petrillo, S. Nuzzo, B. Della Ventura, F. D'Aria, C. Giancola, S. Mitola, E. Grillo, M. Pirozzi, G. Donati, F.S. Di Leva, L. Marinelli, Z. Minic, F. De Micco, G. Thomas, M. V. Berezovski, G. Condorelli, Ex.50.T aptamer impairs tumor–stroma cross-talk in breast cancer by targeting gremlin-1, Cell Death Discov 11 (2025) 94. https://doi.org/10.1038/s41420-025-02363-6.

[34] N. McNamee, R. Daly, J. Crown, L. O'Driscoll, A method of separating extracellular vesicles from blood shows potential clinical translation, and reveals extracellular vesicle cargo gremlin-1 as a diagnostic biomarker, Transl Oncol 15 (2022) 101274. https://doi.org/10.1016/j.tranon.2021.101274.

[35] W. Qin, L. Wang, H. Tian, X. Wu, C. Xiao, Y. Pan, M. Fan, Y. Tai, W. Liu, Q. Zhang, Y. Yang, CAF-derived exosomes transmitted Gremlin-1 promotes cancer progression and decreases the sensitivity of hepatoma cells to sorafenib, Mol Carcinog 61 (2022) 764–775. https://doi.org/10.1002/mc.23416.

[36] J. Turkevich, P.C. Stevenson, J. Hillier, A study of the nucleation and growth processes in the synthesis of colloidal gold, Discuss Faraday Soc 11 (1951) 55–75. https://doi.org/10.1039/DF9511100055.

[37] A. Affinito, C. Quintavalle, C.L. Esposito, G. Roscigno, C. Giordano, S. Nuzzo, L. Ricci-Vitiani, I. Scognamiglio, Z. Minic, R. Pallini, M. V. Berezovski, V. de Francisis, G. Condorelli, Targeting Ephrin Receptor Tyrosine Kinase A2 with a Selective Aptamer for Glioblastoma Stem Cells, Mol Ther Nucleic Acids 20 (2020) 176–185. https://doi.org/10.1016/j.omtn.2020.02.005.

[38] K. Hasegawa, E. Porter, O. Nazarov, Analysis of homogeneous layer approximations in the modeling of localized surface plasmon resonance biosensors, Appl Opt 58 (2019) 6519. https://doi.org/10.1364/AO.58.006519.

[39] D. Foiles, K. Hasegawa, Theoretical approach for modeling LSPR biosensors for the detection of biopolymer nucleation, Appl Opt 60 (2021) 9303. https://doi.org/10.1364/AO.435364.

[40] S. Elhadj, G. Singh, R.F. Saraf, Optical Properties of an Immobilized DNA Monolayer from 255 to 700 nm, Langmuir 20 (2004) 5539–5543. https://doi.org/10.1021/la049653.

[41] Z. Bradley, D. Cunningham, N. Bhalla, Refractive Index-Modulated LSPR Sensing in 20–120 nm Gold and Silver Nanoparticles: A Simulation Study, ECS Sensors Plus 2 (2023) 043402. https://doi.org/10.1149/2754-2726/ad08d8.

[42] H.D. Hill, J.E. Millstone, M.J. Banholzer, C.A. Mirkin, The Role Radius of Curvature Plays in Thiolated Oligonucleotide Loading on Gold Nanoparticles, ACS Nano 3 (2009) 418–424. https://doi.org/10.1021/nn800726e.

[43] Y. Aoshima, Y. Enomoto, S. Muto, S. Meguro, H. Kawasaki, I. Kosugi, T. Fujisawa, N. Enomoto, N. Inui, Y. Nakamura, T. Suda, T. Iwashita, Gremlin-1 for the Differential Diagnosis of Idiopathic Pulmonary Fibrosis Versus Other Interstitial Lung Diseases: A Clinical and Pathophysiological Analysis, Lung 199 (2021) 289–298. https://doi.org/10.1007/s00408-021-00440-y.

[44] X. Wu, W. Chen, T. Fang, Z. Chen, S. Fang, C. Zhou, CAF-derived exosomes drive the FGF4/SHH feedback loop by encapsulating GREM1 in non-small cell lung cancer, Molecular Medicine 31 (2025) 281. https://doi.org/10.1186/s10020-025-01340-0.

Finanziato dall'Unione europea NextGenerationEU
Italiadomani PIANO NAZIONALE DI RIPRESA E RESILIENZA
agritech

Supplementary material

Colorimetric Aptasensor for Exosome Detection in Breast Cancer Liquid Biopsy

Bartolomeo Della Ventura[1], Cristina Quintavalle[2], Erica Cavaliere[1], Kristin Tkalče[3], Paolo Aniello[1], Vincenzo Iannotti[1,4], Gerolama Condorelli[2,3*], and Raffele Velotta[1*]

[1]Department of Physics "Ettore Pancini", University of Naples Federico II, Via Cintia 26 - 80126 Naples (Italy)

[2]CNR-Institute of Endotypes in Oncology, Metabolism and Immunology "G. Salvatore" (IEOMI), Via Sergio Pansini, 5 - 80131 Naples (Italy)

[3]Department of Molecular Medicine and Medical Biotechnology, University of Naples Federico II, Via Sergio Pansini, 5 - 80131 Naples (Italy)

[4]CNR–Institute for SuPerconductors, INnovative materials, and devices (SPIN), Via Cintia 26 - 80126 Naples (Italy)

*Corresponding authors: rvelotta@unina.it; gecondor@unina.it

Table of contents

Figure S1. Kinetic curve for aptamer-AuNP binding.

Figure S2. Interaction of free GREM-1 with f-AuNPs (extinction spectra and dose-response curve).

Figure S3. ELISA and ELONA on serum samples from non-tumoral and tumoral patients.

Figure S4. Nanoparticle Tracking Analysis of isolated extracellular vesicles.

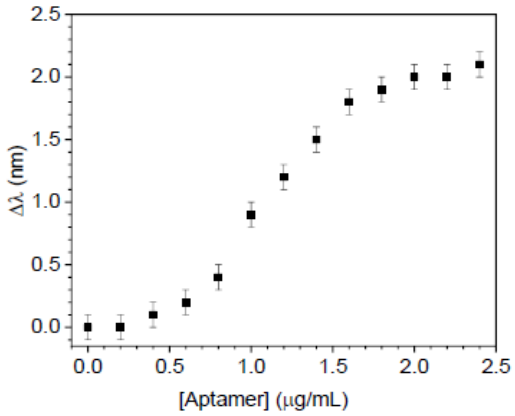

Figure S1. Kinetic binding curve showing the plasmonic peak shift as a function of the concentration of deprotected Ex.50.T.SH aptamer added to the AuNPs. The curve reaches a saturation value of approximately $\Delta\lambda \approx 2$ nm, which represents the completion of the adsorption process under the selected conditions rather than a full monolayer coverage of the nanoparticle surface. In fact, a 30-nm AuNP would be expected to exhibit a shift of ~12 nm upon complete substitution of the surrounding medium ($n = 1.33$) with a DNA layer ($n \approx 1.46$), indicating that the measured saturation corresponds to approximately 20% surface coverage. This partial functionalization—corresponding to roughly 50 aptamers per nanoparticle—proves advantageous for assay performance, as it provides sufficient aptamer density for target recognition while maintaining the reversible aggregation behavior required for an efficient colorimetric response.

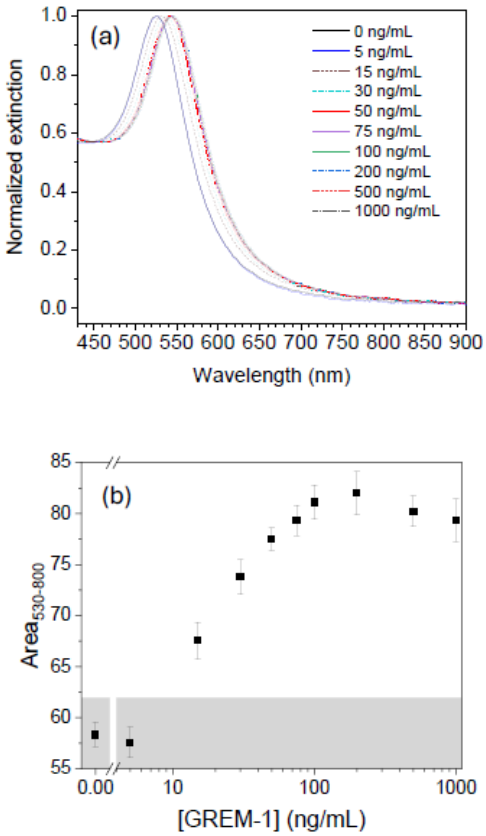

Figure S2. Functionalized gold nanoparticles were dispersed in ultrapure water and mixed with recombinant GREM1 (R&D System) diluted in 1× PBS at various concentrations. (a) Normalized extinction spectra at increasing GREM1 concentrations. (b) Integrated area in the 530–800 nm spectral range plotted against GREM1 concentration. The shaded region represents the baseline calculated with the 3SD method at the zero-concentration (blank) and leads to a minimum detectable concentration of approximately 10 ng/mL.

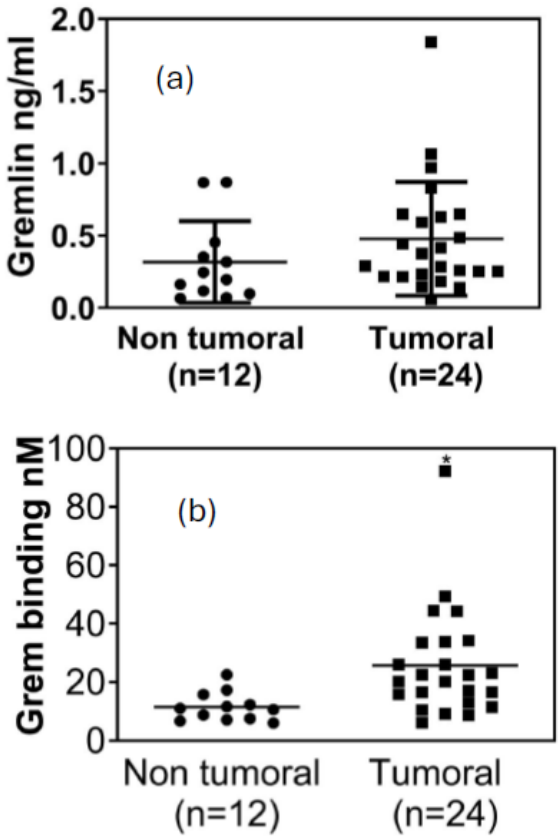

Figure S3. Comparison between (a) antibody-based ELISA and (b) aptamer-based Ex.50.T ELONA for GREM1 quantification in serum samples. While ELONA effectively discriminated between breast cancer patients and non-tumoral controls ($p = 0.0133$), ELISA did not show a statistically significant difference ($p = 0.2203$). Dot blot plots illustrate GREM1 levels measured by ELISA in total serum (left panel) and by Ex.50.T ELONA in the same sample set (right panel), highlighting the superior sensitivity of the Ex.50.T aptamer-based method. Statistical significance: *, $p < 0.05$.

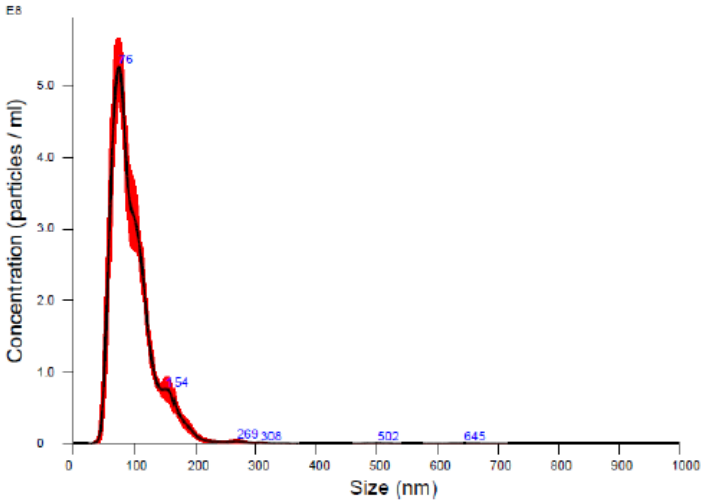

Figure S4. Nanoparticle Tracking Analysis (NTA) profiles of a representative sample of extracellular vesicles (EVs) isolated from tumoral human serum. The data confirm a size distribution and particle concentration (≈10^{10} particles/mL) consistent with typical EV populations, supporting the quality and reproducibility of the isolation process.

Finanziato dall'Unione europea NextGenerationEU
Italiadomani PIANO NAZIONALE DI RIPRESA E RESILIENZA
agritech

Rapid Label-Free Colorimetric ssDNA Biosensor Based on Gold Nanoparticles: Application to *Fusarium oxysporum* Detection in Soil

Erica Cavaliere[a], Tina D'Aponte[a], Emanuela Palomba[b], Maurizio Zotti[b], Pasquale Termolino[c], Vincenzo Iannotti [a,d], Stefano Mazzoleni[c], Raffaele Velotta[a], Bartolomeo Della Ventura[a*]

[a]Department of Physics "Ettore Pancini", University of Naples "Federico II", Via Cinthia 26, 80126 Naples, Italy.

[b]Department of Agricultural Sciences, University of Naples "Federico II", Piazza Carlo di Borbone 1, 80055 Portici (NA), Italy

[c]Institute of Biosciences and Bioresources, UOS Portici Via Università 133 80055 Portici (Italy)

[d]CNR – SPIN c/o Department of Physics "E. Pancini", Piazzale V. Tecchio 80, 80125 Naples, Italy

[*] Corresponding author bartolomeo.dellaventura@unina.it

Finanziato dall'Unione europea NextGenerationEU
Italiadomani PIANO NAZIONALE DI RIPRESA E RESILIENZA
agritech

ABSTRACT

Rapid and reliable detection of specific DNA sequences is essential for environmental and agricultural monitoring, yet amplification-based assays remain limited by equipment demand, multistep workflows, and susceptibility to matrix inhibitors. Here, we present a label-free colorimetric biosensor based on gold nanoparticles (AuNPs) and a freeze-mediated complementary-probe anti-aggregation mechanism (CPAA) for fast detection of Fusarium oxysporum ssDNA. The assay operates through a two-step hybridization process completed in 5 minutes, achieving a limit of detection of 2 nM (12 pg/µL). It exhibits high specificity toward non-complementary sequences, both individually and in complex mixtures, while tolerating a single central mismatch without loss of signal. This controlled mismatch tolerance enhances practical sensitivity when analysing fragmented or partially degraded DNA, as typically encountered in environmental samples. The biosensor maintains its performance with DNA extracted from soil, confirming robustness against real-matrix interference with minimal pretreatment. The platform is rapid, low-cost, and easily reconfigurable through probe substitution. Its simplicity and compatibility with automated and AI-assisted spectral interpretation make it well suited for on-site, large-scale environmental and agricultural diagnostics..

Keywords: Colorimetric biosensor, ssDNA detection, gold nanoparticles (AuNPs), environmental DNA, *Fusarium oxysporum*.

1. Introduction

Environmental DNA (eDNA) has rapidly become a cornerstone in ecological monitoring, enabling the detection of organisms through trace nucleic acids shed into the environment (e.g. water, soil, air) [1]. Its non-invasive nature and capacity to reveal low-abundance taxa make it a powerful tool for biodiversity assessment, invasive species surveillance, and pathogen tracking [2]. However, the utility of eDNA approaches hinges on the performance of the molecular assays employed. Ideal eDNA detection methods must combine high sensitivity and specificity with speed, simplicity, robustness against inhibitors in environmental matrices, and feasibility for field or high-throughput deployment [3]. Typically, rapid and accurate detection in complex samples depends on nucleic acid amplification methods like Polymerase Chain Reaction (PCR). While PCR is highly effective, it can be time-consuming, expensive, and requires specialized equipment. As further, its reliance on precise temperature control equipment makes it challenging to apply PCR in on-site settings [4]. Alternative methods like Loop-mediated Isothermal Amplification (LAMP), offer faster and less equipment-intensive solutions than PCR, but still involve multiple preparation steps and is not exempt from technical complications. A major challenge is the long hybridization times required for hybridization-based detection methods [5]. Thus, despite advances in PCR and metabarcoding, many published assays fall short in one or more of the characteristics required for large scale measurements, highlighting the need for alternative formats that better reconcile operational ease and analytical rigor.

Colorimetric and optical sensors are emerging as the most widely used class of biosensors, as they offer several advantages over conventional analytical techniques, enabling real-time, rapid, cost-effective, and label-free detection of a wide range of analytes [6–9]. In this context, gold nanoparticles (AuNPs) have been extensively employed as a sensing element for colorimetric detections owing to their unique optical properties and the straightforward functionalization of their surfaces. In many cases, nanomaterials that lack suitable optical or functionalization properties can be even endowed with these features by integrating AuNPs[10–12]. A key feature of AuNPs is their localized surface plasmon resonance (LSPR), which arises from the coherent oscillation of free electrons induced by resonant electromagnetic waves. When many-particles systems are considered, near-field and far-field LSPR couplings can also occur [9,13]. These phenomena lead to distinctive opto-plasmonic properties, including strong electromagnetic field enhancements exploited in plasmon-enhanced fluorescence biosensing [14] and characteristic plasmon redshifts upon particle aggregation in the

presence of targets, as utilized in colorimetric biosensors [15,16]. A crucial step in all these approaches is the functionalization of AuNPs with the appropriate biomolecule, enabling the resulting functionalized AuNPs (f-AuNPs) to bind the target with high specificity. Typically, AuNPs are functionalized either through noncovalent physical adsorption or via covalent bonding, most commonly through gold–thiol (Au–SH) interactions [16–18].

When the detection of single-stranded DNA (ssDNA) is targeted, the most straightforward biorecognition element to be immobilized on AuNPs is the complementary sequence. In this case, efficient immobilization of thiolated oligonucleotides (HS-oligos) requires overcoming the electrostatic repulsion between the negatively charged oligonucleotides and the likewise negatively charged AuNP surface. One common approach to overcome this barrier is to increase the ionic strength of the solution [19]. In this method, salt is slowly added at high concentration to shield the negative charges on the HS-oligos, promoting their adsorption onto the AuNP surface. However, this technique has limitations: it is time-consuming, and the high salt concentration can induce AuNP aggregation [20]. An alternative is the low-pH-assisted method, which rapidly lowers the pH to ~3 [21,22]. At this pH, adenosine and cytosine residues become protonated, partially neutralizing the oligonucleotide backbone and reducing electrostatic repulsion. While this method is fast, its efficiency critically depends on the nucleotide composition of the oligo [23]. To circumvent these issues, an effective strategy is the freezing–thawing technique, which enables strong HS-oligonucleotide adsorption under low-salt conditions and high oligonucleotide concentration [24]. During freezing, the formation of ice crystals concentrates solutes in the unfrozen liquid phase. This localized increase in solute concentration, together with the alignment and stretching of oligonucleotides upon freezing, promotes rapid adsorption onto AuNPs—often occurring within minutes [25].

Once functionalized with HS-oligos, f-AuNPs can be used for colorimetric detection through target-induced nanoparticle aggregation, which typically occurs via two mechanisms classified as either cross-linking (CL) [19] or non-cross-linking (NCL) [26]. The CL DNA detection method employs two sets of AuNPs functionalized with ssDNA probes that recognize the two ends of the ssDNA target. If the ssDNA target is recognized this results in particle aggregation and a visible color shift from red to blue [19]. In the NCL method, a single batch of AuNPs bearing ssDNA probes hybridizes with the target, converting flexible, highly charged

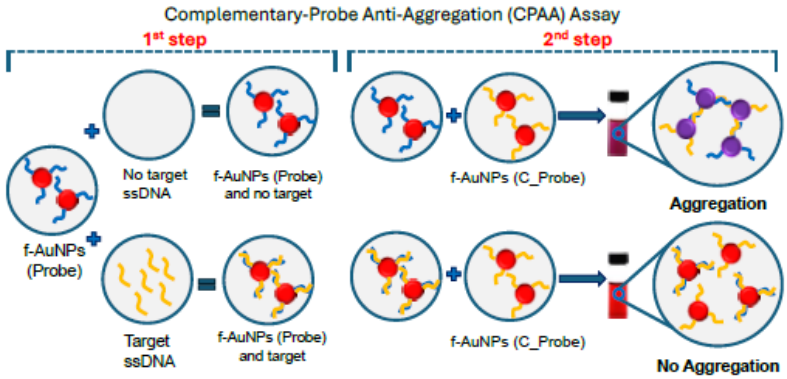

Figure 1. Schematic representation of the colorimetric assay: In the presence of the target, hybridization with Probe–AuNPs prevents aggregation upon addition of C_Probe–AuNPs. In the absence of the target, Probe–AuNPs and C_Probe–AuNPs hybridize with each other, leading to nanoparticles aggregation and a visible color change.

ssDNA into more rigid dsDNA with lower charge density. This reduces electrostatic and steric stabilization, so in the presence of salt the AuNPs lose colloidal stability and aggregate without forming interparticle cross-links. The NCL method is generally faster and less temperature-dependent than the CL approach [27,28], but the latter typically offers higher specificity and sensitivity [29]. NCL performance, however, is strongly influenced by ionic strength, as aggregation occurs only under optimized salt conditions [30]. Both methods are highly sequence-length dependent: the CL assay fails when the target is truncated or embedded in longer fragments, while the NCL assay is particularly sensitive to terminal mismatches or length variations. These features limit their applicability to real samples, where DNA fragments often display heterogeneous lengths. Consequently, there is a clear need for a more robust and adaptable detection strategy.

To overcome these limitations, we developed a novel two-step, label-free colorimetric biosensor based on an anti-aggregation mechanism, in which the presence of the ssDNA target inhibits nanoparticle aggregation (Complementary-Probe Anti-Aggregation Assay, CPAA). The assay uses two batches of AuNPs functionalized with ssDNA Probe and its complementary (C_Probe). As illustrated in Figure 1, the target first hybridizes with Probe–AuNPs (first step), after which C_Probe–AuNPs are introduced (second step). When the target is present, its binding to Probe prevents Probe /C_probe hybridization, maintaining the red color of the colloid; in its absence, Probe and C_Probe hybridize, causing aggregation and a visible color shift. Each hybridization

step is freeze-mediated [31,32], enabling rapid detection and completion of the entire assay within 5 minutes with a limit of detection of 2 nM (12 pg/µL). We tested the functionality of the sensor using the plant pathogenic fungus *Fusarium oxysporum* — one of the most widespread phytopathogens in agricultural systems worldwide [33,34] — in ultrapure water, as well as its response to DNA extracted from soil samples.

2 Experimental

2.1 Reagents and materials

Gold(III) chloride trihydrate ($HAuCl_4 \cdot 3H_2O$), sodium citrate, Phosphate buffered saline (PBS 0.01 M, pH 7.4) and Tris (2-carboxyethyl) phosphine hydrochloride (TCEP) were purchased from Sigma-Aldrich (Milano, Italy). All aqueous solutions were prepared using ultrapure water (24 MΩ·cm) purified with a Milli-Q system (Millipore, Burlington, MA, USA)

For the design of *F. oxysporum*-specific sequences, a single sequence was obtained by querying the NCBI database for the Internal Transcribed Spacer 1 (ITS1), 5.8S ribosomal RNA gene, Internal Transcribed Spacer 2 (ITS2), and Large Subunit ribosomal RNA gene (LSU) of fungi belonging to the genus *Fusarium*. All available sequences of *F. oxysporum* were retrieved, while three representative sequences for approximately 100 additional *Fusarium* species were included for comparison. The sequences were imported into MEGA7 and aligned using the ClustalW algorithm. After alignment, excessively long regions were trimmed, and the sequences were visually inspected to identify a 20 bp sequence conserved among all *F. oxysporum* accessions and differing by at least two bases from other *Fusarium* species.

All ssDNA oligonucleotides were synthesized by Biogenerica Srl (Pedara, Italy) as lyophilized powders. The sequences are listed in Table 1.

Table 1

List of ssDNA sequences used in AuNPs-based colorimetric biosensor.

	ssDNA sequences	Sequence 5' to 3'
1	*F. oxysporum* Probe	Thiol-C6- AAAAACCCCC TCA AAA CCT CAA TGA GTG CG
2	*F. oxysporum* C_Probe	Thiol-C6- AAAAACCCCC CGC ACT CAT TGA GGT TTT GA
3	*F. oxysporum* target (TS)	CGC ACT CAT TGA GGT TTT GA
4	Non-target sequence 1 (NTS1)	GTG CGA TGG TTG GTA GTA GT

5	Non-target sequence 2 (NTS2)	ACT ACT ACC AAC CAT CGC AC
6	Non-target sequence 3 (NTS3)	GCT GGT CAA GGT TTC TCT GC
7	Non-target sequence 4 (NTS4)	ACT GAA AGA GAG GGA AAT GGA GGG ACG GTC

2.2 Synthesis of Gold nanoparticles (AuNPs)

Spherical gold nanoparticles (AuNPs) were synthesized by modifying an already-existing protocol [36]. A gold salt solution composed of 40 mL of ultrapure water and 500 µL of $HAuCl_4 \cdot 3H_2O$ [10 mg/mL] was prepared and boiled under constant vigorous stirring. When boiling point was reached, 1.5 mL of sodium citrate [23.5 mg/mL] was added, and further 15 min were needed to achieve the particles nucleation and seed growth. At the end of this process, the colour of the suspension turned wine-red with an optical density (OD) of approximately 1 at the wavelength (λ) of 522 nm, which allowed us to estimate the AuNPs concentration as ≈ 10^{11} AuNPs·mL^{-1} with a diameter of ≈ 20 nm. Transmission electron microscopy (TEM) analysis confirmed the size and spherical morphology of the nanoparticles (Figure S1). The AuNPs colloid was stored under dark conditions at 4°C.

The reliability of AuNP-based colorimetric biosensors for ssDNA detection depends critically on nanoparticle size, with 20–25 nm AuNPs offering an optimal balance over smaller sizes [23]. To prepare the assay reagents, the AuNP suspension was concentrated to an OD of 4 by centrifugation at 3500 g for 30 minutes, followed by resuspension in Milli-Q ultrapure water.

2.3 Preparation of ssDNA oligonucleotides

Stock solutions of ssDNA (100 µM) were prepared by dissolving lyophilized oligonucleotides in Milli-Q water and stored frozen as recommended by the supplier. The ssDNA probes were modified at the 5′ end with a thiol-C6 group to enable the covalent immobilization on AuNPs [37]. Additionally, a 10-base spacer was added to reduce steric hindrance and enhance target accessibility. The spacer sequence and length significantly affect biosensor selectivity. Spacers composed of nucleobases with high gold affinity, such as polyadenine, have been shown to improve long-term stability. However, shorter spacers (10 bases) result in higher hybridization efficiency, enhancing assay sensitivity and enabling faster and stronger signal changes upon target hybridization [38,39]. Before use, the thiolated ssDNA was chemically activated by treatment with TCEP at a 100:1 molar ratio (TCEP:ssDNA) for 1 hour at room temperature (RT) to induce the reduction of the disulfide

bonds. The freshly activated ssDNA probe was used immediately after this reduction step. Since the target ssDNA did not require the TCEP activation, it was prepared by simply diluting the stock solution to the desired concentrations in Milli-Q water immediately before testing.

2.4 Instruments and measurements

UV–vis spectroscopy was employed to characterize both bare and functionalized AuNPs and to examine the optical responses of the functionalized AuNPs (f-AuNPs) after the detection of the ssDNA target. The UV–vis absorption spectra were measured by a spectrophotometer (NanoPhotometer® NP80, Implen, Germany), which offers a resolution of 1 nm. Dynamic light scattering (DLS) measurements, used to confirm the UV-vis spectroscopy in terms of size of the AuNPs and f-AuNPs, were performed using a Zetasizer Nano ZS instrument (Malvern Instruments), equipped with a 633 nm He–Ne laser and an avalanche photodiode detector positioned at a detection angle of 173°. The morphology of the bare and f-AuNPs was characterized using transmission electron microscopy (TEM) with a JEOL JEM-2100 microscope (JEOL Ltd., Japan). To avoid overcrowded micrograph images, the f-AuNps were diluted 10-fold in MilliQ water.

2.5 AuNPs functionalization

The functionalization of the AuNPs with ssDNA was achieved by exploiting the Au–S bond formation [40]. The sequence 5'ThiolAAAAACCCCCTCAAAACCTCAATGAGTGCG-3' (Probe for *F. oxysporum* genome) was activated with TCEP, by using different ssDNA:AuNP molar ratios (from 200:1 to 1000:1). The mixture was subjected to a brief freeze–thaw cycle (2 minutes on dry ice followed by thawing at room temperature) [24]. Eventually, the unbound ssDNA was removed by a centrifugation step at 16.000 g, 4 °C for 10 minutes. The final pellet was resuspended in 5 mM PBS. Since the presence of ssDNA on the AuNP surface stabilizes the colloidal solution by preventing interparticle coupling [41], the extinction spectrum after resuspension can be used to monitor the degree of surface coverage. As shown in [42], an effective way to quantify this coverage is to evaluate the ratio between the extinction at the plasmon peak and at a wavelength on the red side of the spectrum, where aggregation-induced broadening is most pronounced. In particular, they demonstrate that, for well-functionalized 13 nm AuNPs, the ratio between the extinction at the shoulder of the spectrum and at the peak must remain below 0.3: values higher than 0.3 indicate insufficient ssDNA coverage and therefore poor

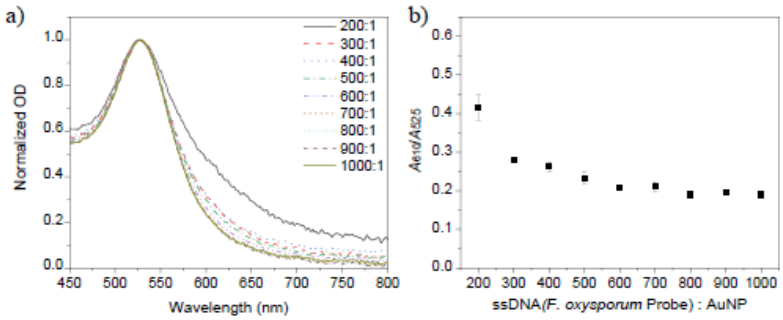

Figure 2. (a) Normalized UV–Vis extinction spectra of AuNPs functionalized with the *Fusarium* probe at different ssDNA:AuNP molar ratios. (b) Corresponding absorbance ratio at 610 nm and 525 nm (A_{610}/A_{525}) which reached an optimal value of 0.28 at a ratio of 300:1. Error bars represent duplicate experiments.

colloidal stability, whereas values that are too low reflect excessive surface coverage, which can hinder hybridization with the complementary sequence and reduce biosensor sensitivity.

In our case, inspection of the extinction spectra for different ssDNA:AuNP molar ratios (Figure 2a) shows that the wavelength around 610 nm is the most responsive to variations in surface coverage, and was therefore selected as the reference wavelength on the red side of the peak, whereas the plasmon peak was set at 525 nm. Based on these considerations, the ratio A_{610}/A_{525} was used as a quantitative indicator of functionalization efficiency. Tests performed at different ssDNA:AuNP molar ratios showed that A_{610}/A_{525}=0.28 provides the optimal balance between colloidal stability and sensing performance, which is achieved at a molar ratio of 300:1 (Figure 2b).

It is worth considering that the optimal ssDNA:AuNP molar ratio value depends on the specific probe sequence used for functionalization. As illustrated in Figure S2, the complementary sequence (*F. oxysporum* C_probe) requires a distinct molar ratio to achieve the same A_{610}/A_{525} ratio of 0.28. This sequence dependence can be explained by the tendency of some ssDNA sequences to form secondary structure involving the spacer and the thiol group. When thiolated ssDNA adopts a secondary structure, its immobilization efficiency during the functionalization is reduced [43], requiring a higher ssDNA:AuNP ratio to achieve a certain coverage. The surface density of ssDNA on AuNPs is a critical parameter: while higher densities enhance colloidal stability,

lower densities can improve biosensor sensitivity: balancing this trade-off is key to achieving optimal performance [44].

2.6 AuNPs characterization

After functionalization, the AuNPs were washed to remove the excess of ssDNA required for the functionalization [20], and then resuspended in PBS 5 mM. The centrifugation step removes not only unbound ssDNA from the solution, but also the aggregates formed during freezing procedure. This is coherent with the extinction spectra shown in Figure S3 in which f-AuNPs (functionalized with *F. oxysporum* Probe at an ssDNA:AuNP molar ratio of 300:1) initially show a ratio A_{610}/A_{525} = 0.28, which decreases to 0.24 after centrifugation step due the removal of aggregates.

To investigate how ssDNA surface density affects colloidal behaviour, we compared two batches of post-washing f-AuNPs obtained using different ssDNA:AuNP molar ratios: 300:1 (A_{610}/A_{525}= 0.24) and 700:1 (A_{610}/A_{525}= 0.16) (Figure 3a). DLS analysis (Figure 3b) revealed an average hydrodynamic diameter of 23 nm

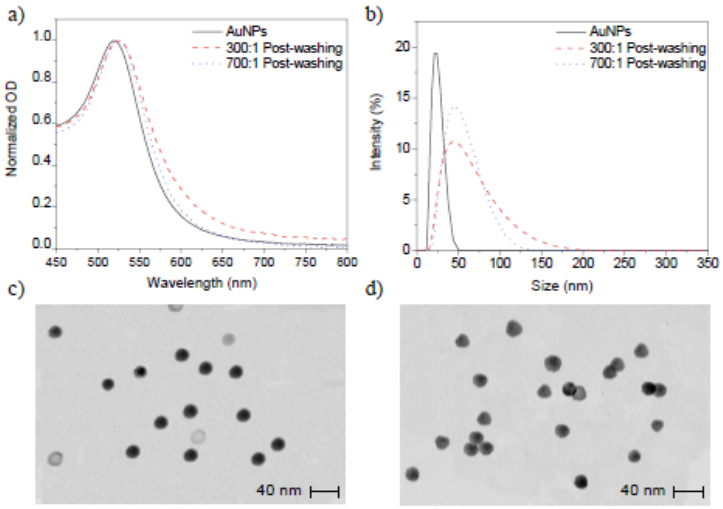

Figure 3. Characterization of f-AuNPs (functionalized with *F. oxysporum* Probe). (a) UV–Vis extinction spectra of f-AuNPs prepared at ssDNA:AuNP molar ratios of 300:1 and 700:1. (b) DLS analysis showing an increase in hydrodynamic diameter for both samples, arising from different causes: a dense ssDNA shell for the 700:1sample versus few-particles aggregation for the 300:1 sample. (c) TEM image 700:1 sample, showing well-dispersed colloidal suspension (d) TEM image of the 300:1 sample, revealing the presence of few-particle aggregation (dimers and trimers).

for bare AuNPs, increasing to ~45 nm for both functionalized samples but this increase in size depends by different reasons.

In the 700:1 sample, the increase arises from an excess of ssDNA forming a dense, uniform shell around each particle. This provides excellent colloidal stability also confirmed by TEM; (Figure 3c), where particles appear identical to bare AuNPs (Figure S1, Section 2.2). Thus, DLS analysis confirms the presence of surface-bound DNA, as indicated by an average hydrodynamic size increase of ~20 nm. This increment is consistent with the expected contribution of a 30-base ssDNA strand (~10 nm) extending from each side of the nanoparticle surface, suggesting dense and uniform functionalization.

In contrast, the 300:1 sample shows an increase in hydrodynamic size, which is attributed to few-particle aggregation rather than to the development of a thicker DNA shell. Although the DNA loading is lower than in the 700:1 condition, it is still sufficient for functionalization but insufficient to maintain strong interparticle

repulsion, leading to partial nanoparticle aggregation. Few-particle formation is further supported by TEM imaging (Figure 3d). These results suggests that while a high DNA excess (700:1) maximizes colloidal stability, it may limit probe accessibility, whereas a 300:1 ratio provides a more balanced compromise between stability and functional performance.

To further investigate the impact of the DNA loading ratio, we estimated the surface coverage by calculating the number (N) of ssDNA strands attached per nanoparticle for both ratios (300:1 and 700:1) [45]:

$$N = \frac{C_{\text{added}} - C_{\text{free}}}{C_{\text{AuNPs}}}, \quad (1)$$

In Equation (1), C_{Added} is the concentration of the ssDNA added to the colloidal solution, C_{free} is the concentration remaining in the supernatant after centrifugation, and C_{AuNPs} is the concentration of the AuNPs. For a molar ratio 300:1, we obtained $N \approx 220$, and for molar ratio 700:1, $N \approx 370$.

Once N values were obtained, the area A_{ssDNA} occupied by a ssDNA was calculated as:

$$A_{\text{ssDNA}} = \frac{\pi d^2}{N} \quad (2)$$

where d is the AuNP diameter. The resulting values are $A_{\text{ssDNA}} = 6.0$ nm^2 for the 300:1 sample and $A_{\text{ssDNA}} = 3.5$ nm^2 for 700:1 sample.

The calculated N and A_{ssDNA} values for the 300:1 and 700:1 batches confirm a higher ssDNA surface density and reduced inter-strand spacing in the 700:1 batch, indicating increased surface coverage, thereby promote steric hindrance and potentially reducing hybridization efficiency. The specific values used in the formulas above are provided in Table S1.

2.7 Real samples preparation and DNA extraction

Soil samples were obtained from a controlled-environment experiment designed to test the mycorrhization of Quercus pubescens with Tuber aestivum. Prior to use, the absence of *F. oxysporum* in the soil was confirmed through a metagenomic analysis aimed at characterizing the fungal community (mycobiota), using ITS1 and ITS2 regions as primers. The bulk soil was subsequently divided into two aliquots of 50 g each. One aliquot was left untreated and served as a control, free of *F. oxysporum*. The second aliquot was inoculated with *F. oxysporum* suspension.

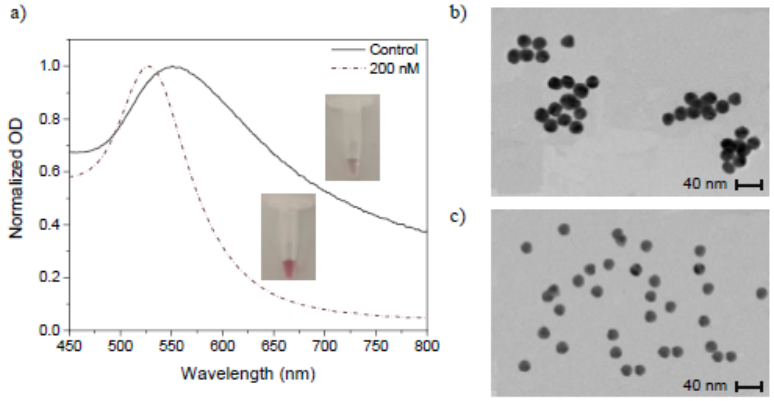

Figure 4. (a) Normalized extinction spectra for some of the condition tested. Control extinction spectrum (no target ssDNA) which shows maximum AuNPs aggregation compared to the extinction spectrum for 200 nM target ssDNA (maximum concertation tested), showing the minimal aggregation. (b) TEM image of control solution, confirming extensive nanoparticles aggregation. (c) TEM image of 200 nM of ssDNA target detection, confirming reduced aggregation at high target concentration.

The inoculum was prepared by scrapping the surface of a 60 mm diameter petri dish to remove *F. oxysporum* mycelium. The collected sample, corresponding to around 0.5 g of fresh mycelium, was then diluted in 5 mL of sterile water and mixed by stirring for 3 minutes until the suspension appeared homogenized by visual inspection. The *F. oxysporum* suspension was subsequently added to the prepared 50 g soil sample. The soil was thoroughly mixed by stirring for 1 minute and was then used for total DNA extraction.

Prior to extraction, a subsample of 2 g of soil was diluted in 20 mL of PBS (phosphate-buffered saline) to promote osmotic imbalance and facilitate the breakdown of mycelial membranes. The solution was concentrated by centrifugation at 12000 g for 2 minutes; the supernatant was discarded, and the pellet was used for DNA extraction. Total DNA from each soil sample was extracted through multiple independent extractions using the DNeasy PowerSoil Kit (Qiagen, Hilden, Germany), and the final volume was adjusted to 100 µL in the buffer C6 (10 mM Tris-HCl, pH 8.5), the elution buffer supplied with the kit.

2.8 Sonication and Gel electrophoresis

Prior to use, the real sample was sonicated for 2 hours in an ultrasonic bath (Elmasonic S 40 H, 37 kHz) to reduce DNA fragment size. To assess the effect of sonication, the treated samples were analyzed by agarose gel electrophoresis. A 1% (w/v) agarose gel was prepared in 1× TAE buffer and stained with GelRed

(1:10.000). Wells were formed using a standard comb. DNA samples were mixed with 6× loading dye in a 1:5 ratio (dye:sample), and 12 µL of each sample, along with a 50 bp DNA ladder (Thermo Scientific, SM0371), was loaded into the gel. Electrophoresis was carried out at 100 V for 45–60 min in 1× TAE running buffer. DNA fragments were visualized under UV light using a ChemiDoc Imaging System (Bio-Rad).

3. Results and discussion

3.1 Operative principle of the biosensor

The biosensor operates through a two-step, label-free colorimetric mechanism based on the anti-aggregation of gold nanoparticles (AuNPs), with hybridization promoted by freezing. This approach allows rapid detection of the target DNA sequence (5′ CGCACTCATTGAGGTTTTGA 3′) within 5 minutes. Two batches of AuNPs are employed: one functionalized with *F. oxysporum* Probe and the other with *F. oxysporum* C_Probe. The overall detection principle depicted in Figure 1 is realized by the following procedure.

1) Mix 10 µL of *F. oxysporum* Probe-AuNPs (OD 4) with 40 µL of target sequence suspension at concentrations in a range of 0–200 nM.
2) Incubate for 1 minute at −80°C on dry ice.
3) Thaw at room temperature and add 10 µL of *F. oxysporum* C_Probe-AuNPs (OD 4).
4) Incubate for 1 minute at −80 °C on dry ice.
5) Acquire the extinction spectra.

3.2 Dose-response curve

To identify the optimal biosensing parameter, the full extinction spectrum was measured for several target sequence concentrations. Spectra were normalized to their maximum optical density (OD), and the 550–800 nm range—where spectral changes are most pronounced—was selected, as it provides the clearest information on ssDNA presence and nanoparticle aggregation (Figure S4a-b). In this system, absence of the ssDNA target results in maximal aggregation, like the control (no ssDNA), whereas increasing target concentration progressively reduces aggregation (Figure 4a). TEM analysis confirmed this trend: large aggregates form in the absence of the target (Figure 4b), while they are absent at high concentrations (200 nM; Figure 4c).

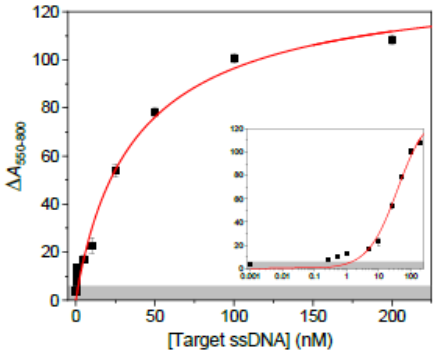

Figure 5. Dose-response curve obtained detecting the target ssDNA sequence in ultrapure water. The inset displays the same curve on a semi-logarithmic scale. The error bars in the figure represent the results of triplicate experiments.

To obtain a robust sensing parameter, we introduced the integrated absorbance difference, $\Delta A_{550\text{-}800} = A_{control} - A_{sample}$ (Figure S4c). Plotting $\Delta A_{550\text{-}800}$ as a function of the ssDNA target concentration yielded the dose–response curve in ultrapure water (Figure 5).

The measurements were performed in triplicate and fitted using a three-parameter Hill equation

$$y = \frac{V_{max} \cdot x^n}{K_m{}^n + x^n} \quad (3)$$

In Eq. (3) $V_{max} = 135 \pm 21$ is the saturation value of $\Delta A_{550\text{-}800}$, $K_m = 38 \pm 16$ nM is the analyte concentration at which half of this saturation value is reached, and $n = 0.9 \pm 0.2$ is the Hill coefficient. Applying the 3σ criterion (shaded area in Figure 5), we achieved a LOD of 2 nM (12 pg/µL). Here the LOD was calculated by adding three times the standard deviation of the signal obtained from multiple measurements of the zero-concentration sample (i.e., in the absence of the target) to its mean value [46,47]. Various f-AuNPs having different A_{610}/A_{525} ratios were tested, revealing optimal performance for f-AuNPs with a A_{610}/A_{525} ratio of 0.24 (Figure S5).

3.2 Specificity tests

To evaluate the specificity of the developed biosensor, we assessed its response against various ssDNA sequences (Table 1, entries 3–9), including the 20 bp target sequence (TS). Each non-target sequence (NTS)

and the TS were tested individually under identical experimental conditions, at 200 nM, corresponding to the highest concentration tested in dose-response curve. As shown in Figure 6a, all the NTSs elicit only negligible responses, whereas the TS generates a significant signal.

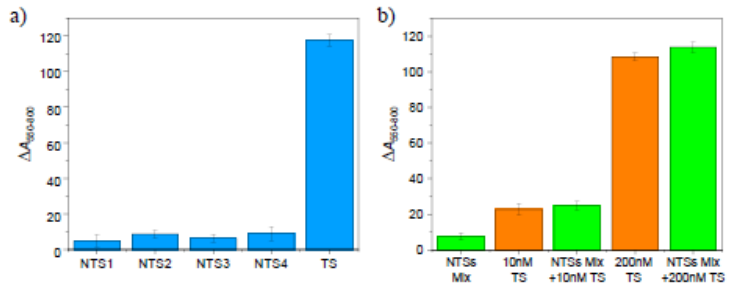

Figure 6. Specificity of the developed DNA biosensor. (a) Biosensor response to individual ssDNA sequences: the target sequence (TS, 200 nM) produces a strong signal, whereas non-target sequences (NTSs, 200 nM) show only negligible responses.(b) Biosensor response to the TS in the presence of a mixture of non-target sequences (NTSs Mix, each at 200 nM): the mixture alone produces no signal, but upon addition of the TS at 10 nM and 200 nM (green bars), the signal intensity closely matches that of the TS tested alone (orange bars). Error bars represent duplicate experiments.

To further investigate the biosensor's ability to detect the target in the presence of other ssDNA sequences, we prepared a mixture of non-target sequences (NTSs Mix), each at 200 nM. When tested alone, this mixture produced no significant signal. When the target ssDNA was added at two different concentrations (10 nM and 200 nM), the resulting signals closely match those obtained for the TS alone (Figure 6b). These results demonstrate that the biosensor effectively detects its target even in a complex mixture.

Experiments using AuNPs functionalized with different probe sequences (Table S2) also show that the biosensor can detect the target even when embedded within a longer sequence (30 bp), and that longer non-target sequences (50 bp) do not interfere with its specificity (Figure S6). Moreover, a single central mismatch generates essentially the same signal as the fully complementary target, implying that this mismatch does not prevent hybridization under the assay conditions.

Additionally, we evaluated the stability of these functionalized AuNPs and found that they remained fully functional for 15 days, after which a gradual 10 % loss of activity was observed between days 16 and 140 (Figure S7).

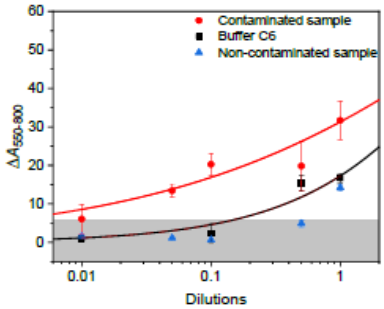

Figure 7. Signal response across serial dilutions for contaminated soil (red circles), C6 buffer alone (black squares). and non-contaminated soil (blue triangles). Both soil samples exhibited elevated signals at the highest concentrations (undiluted and 1:2), but only the contaminated sample showed a clear dose-dependent response at higher dilutions (1:10–1:100), where buffer interference is negligible. The non-contaminated sample displayed no specific signal beyond the background level, with its undiluted and 1:2 responses matching those of the buffer control, confirming that the elevated signals at low dilutions can be ascribed to buffer-induced interference. To account for this effect in quantitative analysis, all data were fitted using a Hill equation with $V_{max} = 135$, which is the value obtained from the interference-free calibration curve. The resulting fits confirm that the non-contaminated sample's response is indistinguishable from background noise, whereas the contaminated sample yields a robust analyte-specific signal. Error bars represent duplicate measurements.

3.3 Real sample test

After evaluating the biosensor's specificity, we tested its performance using DNA extracted from soil samples, referred to here as real samples. Unlike the samples previously prepared in water, the real samples were sonicated for 2 hours in an ultrasonic bath (Elmasonic S 40 (H), 37 kHz). Sonication was used to fragment the DNA, producing shorter ssDNA strands and thus improving detection specificity. The effectiveness of the sonication process was verified by gel electrophoresis (Figure S8).

Two identical soil samples were prepared as described in Section 2.7. After confirming the absence of *F. oxysporum* DNA in both samples, one was inoculated with *F. oxysporum*, while the other served as a control. Fresh *F. oxysporum* mycelium was introduced into the soil to achieve a concentration consistent with levels typically used in laboratory studies [48,49]. Following DNA purification, spectrophotometer measurements showed total DNA concentrations of 22 ng/µL and 15 ng/µL for the non-contaminated and contaminated soils, respectively. This indicates that the presence of *F. oxysporum* DNA did not significantly alter the total DNA content in the soil. Undiluted and serially diluted extracts (1:2, 1:10, 1:50, 1:100) from both samples were then tested using AuNPs functionalized with *F. oxysporum* probes, and the results are presented in Figure 7.

In the extract from the non-contaminated soil (control) (Figure 7), no detectable signal was observed across all dilutions, except at the highest concentrations (undiluted and 1:2). In contrast, the extract from the contaminated soil produced strong signals. The elevated signals at low dilutions obtained in both samples were not due to a lack of specificity — both the biosensing system and probes had already been validated — but rather resulted from interference caused by the extraction buffer. We identified the C6 buffer used in the final step of DNA extraction, as the potential source of this interference. To verify this hypothesis, we tested the AuNPs functionalized with *Fusarium* probes against the buffer itself, and the data confirmed that the increased signals observed at the undiluted and 1:2 dilutions were indeed caused by the high buffer concentration. To account for this interference in quantitative analysis, data were fitted using the same Hill equation applied to the reference dose–response curve. However, because the C6 buffer interferes at lower dilutions (undiluted and 1:2), these points do not reflect true system saturation. To avoid biasing the fit with these distorted low-dilution values, V_{max} was fixed to the value obtained from the interference-free dose–response curve, while the remaining Hill parameters were estimated from the data. This approach yields a robust and biologically meaningful fit, free from artefactual inflation or suppression of the plateau.

Under this constraint, the non-contaminated sample exhibits a response indistinguishable from that of the buffer C6: both experimental points and the fitted curve lie within the background noise region, confirming the absence of a specific analyte signal. These results conclusively demonstrate that the control sample contains no detectable *F. oxysporum* DNA, as its response is fully consistent with baseline interference. In contrast, the contaminated sample exhibited a clear, concentration-dependent response that rose well above background interference even at high dilutions, although signals at the lowest dilutions (undiluted and 1:2) remained affected by residual buffer interference. To ensure accurate detection and minimize this effect, we recommend the dilution of the samples. Consistently, we consider as the optimal detectable signal that obtained at the 1:10 dilution. According to the dose–response curve (Figure 5) and considering the dilution factor, the estimated *F. oxysporum* DNA concentration of the sample was approximately 50 nM. By considering a mean value of 250 bp for the fragment distribution (Figure S8), this corresponds to approximately 4 ng/µL, a value consistent with a contamination level too low to significantly impact the total soil DNA content. Notably, a detectable signal was still obtained at the 1:100 dilution, indicating that the initial *F. oxysporum* concentration used to

contaminate the soil could be reduced by at least one order of magnitude without compromising detection performance.

For practical, real-world applications, the biosensing platform could be further optimized by reducing the required initial *F. oxysporum* concentration. This can be achieved by extracting DNA from larger soil samples, increasing the total amount of target DNA available. Additional improvements could be obtained by concentrating the extracted DNA or by removing residual extraction buffer through an extra washing step. Implementing these strategies would lower the minimum amount of *F. oxysporum* needed for reliable detection—potentially by one or more orders of magnitude— making the assay more applicable to field conditions.

4. Conclusions

Rapid and accurate detection of *Fusarium oxysporum* in soil is crucial for effective crop protection, as its presence strongly influences agricultural management strategies. The use of chemical pesticides, for instance, poses risks such as food safety concerns (chemical residues), loss of biodiversity in adjacent natural ecosystems, and reduction of beneficial microbial communities in agricultural soils [50]. Less impactful strategies rely on biological control agents, including mycoparasitic fungi of the genus *Trichoderma* (e.g., *T. harzianum*), which are widely applied against Fusarium wilt [51]. In all cases, the presence of the pathogen entails additional management costs that ultimately affect the price of agro-food products. Yet, the lack of tools capable of accurately quantifying Fusarium populations in soils hampers targeted interventions and often leads to the excessive use of both chemical and biological control agents [52].

In this work, we developed a rapid, label-free colorimetric biosensor that integrates freeze–thaw-mediated hybridization with AuNP anti-aggregation for the detection of *F. oxysporum* ssDNA. By tuning nanoparticle size, probe density and freezing conditions, the assay achieved a 2 nM detection limit and required only 5 minutes to complete. The biosensor strongly discriminated non-complementary sequences while tolerating a single central mismatch without affecting the colorimetric output. Rather than reducing selectivity, this controlled mismatch tolerance improves practical sensitivity when analysing fragmented or partially degraded DNA, which is the typical form found in real environmental matrices.

When tested on DNA extracted from soil, the sensor maintained both sensitivity and selectivity despite the presence of matrix inhibitors, confirming its robustness for real-sample applications. The minimal reaction

volume (40 µL) and visual readout make the assay particularly suitable for on-site diagnostics, especially in resource-limited settings.

Overall, the proposed platform represents a reliable, affordable and amplification-free alternative to conventional molecular assays. Its modular architecture allows rapid adaptation to other DNA targets by simply changing probe sequences. Future integration with automated handling systems and AI-assisted spectral analysis may further enhance throughput, reduce user variability, and support real-time decision-making in agricultural, clinical and environmental monitoring.

CRediT authorship contribution statement

Erica Cavaliere: Investigation, Visualization, Data curation, Writing - Original Draft. **Tina D'Aponte:** Investigation, Visualization, Formal analysis. **Emanuela Palomba:** Investigation, Validation, Resources. **Maurizio Zotti:** Validation, Resources. **Pasquale Termolino:** Investigation, Validation, Writing - Original Draft. **Vincenzo Iannotti:** Methodology, Writing - Review & Editing. **Stefano Mazzoleni:** Methodology, Resources, Funding Acquisition, Writing - Review & Editing. **Raffaele Velotta:** Supervision, Formal analysis, Writing - Review & Editing, Funding Acquisition. **Bartolomeo Della Ventura:** Conceptualization, Methodology, Formal analysis, Writing - Review & Editing, Funding Acquisition.

Acknowledgement

This study was carried out within the Agritech National Research Center and received funding from the European Union Next-Generation EU (PIANO NAZIONALE DI RIPRESA E RESILIENZA (PNRR) – MISSIONE 4 COMPONENTE 2, INVESTIMENTO 1.4 – D.D. 1032 17/06/2022, CN00000022). Additional funding was provided by the Italian Ministry of University and Research through the following projects: PRIN PNRR Project P2022J3ZPW and PRIN 2022WFRAE7.

References

[1] N.J. Iacaruso, O.P. Reves, S.J. Merkelz, C.L. Waldrep, M.A. Davis, A systematic review evaluating the performance of eDNA methods relative to conventional methods for biodiversity monitoring, Ecography (2025). https://doi.org/10.1002/ecog.07952.

[2] T. Çevik, N. Çevik, Environmental DNA (eDNA): A review of ecosystem biodiversity detection and applications, Biodivers Conserv 34 (2025) 2999–3035. https://doi.org/10.1007/s10531-025-03112-y.

[3] H.J. Yoon, J.H. Seo, S.H. Shin, M.A.A. Abdelhamid, S.P. Pack, Bioinformation and Monitoring Technology for Environmental DNA Analysis: A Review, Biosensors (Basel) 15 (2025) 494. https://doi.org/10.3390/bios15080494.

[4] M. Tan, C. Liao, L. Liang, X. Yi, Z. Zhou, G. Wei, Recent advances in recombinase polymerase amplification: Principle, advantages, disadvantages and applications, Front Cell Infect Microbiol 12 (2022). https://doi.org/10.3389/fcimb.2022.1019071.

[5] L. Becherer, N. Borst, M. Bakheit, S. Frischmann, R. Zengerle, F. Von Stetten, Loop-mediated isothermal amplification (LAMP)-review and classification of methods for sequence-specific detection, Analytical Methods 12 (2020) 717–746. https://doi.org/10.1039/c9ay02246e.

[6] S. Akgönüllü, A. Denizli, Recent advances in optical biosensing approaches for biomarkers detection, Biosens Bioelectron X 12 (2022) 100269. https://doi.org/10.1016/j.biosx.2022.100269.

[7] K. Sharma, M. Sharma, Optical biosensors for environmental monitoring: Recent advances and future perspectives in bacterial detection, Environ Res 236 (2023) 116826. https://doi.org/10.1016/j.envres.2023.116826.

[8] J. Zhou, Y. Liu, X. Du, Y. Gui, J. He, F. Xie, J. Cai, Recent Advances in Design and Application of Nanomaterials-Based Colorimetric Biosensors for Agri-food Safety Analysis, ACS Omega 8 (2023) 46346–46361. https://doi.org/10.1021/acsomega.3c06409.

[9] A. Acunzo, E. Scardapane, M. De Luca, D. Marra, R. Velotta, A. Minopoli, Plasmonic Nanomaterials for Colorimetric Biosensing: A Review, Chemosensors 10 (2022). https://doi.org/10.3390/chemosensors10040136.

[10] D. Marra, A. Acunzo, A. Fulgione, M. De Luca, R. Villalonga, F. Pisani, L. Biondi, F. Capuano, R. Velotta, B. Della Ventura, V. Iannotti, Advances in gluten detection: A rapid colorimetric approach using core-satellite magnetic particles, Biosens Bioelectron X 21 (2024). https://doi.org/10.1016/j.biosx.2024.100545.

[11] M. De Luca, A. Acunzo, D. Marra, M. Borriello, D. Ingrosso, R. Velotta, V. Iannotti, B. Della Ventura, Beyond the Passive Diffusion: Core@Satellite Magneto-Plasmonic Particles for Rapid and Sensitive Colorimetric Immunosensor Response, Advanced Sensor Research 3 (2024). https://doi.org/10.1002/adsr.202400006.

[12] D. Marra, B. Šarkanj, B. Della Ventura, A. Acunzo, M. De Luca, R. Velotta, N. Sakač, Magnetophoretic Biosensor for the Detection of Deoxynivalenol in Food Safety Applications, IEEE Sens J 25 (2025) 24008–24016. https://doi.org/10.1109/JSEN.2025.3570984.

[13] A. Acunzo, M. De Luca, D. Marra, B. Della Ventura, A. Offenhäusser, D. Mayer, R. Velotta, Ultra-uniform high-quality plasmonic metasurfaces through electrostatic self-assembly of gold nanoparticles on chemically unmodified glass, Nanoscale 17 (2025) 14125–14133. https://doi.org/10.1039/d5nr01116g.

[14] M. De Luca, A. Acunzo, E. La Civita, F. Gentile, D. Terracciano, R. Velotta, B. Della Ventura, Metal Enhanced Fluorescence Immunosensor Based on Gold Nanoparticles Array for Early Diagnosis of Prostate Cancer, IEEE Sens Lett 8 (2024). https://doi.org/10.1109/LSENS.2024.3404608.

[15] B. Della Ventura, M. Cennamo, A. Minopoli, R. Campanile, S.B. Censi, D. Terracciano, G. Portella, R. Velotta, Colorimetric Test for Fast Detection of SARS-CoV-2 in Nasal and Throat Swabs, ACS Sens 5 (2020) 3043–3048. https://doi.org/10.1021/acssensors.0c01742.

[16] A. Minopoli, N. Sakač, B. Lenyk, R. Campanile, D. Mayer, A. Offenhäusser, R. Velotta, B. Della Ventura, LSPR-based colorimetric immunosensor for rapid and sensitive 17β-estradiol detection in tap water, Sens Actuators B Chem 308 (2020) 127699. https://doi.org/10.1016/j.snb.2020.127699.

[17] Y.Q. Liu, Y.C. Chao, S.Q. Xu, Y.R. Peng, J.J. Syu, X.H. Yang, Y.K. Pan, P.C. Lin, L.L. Weng, I.C. Chen, K.T. Tan, Surface Functionalization of Gold Nanoparticles Using Alkyne Derivatives: Applications in Chemical Sensing, ACS Appl Mater Interfaces 16 (2024) 58262–58273. https://doi.org/10.1021/acsami.4c12063.

[18] M. Iarossi, C. Schiattarella, I. Rea, L. De Stefano, R. Fittipaldi, A. Vecchione, R. Velotta, B. Della Ventura, Colorimetric Immunosensor by Aggregation of Photochemically Functionalized Gold Nanoparticles, ACS Omega 3 (2018) 3805–3812. https://doi.org/10.1021/acsomega.8b00265.

[19] C.A. Mirkin, R.L. Letsinger, R.C. Mucic, J.J. Storhoff, A DNA-based method for rationally assembling nanoparticles into macroscopic materials, Nature 382 (1996) 607–609. https://doi.org/10.1038/382607a0.

[20] R. Dutour, G. Bruylants, Gold Nanoparticles Coated with Nucleic Acids: An Overview of the Different Bioconjugation Pathways, Bioconjug Chem 36 (2025) 1133–1156. https://doi.org/10.1021/acs.bioconjchem.5c00098.

[21] X. Zhang, M.R. Servos, J. Liu, Instantaneous and Quantitative Functionalization of Gold Nanoparticles with Thiolated DNA Using a pH-Assisted and Surfactant-Free Route, J Am Chem Soc 134 (2012) 7266–7269. https://doi.org/10.1021/ja3014055.

[22] X. Zhang, T. Gouriye, K. Göeken, M.R. Servos, R. Gill, J. Liu, Toward fast and quantitative modification of large gold nanoparticles by thiolated DNA: Scaling of nanoscale forces, kinetics, and the need for thiol reduction, Journal of Physical Chemistry C 117 (2013) 15677–15684. https://doi.org/10.1021/jp403946x.

[23] M. Enea, A. Leite, R. Franco, E. Pereira, Gold Nanoprobes for Robust Colorimetric Detection of Nucleic Acid Sequences Related to Disease Diagnostics, Nanomaterials 14 (2024) 1833. https://doi.org/10.3390/nano14221833.

[24] B. Liu, J. Liu, Freezing Directed Construction of Bio/Nano Interfaces: Reagentless Conjugation, Denser Spherical Nucleic Acids, and Better Nanoflares, J Am Chem Soc 139 (2017) 9471–9474. https://doi.org/10.1021/jacs.7b04885.

[25] B. Liu, J. Liu, Freezing-Driven DNA Adsorption on Gold Nanoparticles: Tolerating Extremely Low Salt Concentration but Requiring High DNA Concentration, Langmuir 35 (2019) 6476–6482. https://doi.org/10.1021/acs.langmuir.9b00746.

[26] K. Sato, K. Hosokawa, M. Maeda, Non-cross-linking gold nanoparticle aggregation as a detection method for single-base substitutions., Nucleic Acids Res 33 (2005). https://doi.org/10.1093/nar/gni007.

[27] H. Ahmadpour-Yazdi, M.R. Hormozi-Nezhad, A.R. Abadi, M.H. Sanati, B. Kazemi, Colorimetric assay for exon 7 SMN1/SMN2 single nucleotide polymorphism using gold nanoprobes, BioImpacts 3 (2013) 185–194. https://doi.org/10.5681/bi.2013.037.

[28] G. Wang, Y. Akiyama, S. Shiraishi, N. Kanayama, T. Takarada, M. Maeda, Cross-linking versus non-cross-linking aggregation of gold nanoparticles induced by DNA hybridization: A comparison of the rapidity of solution color change, Bioconjug Chem 28 (2017) 270–277. https://doi.org/10.1021/acs.bioconjchem.6b00410.

[29] Z. Heidari, S.E. Rezatofighi, S. Rastegarzadeh, Development and comparison of cross-linking and non-crosslinking probe-gold nanoparticle hybridization assays for direct detection of unamplified bovine viral diarrhea virus-RNA, BMC Biotechnol 21 (2021). https://doi.org/10.1186/s12896-021-00691-w.

[30] K. Sato, K. Hosokawa, M. Maeda, Rapid aggregation of gold nanoparticles induced by non-cross-linking DNA hybridization, J Am Chem Soc 125 (2003) 8102–8103. https://doi.org/10.1021/ja034876s.

[31] Y. Xu, K. Huang, A. Lopez, W. Xu, J. Liu, Freezing promoted hybridization of very short DNA oligonucleotides, Chemical Communications 55 (2019) 10300–10303. https://doi.org/10.1039/c9cc04608a.

[32] B. Liu, T. Wu, Z. Huang, Y. Liu, J. Liu, Freezing-directed Stretching and Alignment of DNA Oligonucleotides, Angewandte Chemie 131 (2019) 2131–2135. https://doi.org/10.1002/ange.201814352.

[33] Q. Zuriegat, Y. Zheng, H. Liu, Z. Wang, Y. Yun, Current progress on pathogenicity-related transcription factors in Fusarium oxysporum, Mol Plant Pathol 22 (2021) 882–895. https://doi.org/10.1111/mpp.13068.

[34] E. Jackson, J. Li, T. Weerasinghe, X. Li, The Ubiquitous Wilt-Inducing Pathogen Fusarium oxysporum—A Review of Genes Studied with Mutant Analysis, Pathogens 13 (2024). https://doi.org/10.3390/pathogens13100823.

[35] K. V Krutovsky, D.B. Neale, Nucleotide Diversity and Linkage Disequilibrium in Cold-Hardiness- and Wood Quality-Related Candidate Genes in Douglas Fir, Genetics 171 (2005) 2029–2041. https://doi.org/10.1534/genetics.105.044420.

[36] J. Turkevich, P.C. Stevenson, J. Hillier, A study of the nucleation and growth processes in the synthesis of colloidal gold, Discuss Faraday Soc 11 (1951) 55. https://doi.org/10.1039/df9511100055.

[37] Y. Lu, J. Liu, Functional DNA nanotechnology: emerging applications of DNAzymes and aptamers, Curr Opin Biotechnol 17 (2006) 580–588. https://doi.org/10.1016/j.copbio.2006.10.004.

[38] A. Barchanski, N. Hashimoto, S. Petersen, C.L. Sajti, S. Barcikowski, Impact of spacer and strand length on oligonucleotide conjugation to the surface of ligand-free laser-generated gold nanoparticles, Bioconjug Chem 23 (2012) 908–915. https://doi.org/10.1021/bc200462b.

[39] S.J. Hurst, A.K.R. Lytton-Jean, C.A. Mirkin, Maximizing DNA loading on a range of gold nanoparticle sizes, Anal Chem 78 (2006) 8313–8318. https://doi.org/10.1021/ac0613582.

[40] D.Y. Choi, S. Kim, J.W. Oh, J.M. Nam, nanoparticlesConjugation strategies of DNA to gold, Bull Korean Chem Soc 43 (2022) 1298–1306. https://doi.org/10.1002/bkcs.12621.

[41] X. Liu, Y. Zhao, Y. Ding, J. Wang, J. Liu, Stabilization of Gold Nanoparticles by Hairpin DNA and Implications for Label-Free Colorimetric Biosensors, Langmuir 38 (2022) 5542–5549. https://doi.org/10.1021/acs.langmuir.2c00119.

[42] X. Wang, Z. Yang, Y. Li, K. Huang, N. Cheng, Towards rational design: Developing universal freezing routes for anchoring DNA onto gold nanoparticles, J Colloid Interface Sci 655 (2024) 830–840. https://doi.org/10.1016/j.jcis.2023.11.041.

[43] M. Hu, C. Yuan, T. Tian, X. Wang, J. Sun, E. Xiong, X. Zhou, Single-Step, Salt-Aging-Free, and Thiol-Free Freezing Construction of AuNP-Based Bioprobes for Advancing CRISPR-Based Diagnostics, J Am Chem Soc 142 (2020) 7506–7513. https://doi.org/10.1021/jacs.0c00217.

[44] Y. Tanaka, G. Hirao, N. Fukuzumi, T. Asahi, M. Maeda, A. Ogawa, T. Zako, Effect of DNA Density on Nucleic Acid Detection Using Cross-Linking Aggregation of DNA-Modified Gold Nanoparticles, Langmuir (2025). https://doi.org/10.1021/acs.langmuir.4c04343.

[45] F. Liu, H. Wu, Q. Chen, J. Gao, G. Wang, Demonstration of a Magic Reaction: Accelerating DNA Functionalization of Gold Nanoparticles by Freezing, J Chem Educ 100 (2023) 2009–2014. https://doi.org/10.1021/acs.jchemed.3c00022.

[46] T. D'Aponte, M. De Luca, E. de Alteriis, F. Carteni, S. Mazzoleni, R. Velotta, V. Iannotti, B. Della Ventura, Electrochemical biosensor with custom fluidics for amplification-free, low-picomolar DNA detection, Anal Chim Acta 1374 (2025). https://doi.org/10.1016/j.aca.2025.344554.

[47] H. Moulahoum, F. Ghorbanizamani, The LOD paradox: When lower isn't always better in biosensor research and development, Biosens Bioelectron 264 (2024). https://doi.org/10.1016/j.bios.2024.116670.

[48] J.J. Hao, M.E. Yang, R.M. Davis, Effect of soil inoculum density of fusarium oxysporum f. sp. vasinfectum race 4 on disease development in cotton, Plant Dis 93 (2009) 1324–1328. https://doi.org/10.1094/PDIS-93-12-1324.

[49] X. Yan, S. Guo, K. Gao, S. Sun, C. Yin, Y. Tian, The Impact of the Soil Survival of the Pathogen of Fusarium Wilt on Soil Nutrient Cycling Mediated by Microorganisms, Microorganisms 11 (2023). https://doi.org/10.3390/microorganisms11092207.

[50] A. Bellini, G. Gilardi, M. Idbella, M. Zotti, M. Pugliese, G. Bonanomi, M.L. Gullino, Trichoderma enriched compost, BCAs and potassium phosphite control Fusarium wilt of lettuce without affecting soil microbiome at genus level, Applied Soil Ecology 182 (2023). https://doi.org/10.1016/j.apsoil.2022.104678.

[51] F. Matarese, S. Sarrocco, S. Gruber, V. Seidl-Seiboth, G. Vannacci, Biocontrol of Fusarium head blight: Interactions between Trichoderma and mycotoxigenic Fusarium, Microbiology (N Y) 158 (2012) 98–106. https://doi.org/10.1099/mic.0.052639-0.

[52] C. Alabouvette, P. Lemanceau, C. Steinberg, Recent advances in the biological control of fusarium wilts, Pestic Sci 37 (1993) 365–373. https://doi.org/10.1002/ps.2780370409.

Finanziato dall'Unione europea NextGenerationEU
Italiadomani PIANO NAZIONALE DI RIPRESA E RESILIENZA
agritech

Supplementary Material

Rapid Label-Free Colorimetric ssDNA Biosensor Based on Gold Nanoparticles: Application to *Fusarium oxysporum* Detection in Soil

Erica Cavaliere[a], Tina D'Aponte[a], Emanuela Palomba[b], Maurizio Zotti[b], Pasquale Termolino[c], Vincenzo Iannotti[a,d], Stefano Mazzoleni[c], Raffaele Velotta[a], Bartolomeo Della Ventura[a*]

[a]Department of Physics "Ettore Pancini", University of Naples "Federico II", Via Cinthia 26, 80126 Naples, Italy.

[b]Department of Agricultural Sciences, University of Naples "Federico II", Piazza Carlo di Borbone 1, 80055 Portici (NA), Italy

[c]Institute of Biosciences and Bioresources, UOS Portici Via Università 133 80055 Portici (Italy)

[d]CNR – SPIN c/o Department of Physics "E. Pancini", Piazzale V. Tecchio 80, 80125 Naples, Italy

* Corresponding author bartolomeo.dellaventura@unina.it

Table of contents

Figure S1. Morphology and size characterization of synthesized gold nanoparticles (AuNPs).

Figure S2. Optimization of AuNP functionalization with complementary ssDNA probe (C_Probe).

Figure S3. Effect of post-functionalization centrifugation on f-AuNPs.

Table S1. Estimation of ssDNA surface coverage on AuNPs.

Figure S4. Extinction spectra and sensing parameter.

Figure S5. Impact of f-AuNPs surface coverage on detection performance.

Table S2. List of probes and ssDNA sequences for preliminary specificity and stability assays.

Figure S6. Preliminary specificity assessment with alternative probe sequences.

Figure S7. Stability test.

Figure S8. Agarose gel electrophoresis of sonicated DNA.

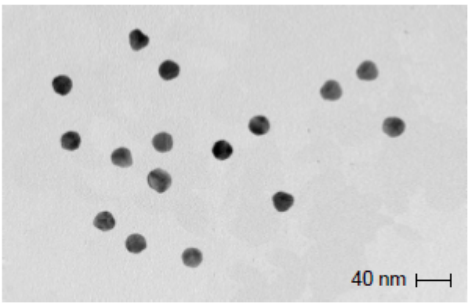

Figure S1. Morphology and size characterization of gold nanoparticles (AuNPs). Transmission electron microscopy (TEM) image of spherical AuNPs prepared via a modified Turkevich method, exhibiting uniform size distribution with an average diameter of approximately 20 nm.

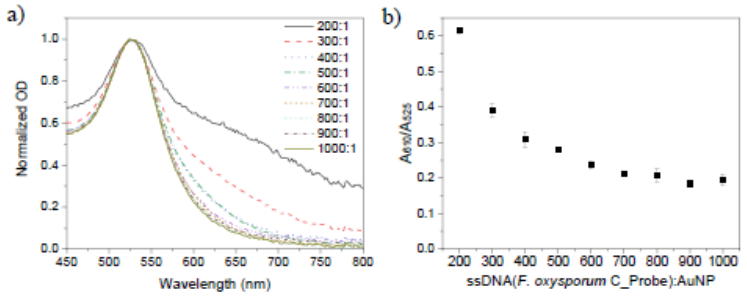

Figure S2. Optimization of AuNP functionalization with complementary ssDNA probe (C_Probe). (a) Normalized UV–Vis extinction spectra of AuNPs functionalized with the Fusarium C_Probe at different ssDNA:AuNP molar ratios. (b) Corresponding absorbance ratio at 610 nm and 525 nm (A_{610}/A_{525}), showing an optimal value of 0.28 at a 400:1 ratio.

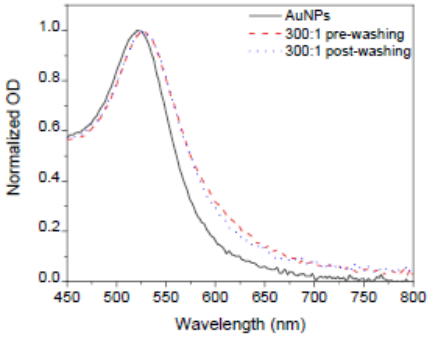

Figure S3. Effect of post-functionalization centrifugation on f-AuNPs. Normalized UV–Vis extinction spectra of AuNPs functionalized with the *F. oxysporum* Probe at a 300:1 ssDNA:AuNP molar ratio, measured pre and post centrifugation. The ratio A_{610}/A_{525} decreases from 0.28 to 0.24, indicating removal of aggregates or dimers formed during functionalization due to non-excess ssDNA coverage.

Table S1. Estimation of ssDNA surface coverage on AuNPs.

ssDNA:AuNP	C_{added} (μM)	V (μL)	C_{free} (μM)	C_{AuNP} (μM)	N	A_{ssDNA} (nm^2)
300:1	40	3	0.3	0.04	≈220	≈6.0
700:1	40	7	1.2	0.04	≈370	≈3.5

Parameters used to calculate the number of ssDNA strands per gold nanoparticle and the corresponding surface area occupied by each strand. As expected, increasing the ssDNA:AuNP molar ratio results in higher DNA loading per particle and a reduced average surface area available per strand.

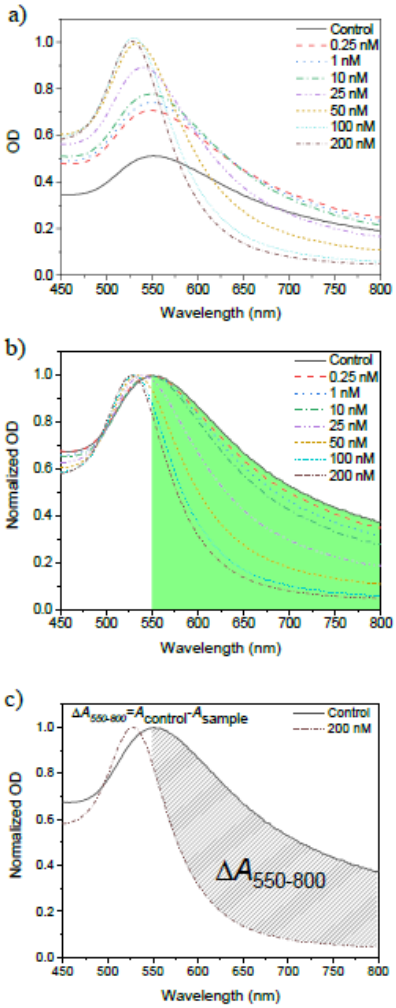

Figure S4. Extinction spectra and sensing parameter. (a) Extinction spectra at several concentrations. (b) Normalized extinction spectra highlighting the 550–800 nm range. (c) Graphical illustration of ΔA for 20 nM.

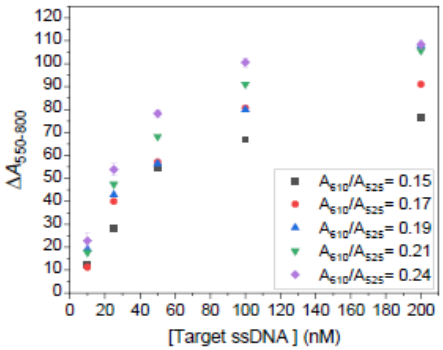

Figure S5. Impact of f-AuNPs surface coverage on detection performance. Detection performed using f-AuNPs with different A_{610}/A_{525} ratios shows that nanoparticles with an A_{610}/A_{525} ratio of 0.24 (after washing) yield the strongest signal, indicating that higher ssDNA surface density can obstruct target sequence detection. Conversely, a higher ratio — corresponding to lower surface coverage — is not feasible, as the AuNPs would become highly unstable.

Table S2. List of probes and ssDNA sequences for preliminary specificity and stability assays.

	ssDNA sequences	bp	Sequence 5' to 3'
1	Probe	30	Thiol-C6- AAAAACCCCC TCC CTC CAT TTC CCT CTC TT
2	C_Probe	30	Thiol-C6- AAAAACCCCC AAG AGA GGG AAA TGG AGG GA
3	Non-target sequence 1 (NTS1)	20	GTG CGA TGG TTG GTA GTA GT
4	Non-target sequence 2 (NTS2)	20	ACT ACT ACC AAC CAT CGC AC
5	Non-target sequence 3 (NTS3)	20	GCT GGT CAA GGT TTC TCT GC
6	Non-target sequence 4(LNTS)	50	CCT ACG TAG CTA GCA TAC GGT ACT AGC TAT ACG CAA TGC TAC GTA CGC AT
7	Target sequence (TS)	20	AAG AGA GGG AAA TGG AGG GA
8	Long Target sequence (LTS)	30	**ACT GAA** AGA GAG GGA AAT GGA GGG ACG **GTC**
9	Target sequence 1m.m (TSM)	20	AAG AGA GGG T̲AA TGG AGG GA

The ssDNA sequences in lines 1–2 were used to functionalize the AuNP batches, whereas those in lines 3–9 were used for specificity tests. In the table, bold indicates bases added to the target sequence, while underlining denotes mismatches.

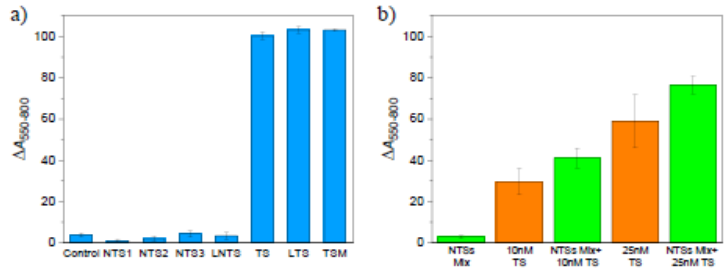

Figure S6. Specificity tests with alternative probe sequences. (a) Specificity was evaluated using the sequences listed in Table S2 (lines 3–9), each tested at a concentration of 200 nM. The results show that the system is highly specific and capable of detecting the target sequence even when embedded within a longer strand. However, it is unable to discriminate a single central mismatch. Non-target sequences did not produce any significant signal. (b) Specificity was further assessed by mixing all non-target sequences (200 nM each) and adding the target sequence at varying concentrations (10 nM and 200 nM). The results (green bars) closely match those obtained with the target alone (orange bars), indicating that the biosensor effectively detects the target even in the presence of multiple non-target sequences. All error bars represent duplicate experiments.

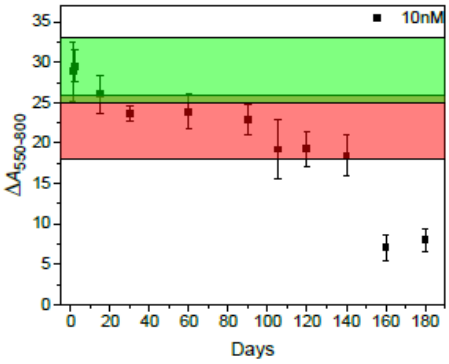

Figure S7. Stability test. AuNP batches functionalized with the probe sequences listed in Table S3 were evaluated for stability. The f-AuNPs were stored in the dark at 4 °C, and their sensing response was monitored over time using a 10 nM target sequence. The f-AuNPs retained 100% activity for up to 15 days. From day 16 to day 120, functionality declined by approximately 10%, demonstrating robust long-term stability under these storage conditions. All error bars represent duplicate experiments.

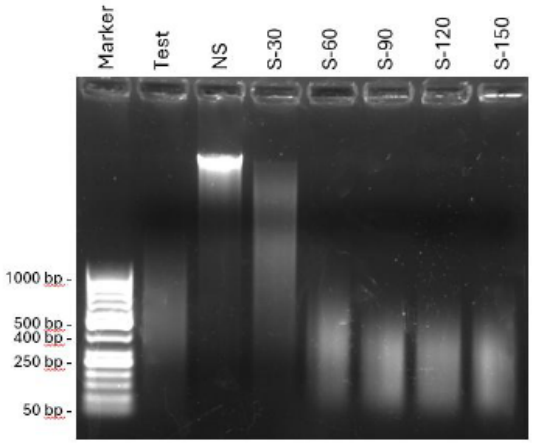

Figure S8. Agarose gel electrophoresis of sonicated DNA. The gel (1% Ultrapure agarose, Thermo Scientific) was prepared in 1× Tris-acetate-EDTA (TAE). Marker: GeneRuler 50 bp DNA Ladder (Thermo Scientific), indicating fragment sizes. Test: DNA sonicated for 10 minutes under standard ChIP conditions using a Bioruptor Plus Sonicator. NS: non-sonicated DNA. S-30, S-60, S-90, S-120, and S-150: DNA sonicated for 30, 60, 90, 120, and 150 minutes, respectively, in an Elmasonic Sonicator (S 40 (H), 37 kHz). The results demonstrate effective DNA fragmentation and show that, when using a high-power sonicator, the required fragmentation time can be significantly reduced.